Solid-State Sensitized Heterojunction Solar Cells: Effect of Sensitizing Systems on Performance and Stability

PAR

Soo-Jin MOON

ÉCOLE POLYTECHNIQUE
FÉDÉRALE DE LAUSANNE

Suisse
2011

Abstract

Dye-sensitized solar cells (DSCs) are considered as an emerging technology in order to replace conventional silicon solar cells or thin film solar cells such as amorphous silicon, CIGS, and CdTe. Liquid electrolytes containing iodide/triiodide redox couple have a durability problem due to the corrosion of metal contacts. In order to improve the long-term stability of DSC device it is important to find an alternate efficient redox couple. In search of this we are using 2,2′,7,7′-tetrakis-(N,N-di-methoxyphenylamine)-9,9′-spirobifluorene (spiro-OMeTAD) as a hole transport material for solid-state dye-sensitized solar cells (SSDSCs). In comparison to the liquid electrolytes the efficiencies of SSDSCs are inferior, they are around only 30% of the efficiencies obtained with the liquid electrolytes. In optimizing the device performance and stability of SSDSCs, various light harvesting systems are employed to enhance a photovoltaic performance and investigated their properties in SSDSCs.

In SSDSCs we use thin TiO_2 films to avoid the pore-filling problem of HTM. Hence it is critical to use high molar extinction coefficient dyes with an efficient light harvesting capability for SSDSCs. Representative ruthenium sensitizers such as N719 or Z907 have shown good and stable performances in liquid electrolyte-based DSCs. However, their performances are low in SSDSCs due to insufficient light harvesting in thin mesoporous TiO_2 films. A new family of heteroleptic polypyridyl ruthenium sensitizers having thiophene units was employed to increase the light harvesting capabilities and their applicability in SSDSCs. These new dyes could improve the absorbed photon-to-current conversion efficiencies as well as power conversion efficiencies due to their high molar extinction coefficients. The thiophene units of the ancillary ligands not only enhanced molar extinction coefficients but also augmented electron lifetime in the devices.

In general, ruthenium sensitizers possess lower molar extinction coefficients compared to organic dyes. In order to increase the molar extinction coefficients and bathochromic shift in the absorption spectra of organic dyes, we applied donor-acceptor concept in organic dyes with different π-conjugation bridges. Consequently, we achieved 6 % power conversion efficiency at AM 1.5G solar irradiation (100 mW/cm^2) in a solid-state dye-sensitized solar cell. Transient photovoltage and photocurrent decay measurements showed that the enhanced performance of this device was ascribe to higher charge collection efficiency over a wider potential range. We also examined near infrared absorbing dyes and they could be employed to different device architectures such as tandem cells, Förster Resonance Energy Transfer, or co-sensitization to substantiate panchromatic response.

Another interesting type of sensitizers is semiconductor or quantum dots due to their unique properties. However, the efficiency of the semiconductor-sensitized solar cells was only 1-2 % range. Recently, much improved efficiencies were reported with Sb_2S_3-sensitized cells using different hole conductors. The Sb_2S_3-sensitized cells with spiro-OMeTAD demonstrated a very high incident

photon-to-conversion efficiency (IPCE) of 90 %. This excellent result shows that the semiconductor sensitizers are promising candidate as light absorbers for SSDSCs.

Most of the standard ruthenium and organic dyes have the limited absorption in near infrared region of the solar spectrum. Porphyrin sensitizers possess strong absorptions in the visible and near infrared region and they have good chemical, photochemical and thermal stability. However, the power conversion efficiency of SSDSCs devices using a novel D-π-A porphyrin we reached only 1.6 %. In order to improve a cell performance, porphyrin was co-sensitized with an organic dye to increase light harvesting capability in the green wavelength region as well as to reduce the dye aggregation. Instead of spiro-OMeTAD a polymer hole conductor was applied, which had intense spectral response in the visible region. Interestingly, in this system the polymer hole conductor showed dual functions, as a light absorber and a hole transporter. This hybrid solar cell exhibited a clear panchromatic response and improved the power conversion efficiency of device compared to the cell with spiro-OMeTAD.

Résumé

Les cellules solaires sensibilisées par des colorants (ou cellule solaires à colorants, Dye-Sensitized Solar Cell, DSC) sont considérées comme une technologie émergente dans le domaine de l'energie solaire de remplacer les cellules solaires classiques comme celles basées sur le silicium ou cellules à couches minces basées sur des matériaux tels que le silicium amorphe, CIGS, CdTe. Les électrolytes liquides, utilisés principalement dans les cellules solaires à colorant, contiennent le couple redox iodure/triiodure cousant une faible durabilité des cellules due à la corrosion des contacts métalliques. Pour améliorer la stabilité de la DSC stabilité à long terme, il est important de trouver un autre couple redox efficace. Dans ce but, nous utilisons le composé organique 2,2',7,7'-tétrakis-(N,N-di-methoxyphenylamine)-9,9'-spirobifluorène (spiro-OMeTAD) comme transporteur de trous (charges positives) dans le cadre de cellules solaires sensibilisée par des colorants à hétérojonction solide (Solid-State Dye-Sensitized Solar Cells, SSDSCs). La performance des SSDSCs est aujourd'hui bien inférieure à celle des cellules utilisant un électrolyte liquide est seulement 30 % de l'éfficacité maximale des cellules solaires à colorant à électrolyte liquide est obtenue avec la meilleure cellule comportant un électrolyte solide. En optimisant la performance et la stabilité des DDSCSs, divers systèmes de collection de lumière ont été utilisées afin d'améliorer leur rendement photovoltaïque ainsi que d'étudier leurs propriétés dans les SSDSCs.

Dans les SSDSCs, des couches très minces de TiO_2 sont utilisées pour éviter le problème de remplissage des pores par le conducteur de trou (HTM). C'est pourquoi il est essentiel d'utiliser des colorants ayant un fort coefficient d'extinction molaire pour collecter efficacement l'énergie lumineuse dans les SSDSCs. Les colorants au ruthénium, tel que le N719 ou le Z907, ont démontré de bonnes performances et une longue stabilité dans les cellules DSC utilisant un électrolyte liquide. Cependant, leurs performances sont faibles dans les SSDSCs en raison de la faible quantité de lumière absorbé par ces colorants lorsque ceux-ci sont absorbés sur des couches minces de TiO_2 mésoporeux. Une nouvelle famille de colorant au ruthénium comportant des ligands polypyridyl hétéroleptiques ruthénium, incluant des unités thiophène, a été utilisée pour augmenter l'absorption lumineuse et rendre l'application des colorants au ruthénium possible dans les SSDSCs. Ces nouveaux colorants peuvent améliorer l'efficacité quantique (conversion du photon absorbée en charges électroniques) et l'efficacité énergétique (conversion en terme de puissance) en raison de leurs hauts coefficients d'extinction molaire. Les unités thiophène des ligands auxiliaires ont non seulement ont amélioré le coefficients d'extinction molaire du colorant, mais ont aussi augmenté le temps de vie de l'électrons dans les dispositifs.

En général, les colorants au ruthénium possèdent des coefficients d'extinction molaire inférieure par rapport aux colorants organiques. Nous avons appliqué le concept de donneur-accepteur dans des

colorants organiques utilisant différents ponts π-conjugués pour augmenter le coefficients d'extinction molaire et effecteur un déplacement bathochromic du spectres d'absorption des colorants organiques (D-π-A). Cette stratégie nous a permis d'obtenir 6 % d'efficacité à une illumination AM 1.5G (100 mW/cm^2) dans la SSDSC. Les mesures de décroissance transitoires du photo-courant et photo-voltage ont permis d'attribuer l'amélioration des performances de ce système à une plus grande efficacité de collection de charge sur une plus grande gamme de potentiel. Nous avons également examiné des colorants absorbant des longueurs d'onde dans le proche infrarouge qui permettraient d'utiliser les cellules à colorants dans différentes architectures telles que des structures tandem de cellules, des systèmes utilisant le transfert d'énergie entre colorants de type Förster (FRET), ou ceux utilisant co-sensibilisation du semiconducteur pour obtenir une réponse panchromatique.

Un autre intéressant moyen de sensibiliser le semiconducteurs est d'utiliser un autre semiconducteurs sous forme de petites nanoparticules (quantum dots) en raison de leurs propriétés optoélectroniques uniques. Cependant, l'efficacité des cellules solaires sensibilisées par des semiconducteurs a seulement été de l'ordre de 1-2 %. Récemment, de nombreuses améliorations de l'efficacité de tels systémes ont été reportées avec des cellules sensibilisées par Sb_2S_3 en utilisant différents conducteurs trou. Les cellules sensibilisées par Sb_2S_3 ont démontré une efficacité quantique (IPCE) très élevé de 90 %. Cet excellent résultat démontre que les sensibilisateurs semi-conducteurs sont des candidats prometteurs pour absorber l'énergie solaire dans les SSDSCs.

La plupart des colorants au ruthénium et des colorants organiques ont une absorption limitée dans la région proche infrarouge du spectre solaire. Les colorants de type porphyrine possèdent une forte absorption dans le visible ainsi que dans le proche infrarouge et ils possèdent une bonne stabilité chimique, photochimique et thermique. Cependant, en utilisant un nouveau système D-π-A comprenant une partie porphyrine dans les SSDSC, nous avons seulement atteint 1.6 % d'efficacité énergétique. Pour améliorer la performance de cette cellule, porphyrine a été co-sensibilisées avec un colorant organique pour augmenter l'absorption dans la région du spectre solaire correspondant à la couleur verte ainsi que pour réduire l'agrégation du colorant. Au lieu de spiro-OMeTAD un conducteur trou polymère, qui possédait une intense réponse spectrale dans le visible a été appliqué. Fait intéressant, dans ce système, le conducteur de trou polymère a démontré deux fonctions : absorbeur de lumière et transporteur de trou. Cette cellule solaire hybride présentait indubitablement une réponse panchromatique et a amélioré l'efficacité énergétique de la cellule par rapport à celle avec le spiro-OMeTAD.

Mots-clés: Cellules solaires sensibilisées par des colorants, Cellules solaires sensibilisée par des colorants à hétérojonction solide, Colorants au ruthénium, Colorants organiques, Sensibilisateurs semiconducteurs, Colorants porphyrine, Collecteurs de lumière, Conducteur de trou, Réponse spectrale panchromatique

List of Abbreviations

AM	Air mass
CDCA	Chenodeoxycholic acid
DSCs	Dye-sensitized solar cells
D-π-A	Donor-π-bridge-acceptor
FRET	Förster Resonance Energy Transfer
FTO	Fluorine-doped-tin oxide
GBA	4-guanidinobutyric acid
HOMO	Highest occupied molecular orbital
HTM	Hole transporting material
IPCE	Incident monochromatic photon-to-current conversion efficiency
IR	Infrared
IUPAC	International Union of Pure and Applied Chemistry
J-V	Current-Voltage
LiTFSI	Li(CF$_3$SO$_2$)$_2$N
LHE	Light harvesting efficiency
LUMO	Lowest unoccupied molecular orbital
MLCT	Metal-to-ligand charge transfer
OPV	Organic photovoltaic
P3HT	Poly(3-hexylthiophene)
PCE	Power conversion efficiency
PEDOT	Poly(3,4-ethylenedioxythiophene)
PIA	Photo-induced absorption
PL	Photoluminescence
PPA	3-phenylpropionic acid
QD	Quantum dot
spiro-OMeTAD	2,2',7,7'-tetrakis(N,N-di-p-methoxyphenyl-amine)9,9'-spirobifluorene
SSDSCs	Solid-state dye-sensitized solar cells
t-BP	4-*tert*-butylpyridine
TCO	Transparent conductive oxide
UV-Vis	Ultraviolet-visible
F.F.	Fill factor
I_{sc}	Short-circuit current
J_{sc}	Short-circuit current density

V_{oc}	Open-circuit voltage
η	Power conversion efficiency
τ_e	Electron lifetime

Contents

Chapter 1

Introduction

Renewable energy has become the major talking point since the last oil crisis in the 1970s. Finally, world primary energy (for example, crude oil and coal etc.) consumption fell by 1.1% in 2009[1], the first decline since 1982. This shows that renewables are starting to play a significant role in power generation replacing fossil fuels. Wind, geothermal heat, hydroelectric and solar energy are the representative sources of the renewable energy. Solar energy is regarded as the most available source on earth because of its sufficient amount to cover all human energy consumption.

A solar cell is a device that produces electricity directly from the energy of sunlight. The first solar cell was only around 1 % power conversion efficiency (PCE) and was made by Charles Fritts in 1883[2]. However, solar cells have made remarkable progress since the first efficient silicon p-n junction was developed in 1954. Photovoltaic technology already has evolved into a third generation. The first generation cells are silicon-based cells with high efficiency and they still dominate the commercial solar panel market. In spite of that, there are several limitations such as high manufacturing costs, high energy and labor inputs to make these devices. To simplify manufacturing and reduce costs, the second-generation cells called thin film solar cells have been developed. The most successful materials have been amorphous silicon (a-Si), copper indium gallium selenide (CIGS) and cadmium telluride (CdTe)[3]. They are cheap, flexible and lightweight; however they have lower efficiency than 1st generation cells and also the toxicity of the materials is often a significant problem. Third generation solar cell technologies aim to enhance efficiency and notably lower costs compared to 1st and 2nd generation technologies[4-7](see Figure 1.1).

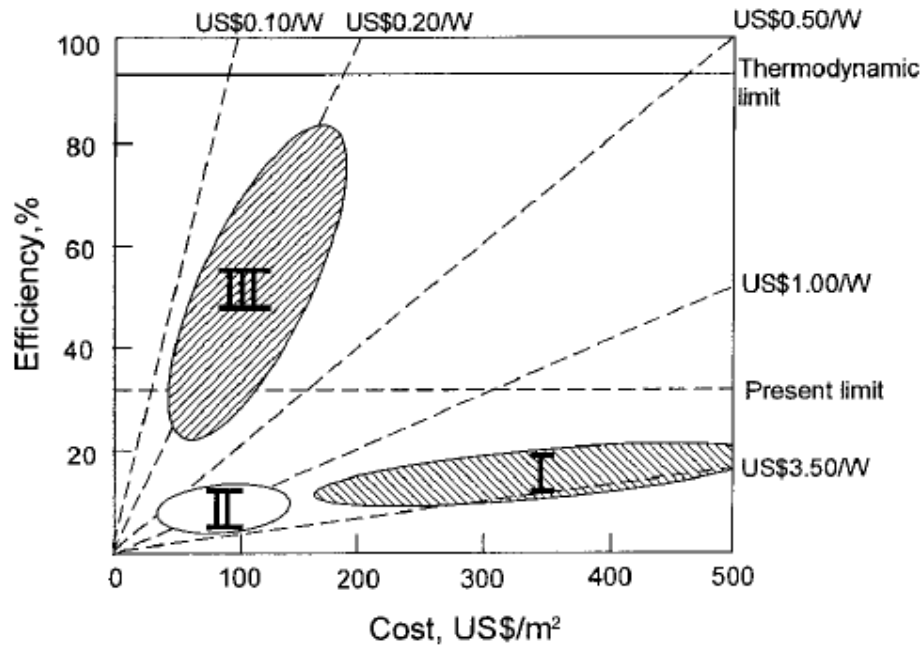Figure 1.1. Efficiency and cost projection for first, second and third generation photovoltaic technology[7].

In this chapter, third generation solar cells and the development of these technologies are briefly introduced. The development and operating mechanism of solid-state dye-sensitized solar cells (SSDSCs), in particular, are detailed. In the end, the objectives of this work will be presented.

1. 1 Third Generation Solar Cell Technologies

Third generation solar cells are emerging as novel PV-technologies. Most of them are still in the research phase. Generally they tend to include polymer solar cells, dye-sensitized solar cells, quantum dot cells, tandem/multi-junction cells, up – down conversion technologies and hot-carrier cells[8-11] In this section, mainly bulk heterojunction organic photovoltaic (OPV) cells and dye-sensitized solar cells (DSCs) are introduced.

1.1.1 Bulk heterojunction OPV cells

Single layer OPV and bilayer OPV cells were investigated before developing the bulk heterojuction OPV concept (see Figure 1.2)[12]. However, they had crucial problems of materials and device structures such as low charge carrier mobility of the organic electronic material, high recombination and short exciton diffusion length in the organic layer that prevented achieving high quantum efficiency. The problem of bilayer OPV cells is that, since they only produce free carriers at an interface between a donor and an acceptor material, they only collect a very small amount of current due to the low interfacial area. To increase the interfacial area between the donor and acceptor, bulk heterojunction OPV cells, which have a mixed composite of donor and acceptor, were created. Initially the obtained PCE was less than 1 % in the poly(phenylene vinylene) (PPV) system in 1995[13]. However, in the last fifteen years, remarkable progress has been made on the improvement of the PCE of bulk heterojunction OPV cells, and recently over 7 % efficiency was reached by optimising device processing and tuning materials[14].

The main steps in the device operation principles are depicted in Figure 1.3[15]. The first step is light absorption leading to exciton formation. When the donor material absorbs a photon, an electron in the highest occupied molecular orbital (HOMO) is excited to the lowest unoccupied molecular orbital (LUMO) and a positive hole is left in the HOMO. The excited electron and hole attract each other to form an exciton. Thus photon absorption in these materials does not produce free charge carriers. The typical exciton diffusion length is generally 10 to 20 nm, and the exciton can recombine, returning the electron to its ground state. If an exciton diffuses to the interface between the donor and acceptor, it can dissociate by electron transfer. Then the electron travels through the electron acceptor to one electrode while the hole moves through the other material to the second electrode. These free charges lead to photocurrent. If excitons do not reach the interface, they recombine and the absorbed energy is dissipated without producing photocurrent. Therefore, to efficiently generate power, the excitons have to be dissociated and collected at electrodes before recombination.
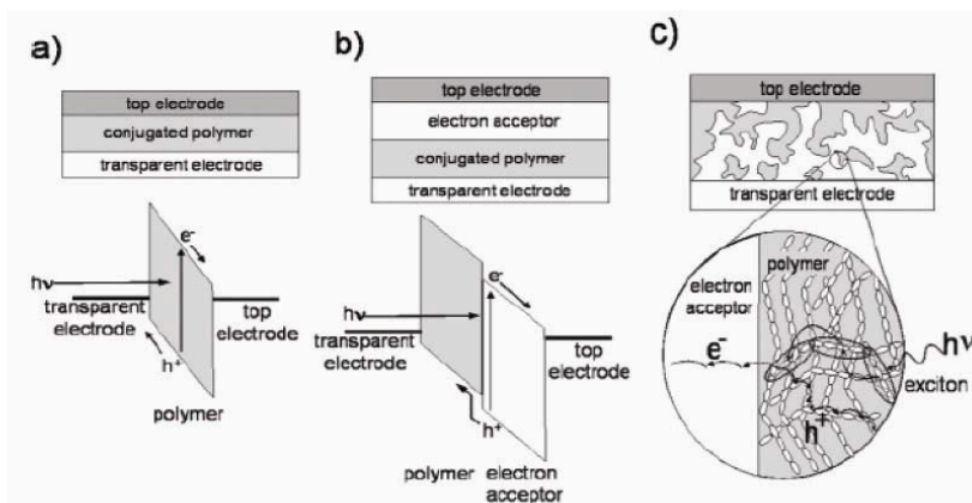
Figure 1.2. The device structures of OPV cells: a) single layer OPV cell, b) bilayer OPV cell and c) bulk heterojunction OPV cell.
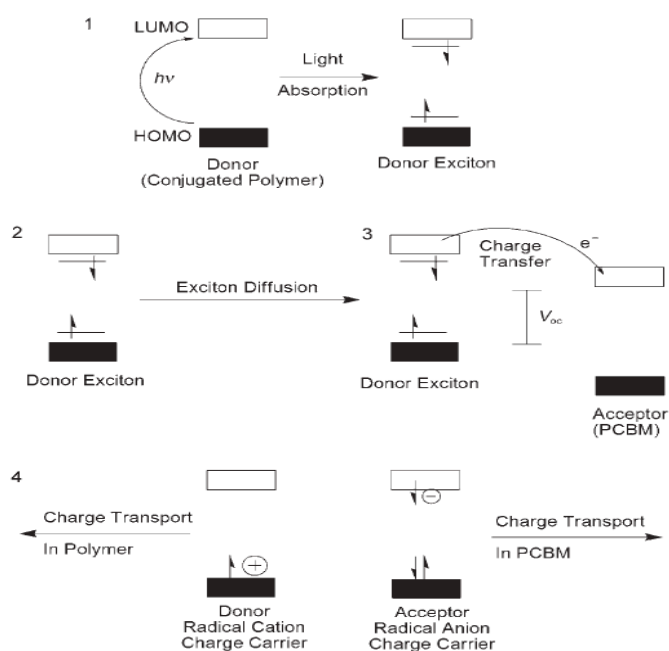
Figure 1.3. General mechanism for photoenergy conversion in the OPV solar cell.

OPV solar cells have many advantages such as simple fabrication process, small thickness, lightweight, and inexpensive material. However, they have several critical issues that hinder them from generating higher PCEs. Organic semiconductors have limited spectral coverage and organic thin films can not capture the incident light enoughly because of short exciton diffusion length. Another issue is the device stability as OPV cells are very sensitive to water and oxygen[16, 17].

4

1.1.2 Dye-sensitized solar cells (DSCs)

Initial study of DSCs was based on flat electrodes, but these devices had an intrinsic problem. The light harvesting efficiency is extremely low because only the first layer of adsorbed dye lead to effective electron injection into the semiconductor. The major breakthrough was in 1991 by O'Regan and Grätzel[18]. The photovoltaic performance was immensely improved by using a nanoporous electrode instead of the flat electrode. Since then, DSCs have been regarded as the next energy conversion device to substitute conventional Si solar cells. They are promising for low cost solar electricity generation owing to their cheap material and simple fabrication process. Already small cells reach over 11 % conversion efficiency[19]. They have not only high efficiency but also remarkable stability: more than 1000 hours at 60 ºC under continuous illumination of 1000 W/m^2 visible light with minor performance degradation[20-23].

1.1.2.1 Operating principles of DSCs

A DSC device consists of light harvesting dye-sensitized photoanode, counter electrode and electrolyte containing a redox couple. The photoanode is a porous nanocrystalline film composed of a wide band gap metal oxide such as TiO_2, ZnO[24-26], or SnO_2[27]. The electrolyte consists of the iodide/triiodide redox couple in organic solvents. The counter electrode is coated with platinum catalyst on conducting glass. The conducting glass substrate is coated with indium tin oxide (ITO) or fluorine doped tin oxide (FTO). Figure 1.4 shows the working mechanism of the DSC. When the dye absorbs incident light an electron is excited from the HOMO to the LUMO of the dye molecule. The electron from the excited dye (S*) is injected to the photoanode, made of a nanoporous semiconductor, and the subsequently oxidized dye (S$^+$) is regenerated by an electron from the redox couple in the electrolyte. The injected electron travels by diffusion through the nanoporous film and is collected at the substrate contact where it is released to the external circuit. Passing through the external circuit, the electron is returned to the counter electrode. The oxidized redox species are then regenerated by the circulated electron at the counter electrode (see Figure 1.4.[28]). Thus, the device generates electricity from light without any permanent chemical transformation.

Fast electron injection and efficient regeneration of the dye and the redox couple are required for an efficient device. Figure 1.5[29] shows the kinetic processes in a DSC device. Forward reactions such as electron injection to the semiconductor and regeneration of the oxidized dye and redox couples compete with recombination reactions. Briefly, two types of recombination processes take place in a DSC device. In the device, photoinjected electrons traverse a relatively long pathway through the mesoporous TiO_2 layer surrounded by dye and electrolyte. These electrons then have many chances to recombine with an oxidized dye molecule or electron acceptors in the electrolyte. In general, the

recombination process is much slower than the forward process, but nevertheless, the competition between the forward and recombination reactions is a critical point that affects a power conversion effeiciency of a device.
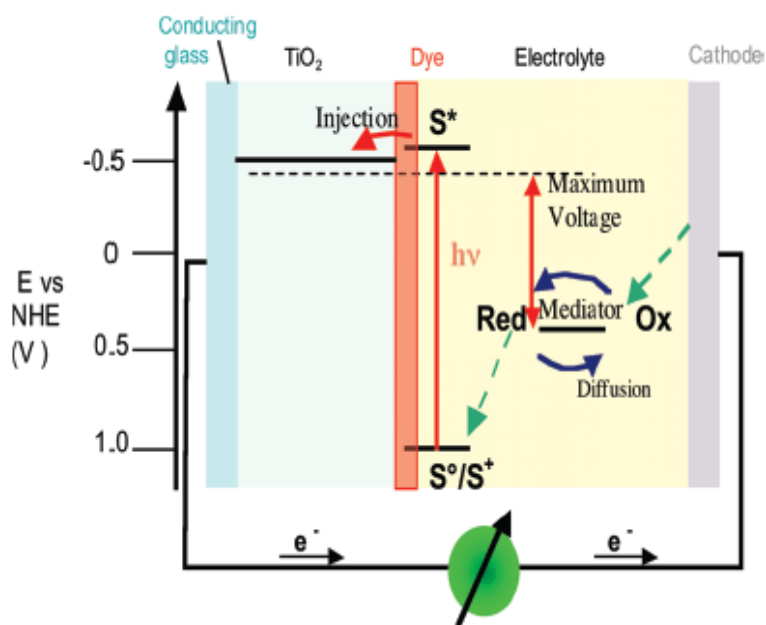

Figure 1.4. Structure and operating principle of the dye-sensitized solar cell.
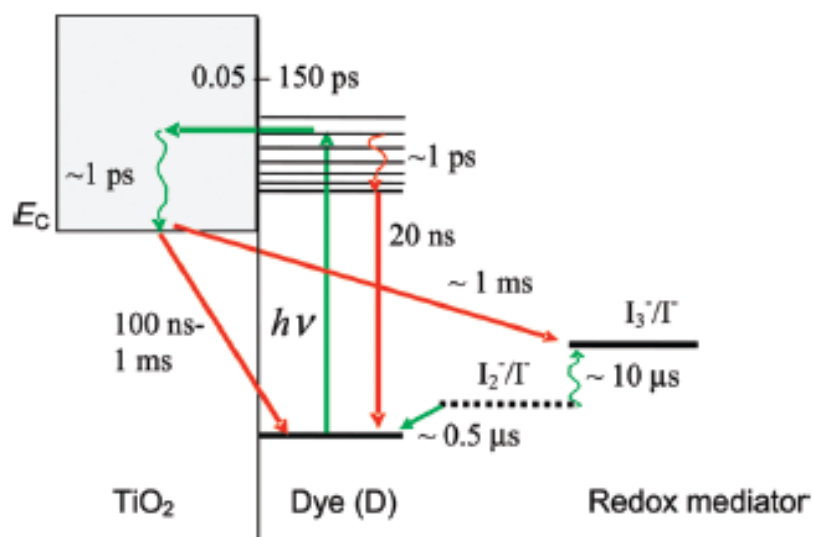
Figure 1.5. Kinetics of the dye-sensitized solar cell with I^-/I_3^- redox couple.

The power conversion efficiency of liquid electrolyte-based DSCs has reached over 11 % with tuned dye molecules. At present, research on DSCs include to theoretical studies for further progress.

1. 2 Solid-State Dye-Sensitized Solar Cells (SSDSCs)

Dye-sensitized solar cells have numerous advantages such as cheap materials, simple manufacturing process, lightweight, and environmental-friendly technology, etc. However, liquid electrolyte-based devices have not attained wide-spread applications in the commercial market due to concerns of solvent leakage and corrosion problems from the iodide/triiodide redox couple. Many approaches to replace liquid electrolyte have been researched, for instance polymer electrolyte, ionic liquids, p-type semiconductors such as CuI or CuSCN and organic hole conductors[30-38]. Recently, the conversion efficiency of the SSDSC based on an organic hole conductor have achieved over 6 % PCE. These interesting results have stimulated research on the SSDSCs.

In this section, the structure of the SSDSC with an organic hole transporting material (HTM) and its key materials will be introduced.

1.2.1 Working mechanism of SSDSCs

SSDSCs possess a monolithic structure in contrast to the sandwich design of the liquid electrolyte-based DSCs. In Figure 1.6, the other processes such as photoexcitation of sensitizer, electron injection and dye regeneration are the same as in the liquid electrolyte-based DSC: the only different part is that hole transfer takes place directly from the dye to the HTM, and then the hole is transported via hopping to the counter electrode.

Figure 1.6. Scheme for the electron transfer processes of the SSDSC.

1.2.2 Main components

Photoanode

The photoanode is related to light harvesting, electron injection and collection as well as undesirable electron recombination. The ideal photoanode, made most typically from a nan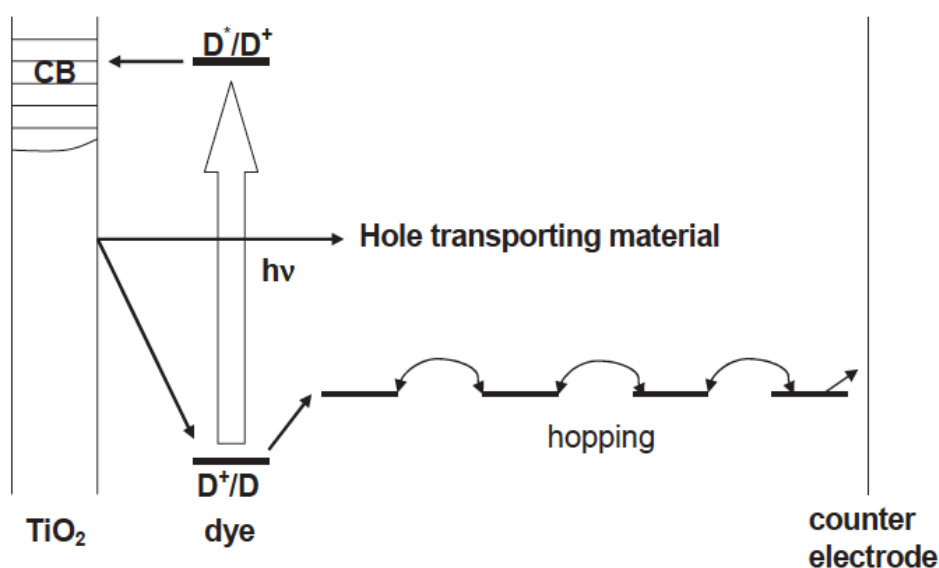oporous semiconducting oxide layer, is required to have high specific surface area for dye adsorption and good interconnection between nanoparticles.

Blocking layer

In contrast to the liquid cell, the HTM could permeate through the pores of the TiO_2 to form an ohmic contact with the FTO substrate. This would lead to a short circuit and loss of current through recombination at the FTO electrode. A blocking layer at the interface between the HTM and the FTO is necessary to avoid direct contact. Here a compact TiO_2 layer has been employed between the nanocrystalline TiO_2 and FTO layer by spray pyrolysis. The optimized thickness of compact layer for our SSDSCs is around 100nm. When the compact layer is too thick, it hinders electrons from reaching the anode, which lowers cell performance[39, 40].

Mesoporous TiO_2 films

In a typical DSC device, the size of TiO_2 particles is around 20nm and normally colloidal TiO_2 dispersions are applied to deposit nanocrystalline TiO_2 films on FTO substrate. There are two methods to make a TiO_2 paste: a sol-gel procedure from titanate[41] and using commercial TiO_2 particles[42]. For the deposition of the TiO_2 layer, screen-printing and doctor-blading techniques are widely used. After coating TiO_2 on the substrate, annealing at 450 ºC ~ 550 ºC is required to remove organic additives and afford good interconnection between the TiO_2 particles.

The breakthrough in DSC technology was due to the TiO_2 film, which had a mesoporous semiconductor structure instead of a flat electrode. The mesoporous TiO_2 films provide a surface area more than 1000-times greater compared to a flat electrode. Moreover, the open porosity of these films allows electrolyte to fill all pores of the film and make good contact with the dye molecules and electrolyte. However, the huge surface area also increases the recombination between electrons in the conduction band of the semiconductor and the electron acceptor in the electrolyte. Recently many interesting approaches have been applied to the TiO_2 surface in order to reduce interfacial recombination losses. For example, using an organic spacer between dye and TiO_2 surface[43-46], TiO_2 surface passivation with semiconductors, which have higher conduction band edge than TiO_2[47-53] or electrodeposition of insulating polymer on its surface, etc.

In general, liquid electrolyte-based cells use a thick mesoporous TiO_2 layer, roughly 10 to 20 μm thickness. However, SSDSCs based on organic hole transporting material can use only a 2 to 3μm thick film because the HTM cannot fill every pore of the TiO_2 when the film is too thick. This results in a limitation to achieve high photocurrent because of less dye loading and partial pore infiltration of

HTM. The film thickness, pore-filling problem of the HTM[54-57] and charge recombination between the electron from the TiO_2 and the HTM are the main drawbacks preventing highly efficient device performance.

Sensitizer

The sensitizer is an essential component to absorb light in the DSC, converting the incident light into photocurrent. Its properties have much effect on the light harvesting efficiency and the overall power conversion efficiency. The role of the sensitizer is not only light harvesting but also charge injection. The following properties are required for the ideal sensitizer. First it should cover a wide range of the solar spectrum for high photocurrent. Second, it must have attachment groups such as carboxylate or phosphonate to graft itself on the TiO_2 surface and to inject electrons from the excited dye to the TiO_2 conduction band. In addition, a dye with high molar extinction coefficient is advantageous to absorb more light with a thinner TiO_2 film, particularly in the SSDSC device. Finally, it should sustain its photoactive property at least 20 years of operation under illumination.

The sensitizer can be divided into inorganic-based dye (including semiconductor sensitizer) and organic dye according to the structure. Ruthenium and osmium complex sensitizers are the representative inorganic dyes and their properties have been investigated and improved systematically. Over the last few years quantum dots have raised interest as light absorbers in DSC devices because of their unique opto-electronic properties[11]. There are also many publications on purely organic dyes with good photovoltaic performance. Organic dyes are easy to synthesize, tune their properties and they have lower cost compared with ruthenium sensitizers.

The film thickness is a critical point in our SSDSC device, therefore a high extinction coefficient dye can enhance photocurrent and leads to higher overall efficiency with small amount of dye. The specific features and recent trends of sensitizers will be introduced in the following chapters.

Hole transporting material

The HTM should be able to transfer holes from the dye after the dye has injected electrons in the TiO_2. Several criteria have to be considered for the material to function as a good HTM. For efficient dye regeneration, the upper edge of the HTM valence band must be located above the ground state level of the dye. Moreover, the HTM must have a good contact with porous TiO_2 layer by penetrating into the pores of the nanoparticle film, and finally it should be transparent to the visible spectrum, where the dye absorbs light. There are two types: organic and inorganic HTM.

CuI[52, 58, 59] and $CuSCN$[60-62] are the representative inorganic HTMs. These copper-based materials can be cast from solution or vacuum deposition to form a complete hole-transporting layer. Also they have good conductivity over 10^{-2} S/cm, which facilitates their hole conducting ability. They showed relatively good power conversion efficiencies over 2 % when used in a SSDSC. However, the SSDSC

devices based on these inorganic hole conductors have problems such as instability, crystallization on TiO$_2$ film surface before penetrating into the pores and insufficient pore-filling.

Organic HTMs possess the advantages of low crystallinity, easy film formation and plentiful sources. The first efficient SSDSC using organic HTM, 2,2',7,7'-tetrakis(N,N-di-p-methoxyphenyl-amine)9,9'-spirobifluorene (spiro-OMeTAD) was reported by Udo *et al.* in 1998[63]. Utilization of additives, Li(CF$_3$SO$_2$)$_2$N and 4-*tert*-butylpyridine, in spiro-OMeTAD solution increased the short circuit current and the open circuit voltage and led to an enhancement of the power conversion efficiency in SSDSCs[64]. Recently, a SSDSC based on spiro-OMeTAD achieved the highest efficiency of over 6 % with a high extinction coefficient organic dye.

Conducting Polymers such as poly(3-hexylthiophene) (P3HT)[65-68] and poly(3,4-ethylenedioxythiophene) (PEDOT)[69-72] also have been employed as a HTM. Normally polymers have a large molecular size. This factor may have an influence on pore-filling of polymer. To avoid an infiltration problem of polymer, in situ polymerization of monomers has been reported by Yanagida. Lately, Liu *et al.* reported remarkably improved efficiency of over 6 % based on in-situ polymerized PEDOT with organic dyes[73]. However, the overall efficiency in a similar device with a Z907 dye, a ruthenium sensitizer, was much lower than that of the device sensitized with the organic dye.

SSDSCs employing spiro-OMeTAD have shown by far the best performance, but the PCE of this system is still lower than liquid electrolyte-based DSC. To improve their performance, these problems have to be resolved: 1) low hole mobility of spiro-OMeTAD, 2) high recombination between TiO$_2$ and HTM, 3) incomplete pore-filling into the pores of nanocrystalline TiO$_2$ film.

Counter electrode

The counter electrode should have a high conductivity, mechanical stability and chemical/electrochemical stability. Also, a large work function is required to be matched with the HTM. In general, noble metals such as gold and platinum have a large work function, and gold is typically used as a counter electrode in our SSDSCs. Silver is also a good candidate because of its high reflectivity, which reflects the incident light back on to the TiO$_2$ layer and improve the utilization of light. Snaith *et al.* reported enhanced photocurrent and overall efficiency by incorporating a silver counter electrode[74]. With regard to low cost, graphite and conducting polymers are also considered. Another interesting material is ITO, which is a transparent conducting material[75]. Chen demonstrated the SSDSC device with an ITO counter electrode having around 2 % efficiency by using a sputtering method for the ITO layer. The SSDSC device with a transparent counter electrode can be used for tandem devices and a transparent application such as a power window.

1.2.3 Efficiency limit of SSDSCs

Charge recombination

Charge recombination occurs easily in SSDSCs due to the high proximity of electrons and holes throughout the networks and the lack of substantial potential barrier at the interface. As a result, it is a main loss factor and leads to a low fill factor and open circuit voltage loss. The charge recombination between the oxidized dye molecule and the injected electron into TiO_2 is negligible in SSDSCs, since the oxidized dye molecule is regenerated by the HTM at a high rate, typically at the nanosecond time scale. There is another kind of charge recombination between injected electrons in the TiO_2 and holes in the HTM, and this back reaction takes place dominantly in SSDSCs.

Surface modification of the nanocrystalline TiO_2 layer is a versatile technique to suppress charge recombination. One of the most researched ways is the TiO_2 surface coating with insulator such as ZrO_2[50], ZnO[52], or MgO[47] to retard the recombination[76]. The insulating layer can block the access of holes to recombination centers on the TiO_2 surface. Instead of an insulator, using a co-adsorbent with the dye can make the same effect by creating an insulating thin layer. Recently, Wang *et al.* reported effectively reduced recombination using 4-guanidinobutryc acid (GBA) as a co-adsorbent with Z907 sensitizer in the SSDSC device[46]. Dye designs such as donor-antenna dye or dipolar dye molecule also have an influence on the charge recombination by controlling charge transfer dynamics.

Poor pore-filling

The filling fraction of spiro-OMeTAD is only 60 % in 2.5 µm TiO_2 film and the fraction gets lower in thicker films[55]. The insufficient pore-filling of spiro-OMeTAD causes lower photocurrent and poorer performance under full sunlight and faster recombination as well. Not only does it lead to those problems but also it inhibits the use of thicker TiO_2 films. The optimum TiO_2 thickness is only 2 µm in SSDSCs based on spiro-OMeTAD. To improve the power conversion efficiency, basically thicker TiO_2 film is necessary to achieve good optical absorption.

Few approaches have been undertaken to characterize and improve pore-filling in thicker TiO_2 films more than 3 µm[77]. Commonly a spin coating method is used to deposit spiro-OMeTAD on TiO_2 films. Recently, Ding *et al.* reported doctor-blading techniqued to deposit HTM layer and the pore-filling in TiO_2 film thickness of 5 µm was improved from 41 % to 53 % compared with spin coating method[78]. However, it is still quite low fraction. Dyes having similar functional group to methoxyphenyl amine group on spiro-OMeTAD could have a favorable contact between dye molecules and HTM, and this good contact can lead to better pore-filling.

1. 3 Objectives of The Present Work

The photovoltaic performances of the solid-state dye-sensitized solar cells based on spiro-OMeTAD have been progressed by applying new materials, optimization of device components and fundamental studies. The objective of the present work is basically to improve the power conversion efficiency of the SSDSC device. This work focuses on the photovoltaic performance of SSDSCs using diverse light absorbing materials, especially high extinction ruthenium sensitizers and organic dyes. The semiconductor sensitizer is also evaluated as alternative light absorbing materials instead of molecular sensitizers. In the last chapter, conducting polymer is employed to porphyrin sensitized solid-state solar cells and the photovoltaic performance of the conducting polymer based SSDSCs is made a comparison with that of spiro-OMeTAD based SSDSCs.

Bibliography

1.   BP, Statistical Review of World Energy (2010).

2.   W. Siemens, Van Nostrand's Eng. Mag. **32**, 392 (1885).

3.   M. Green, Journal of Materials Science: Materials in Electronics **18** (0), 15-19 (2007).

4.   M. Green, Third Generation Photovoltaics: Advanced Solar Energy Conversion (2003).

5.   A. L. A. Martí, Next generation photovoltaics: high efficiency through full spectrum utilization, Series in Optics and Optoelectronics (2003).

6.   G. Conibeer, Materials Today **10** (11), 42-50 (2007).

7.   M. A. Green, Progress in Photovoltaics: Research and Applications **9** (2), 123-135 (2001).

8.   M. D. McGehee, MRS Bulletin **34** (2), 95-100 (2007).

9.   M. Grätzel, Nature **414** (6861), 338-344 (2001).

10.   T. Trupke, M. A. Green and P. Wurfel, J Appl Phys **92** (7), 4117-4122 (2002).

11.   S. Rühle, M. Shalom and A. Zaban, ChemPhysChem **11** (11), 2290-2304 (2010).

12.   K. M. Coakley and M. D. McGehee, Chemistry of Materials **16** (23), 4533-4542 (2004).

13.   G. Yu and A. J. Heeger, J Appl Phys **78** (7), 4510-4515 (1995).

14.   Y. Liang, Z. Xu, J. Xia, S. T. Tsai, Y. Wu, G. Li, C. Ray and L. Yu, Adv Mater **22** (20), E135-E138 (2010).

15.   B. Thompson and J. Fréchet, Angewandte Chemie International Edition **47** (1), 58-77 (2008).

16.   S. R. Forrest, MRS BULLETIN **30**, 28-32 (2005).

17.   S. Günes, H. Neugebauer and N. S. Sariciftci, Chemical Reviews **107** (4), 1324-1338 (2007).

18.   B. O'Regan and M. Grätzel, Nature **353** (6346), 737-740 (1991).

19.   M. A. Green, K. Emery, Y. Hishikawa and W. Warta, Progress in Photovoltaics: Research and Applications **16** (5), 435-440 (2008).

20.   A. Hinsch, J. M. Kroon, R. Kern, I. Uhlendorf, J. Holzbock, A. Meyer and J. Ferber, Progress in Photovoltaics: Research and Applications **9** (6), 425-438 (2001).

21.   P. Wang, S. M. Zakeeruddin, J. E. Moser, M. K. Nazeeruddin, T. Sekiguchi and M. Grätzel, Nat Mater **2** (6), 402-407 (2003).

22.   P. Wang, C. Klein, R. Humphry-Baker, S. M. Zakeeruddin and M. Grätzel, Applied Physics Letters **86** (12), 123508-123503 (2005).

23.   J. H. Yum, D. Hagberg, S. J. Moon, K. Karlsson, T. Marinado, L. Sun, A. Hagfeldt, M. Nazeeruddin and M. Grätzel, Angewandte Chemie International Edition **48** (9), 1576-1580 (2009).

24.   H. Horiuchi, R. Katoh, K. Hara, M. Yanagida, S. Murata, H. Arakawa and M. Tachiya, The Journal of Physical Chemistry B **107** (11), 2570-2574 (2003).

25.   M. Law, L. E. Greene, J. C. Johnson, R. Saykally and P. Yang, Nat Mater **4** (6), 455-459 (2005).

26.   M. Quintana, T. Edvinsson, A. Hagfeldt and G. Boschloo, The Journal of Physical Chemistry C **111** (2), 1035-1041 (2006).

27.   K. Tennakone, P. K. M. Bandaranayake, P. V. V. Jayaweera, A. Konno and G. R. R. A. Kumara, Physica E: Low-dimensional Systems and Nanostructures **14** (1-2), 190-196 (2002).

28.   M. Grätzel, Accounts of Chemical Research **42** (11), 1788-1798 (2009).

29.   G. Boschloo and A. Hagfeldt, Accounts of Chemical Research **42** (11), 1819-1826 (2009).

30.   U. Bach, D. Lupo, P. Comte, J. E. Moser, F. Weissortel, J. Salbeck, H. Spreitzer and M. Grätzel, Nature **395** (6702), 583-585 (1998).

31.   J. Bandara and H. Weerasinghe, Solar Energy Materials and Solar Cells **85** (3), 385-390 (2005).

32.   J. Hagen, W. Schaffrath, P. Otschik, R. Fink, A. Bacher, H. W. Schmidt and D. Haarer, Synth. Met. **89** (3), 215-220 (1997).

33.   A. Konno, T. Kitagawa, H. Kida, G. R. A. Kumara and K. Tennakone, Curr. Appl. Phys. **5** (2), 149-151 (2005).

34.   B. O'Regan and D. T. Schwartz, J. Appl. Phys. **80** (8), 4749-4754 (1996).

35.   R. Senadeera, N. Fukuri, Y. Saito, T. Kitamura, Y. Wada and S. Yanagida, Chem. Commun. (17), 2259-2261 (2005).

36.   K. Tennakone, G. R. R. A. Kumara, A. R. Kumarasinghe, K. G. U. Wijayantha and P. M. Sirimanne, Semicond. Sci. Technol. **10** (12), 1689-1693 (1995).

37.   B. Li, L. Wang, B. Kang, P. Wang and Y. Qiu, Solar Energy Materials and Solar Cells **90** (5), 549-573 (2006).

38.   A. F. Nogueira, C. Longo and M. A. De Paoli, Coordination Chemistry Reviews **248** (13-14), 1455-1468 (2004).

39.   L. Kavan and M. Grätzel, Electrochimica Acta **40** (5), 643-652 (1995).

40.   B. Peng, G. Jungmann, C. Jäger, D. Haarer, H.-W. Schmidt and M. Thelakkat, Coordination Chemistry Reviews **248** (13-14), 1479-1489 (2004).

41.   M. K. Nazeeruddin, A. Kay, I. Rodicio, R. Humphrybaker, E. Muller, P. Liska, N. Vlachopoulos and M. Grätzel, Journal of the American Chemical Society **115** (14), 6382-6390 (1993).

42.   S. Ito, P. Chen, P. Comte, M. K. Nazeeruddin, P. Liska, P. Péchy and M. Grätzel, Progress in Photovoltaics: Research and Applications **15** (7), 603-612 (2007).

43.   J. Krüger, U. Bach and M. Grätzel, Adv Mater **12** (6), 447-451 (2000).

44.   N. Kopidakis, N. R. Neale and A. J. Frank, The Journal of Physical Chemistry B **110** (25), 12485-12489 (2006).

45.   Z. Zhang, N. Evans, S. M. Zakeeruddin, R. Humphry-Baker and M. Grätzel, The Journal of Physical Chemistry C **111** (1), 398-403 (2006).

46.   M. Wang, C. Grätzel, S. J. Moon, R. Humphry-Baker, N. Rossier-Iten, S. M. Zakeeruddin and M. Grätzel, Adv Funct Mater **19** (13), 2163-2172 (2009).

47.   H. S. Jung, J.-K. Lee, M. Nastasi, S.-W. Lee, J.-Y. Kim, J.-S. Park, K. S. Hong and H. Shin, Langmuir **21** (23), 10332-10335 (2005).

48.   A. Kay and M. Grätzel, Chemistry of Materials **14** (7), 2930-2935 (2002).

49.   G. R. R. A. Kumara and et al., Journal of Physics D: Applied Physics **34** (6), 868 (2001).

50.   D. B. Menzies, Q. Dai, Y.-B. Cheng, G. P. Simon and L. Spiccia, Comptes Rendus Chimie **9** (5-6), 713-716.

51.   E. Palomares, J. N. Clifford, S. A. Haque, T. Lutz and J. R. Durrant, J Am Chem Soc **125** (2), 475-482 (2002).

52.   K. Tennakone, G. R. R. A. Kumara, I. R. M. Kottegoda and V. P. S. Perera, Chemical Communications (1), 15-16 (1999).

53.   J.-H. Yum, S. Nakade, D.-Y. Kim and S. Yanagida, The Journal of Physical Chemistry B **110** (7), 3215-3219 (2006).

54.   L. Schmidt-Mende and M. Grätzel, Thin Solid Films **500** (1-2), 296-301 (2006).

55.   I. K. Ding, N. Tetreault, J. Brillet, B. E. Hardin, E. H. Smith, S. J. Rosenthal, F. Sauvage, M. Grätzel and M. D. McGehee, Adv Funct Mater **19** (15), 2431-2436 (2009).

56.   J. Kroeze, N. Hirata, L. Schmidt-Mende, C. Orizu, S. Ogier, K. Carr, M. Grätzel and J. Durrant, Adv Funct Mater **16** (14), 1832-1838 (2006).

57.   J. S. Henry and et al., Nanotechnology **19** (42), 424003 (2008).

58.   P. M. Sirimanne and et al., Semiconductor Science and Technology **18** (7), 708 (2003).

59.   G. R. A. Kumara, S. Kaneko, M. Okuya and K. Tennakone, Langmuir **18** (26), 10493-10495 (2002).

60.   B. O'Regan, F. Lenzmann, R. Muis and J. Wienke, Chemistry of Materials **14** (12), 5023-5029 (2002).

61.   B. O'Regan and D. T. Schwartz, Chemistry of Materials **7** (7), 1349-1354 (1995).

62.   Y. Itzhaik, O. Niitsoo, M. Page and G. Hodes, Journal of Physical Chemistry C **113** (11), 4254-4256 (2009).

63.   U. Bach, D. Lupo, P. Comte, J. E. Moser, F. Weissortel, J. Salbeck, H. Spreitzer and M. Grätzel, Nature **395** (6702), 583-585 (1998).

64.   J. Kruger, R. Plass, L. Cevey, M. Piccirelli, M. Grätzel and U. Bach, Applied Physics Letters **79** (13), 2085-2087 (2001).

65.   G. K. Mor, S. Kim, M. Paulose, O. K. Varghese, K. Shankar, J. Basham and C. A. Grimes, Nano Lett **9** (12), 4250-4257 (2009).

66.   Y.-Y. Lin, T.-H. Chu, C.-W. Chen and W.-F. Su, Applied Physics Letters **92** (5), 053312-053313 (2008).

67.   R. Zhu, C. Y. Jiang, B. Liu and S. Ramakrishna, Adv Mater **21** (9), 994-1000 (2009).

68.   M.-C. Wu, Y.-J. Wu, W.-C. Yen, H.-H. Lo, C.-F. Lin and W.-F. Su, Nanoscale **2** (8), 1448-1454 (2010).

69.   N. Fukuri, N. Masaki, T. Kitamura, Y. Wada and S. Yanagida, The Journal of Physical Chemistry B **110** (50), 25251-25258 (2006).

70.   Y. Saito, N. Fukuri, R. Senadeera, T. Kitamura, Y. Wada and S. Yanagida, Electrochemistry Communications **6** (1), 71-74 (2004).

71.   N. Fukuri, Y. Saito, W. Kubo, G. K. R. Senadeera, T. Kitamura, Y. Wada and S. Yanagida, Journal of The Electrochemical Society **151** (10), A1745-A1748 (2004).

72.   J. Xia, N. Masaki, M. Lira-Cantu, Y. Kim, K. Jiang and S. Yanagida, Journal of the American Chemical Society **130** (4), 1258-1263 (2008).

73.   X. Z. Liu, W. Zhang, S. Uchida, L. P. Cai, B. Liu and S. Ramakrishna, Adv Mater **22** (20), E150-+ (2010).

74.   H. J. Snaith, A. J. Moule, C. d. Klein, K. Meerholz, R. H. Friend and M. Grätzel, Nano Lett **7** (11), 3372-3376 (2007).

75.   P. Chen, Ph.D. Thesis, EPFL (Switzerland) (2009).

76.   Y. Diamant, S. Chappel, S. G. Chen, O. Melamed and A. Zaban, Coordination Chemistry Reviews **248** (13-14), 1271-1276 (2004).

77.   U. B. Cappel, E. A. Gibson, A. Hagfeldt and G. Boschloo, The Journal of Physical Chemistry C **113** (15), 6275-6281 (2009).

78.   I. K. Ding, J. Melas-Kyriazi, N. L. Cevey-Ha, K. G. Chittibabu, S. M. Zakeeruddin, M. Grätzel and M. D. McGehee, Org Electron **11** (7), 1217-1222 (2010).

Chapter 2

Experimental Methods and Device Preparation

This chapter is divided into two parts: the first section introduces employed materials and their properties, as well as assembling procedures of the SSDSCs. The second section describes characterization methods and their theoretical background.

2. 1 Materials

2.1.1 Conductive glass

Transparent conductive oxide coated glass (TCO glass) is employed as a substrate for SSDSC devices. For all experiments, Fluorine-doped-tin oxide (FTO) coated glass (TEC 15) purchased from Pilkington was used. The parameters of the TEC 15 are listed in Table 2.1.

	Resistance ($\Omega/\square$)	Transmittance at 550 nm (%)	Thickness (mm)
TEC 15	15	82	2.3

Table 2.1. Specific parameters of the conductive glass used for SSDSC devices.

2.1.2 Precursor solution for compact TiO$_2$ layer

Diisopropoxy-titaniumbis(acetylacetonate) (TAA, Aldrich) stored under Argon is diluted with ethanol to a concentration of 0.02M. The precursor solution is prepared fresh just before performing spray pyrolysis.

2.1.3 TiO$_2$ pastes

Four kinds of TiO$_2$ paste having different particle size were used for each experiment. Table 2.2 shows the properties of each paste. Acidic 20 and Basic 23 were prepared by P. Compte (LPI, EPFL) following a sol-gel process.[1] These were mainly employed for ruthenium or organic dye sensitized devices. The S30 and S75, having bigger particle size and pore size, were used for the other device systems to be discussed (i.e. semiconductor sensitizer and conducting polymer). Unlike Acidic 20 and Basic 23, they were prepared from commercial TiO$_2$ powders (Showa Denko K.K). The paste making procedure is described in reference.[2]

	Acidic 20	Basic 23	S30	S75
Particle size (nm)	20.0	23.0	30.0	75.0
Porosity (%)	65.0	67.0	65.3	32.6
Average Pore sizes (nm)	20.3	25.0	27.6	52.0

Table 2.2. The properties of used TiO$_2$ pastes for SSDSC devices.

2.1.4 Sensitizers

Ruthenium, organic and porphyrin sensitizers were used in this work. Their molecular structures will be shown in the following chapters. Except the Z907 sensitizer, ruthenium sensitizers, C101, C104 and C106, were synthesized by Prof. Wang's group (CAS, China). CYC-B1 was synthesized by Prof. Wu's group (NCU, Taiwan). Dr. Zakeeruddin (LPI, EPFL) prepared all dye solutions and purified the Z907 sensitizer, which is the reference sensitizer in our SSDSCs. Organic sensitizers, D5L6, D21L6 and D25L6, were synthesized by Prof. Sun's group (KTH, Sweden). Another organic dyes, C2, C6 and C12, were synthesized by Prof. Wang's group. We got near infrared absorbing dyes, SQ1 and SQ2, from Dr. Nüesch (Empa, Switzerland). The zinc porphyrin sensitizer, YD2, was provided by Prof. Yeh (NCHU, Taiwan).

2.1.5 Hole transporting materials and additives

Spiro-OMeTAD purchased from Merck was used as an organic hole transporting material (HTM) in dye sensitized devices. $Li(CF_3SO_2)_2N$ (LiTFSI, Aldrich) and 4-*tert*-butylpyridine (*t*BP, Fluka) were added to spiro-OMeTAD solution. Before using the *t*BP, it was purified by distillation and stored in a glove box. To study alternative SSDSCs, Poly(3-hexylthipene-2,5-diyl) (P3HT, Reike Metals, Inc.) and poly(3,4-ethylenedioxythiophene) (PEDOT, Aldrich) were employed to the devices as a polymer hole conductor. The molecular structures of all HTMs are listed in Appendix A2.

2. 2 Photovoltaic Device Fabrication

A general fabrication method of SSDSCs is described in this part. The specific cell assembly for semiconductor sensitized cells and devices based on polymer HTM will be explained in following chapters. A device schematic is shown in Figure 2.1.
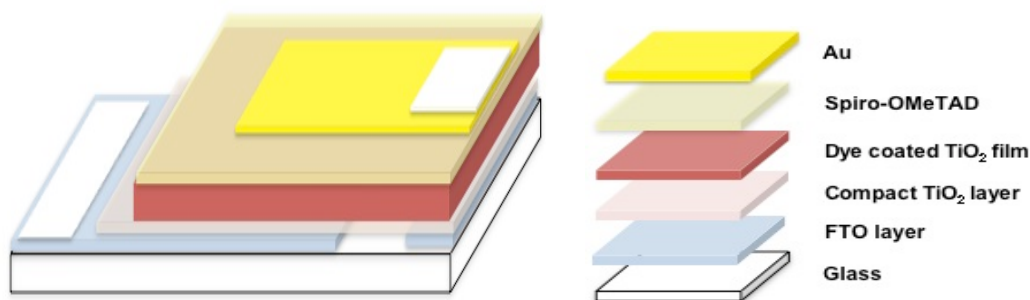

Figure 2.1. A device schematic of SSDSCs.

The SSDSC device has a monolithic structure and FTO glass is used for a substrate. Before cleaning FTO glass substrates, part of FTO layer was chemically etched away to avoid direct contact between the FTO layer and the Au electrode. Zn powders were spread on FTO layer, and then dropped 4 M HCl on Zn powders. The fast reaction between HCl and Zn powders completely removes FTO layer. Etched substrates were cleaned with acetone, Hellmanex[®] surfactant (2 % in H_2O) and ethanol, then dried out with air. Just before performing spray pyrolysis, the substrates were treated by UV/Ozone cleaner (UVO-Cleaner(R), Model No. 256-220, Jelight company Inc.) for 20 minutes.

The compact TiO_2 layer was deposited by spray pyrolysis method,[3] which was reported by Kavan *et al.* The substrates were heated to 450 ºC in 15 minutes and left for another 5 minutes to heat them evenly. The prepared 0.02 M TAA solution was sprayed through a spray head at a distance of about 20 cm over the glass substrates. Oxygen was used as a carrier gas. Glass slides were used to mask the

FTO surface where collecting contact was to be made. For layer of around 100 nm thickness, 16 spray cycles with an interval of 10 seconds were performed. After that, the substrates were annealed at 450 ºC for another 30 minutes to remove remaining organic substances.

Mesoporous TiO_2 films were deposited on compact TiO_2 layer by screen-printing and doctor-blading. Then they were sintered with a stepwise temperature program under oxygen flow (See Appendix B for sintering program). After cooling the substrates, a 0.02 M $TiCl_4$ solution was applied to the TiO_2 films for 6 hours at room temperature. Afterwards the substrates were rinsed with deionized water carefully and they were sintered again at 450 ºC for 30 minutes under oxygen flow. Figure 2.2 shows a substrate schematic displaying the included layers. Usually 12 pieces of TiO_2 films with a size of 0.7 cm x 0.7 cm were printed on a big substrate (5 cm x 10 cm).

For sensitization, the TiO_2 films were sintered again at 500 ºC for 30 minutes to remove water and dust. After cooling to 80 ºC, they were immersed into a dye solution. The concentration of dye solution can vary according to sensitizers. Normally the concentration for ruthenium sensitizer is 0.3 mM in various organic solvents such as acetonitrile/*tert*-butyl alcohol mixture, ethanol and chlorobenzene, etc. Organic sensitizers have higher molar extinction coefficients compared to ruthenium dyes, therefore they generally require lower concentrations. Immersing time for sensitization is also different between ruthenium and organic dyes. It takes over 10 hours for ruthenium dyes, however it takes only few hours for organic dyes. After finishing sensitization, the dye-coated films were rinsed with same solvent, which was used for the dye uptake to remove extra and loosely attached dyes on the TiO_2 surface.
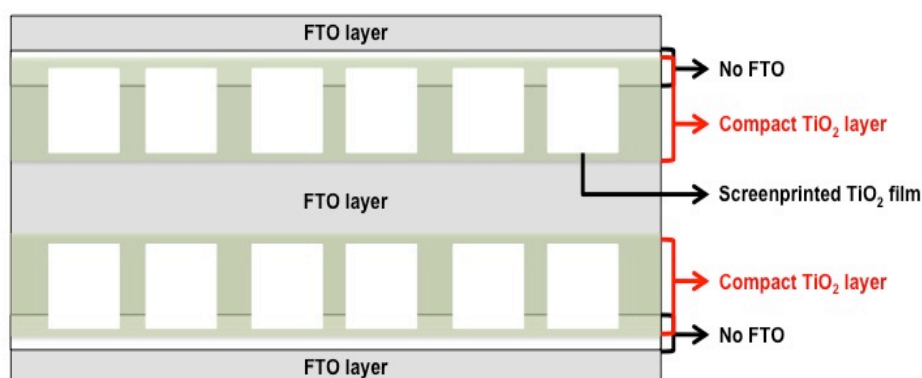

Figure 2.2. Scheme of the substrate including compact TiO_2 layer and mesoporous TiO_2 film.

The HTM solution is composed of spiro-OMeTAD (180 mg/ml in chlorobenzene) with additives LiTFSI (19.5 mM) and *t*BP (17.6 µl/ml). The spiro-OMeTAD solution was heated at 80 ºC for 30 minutes to dissolve it completely. Then *t*BP and LiTFSI, which was pre-dissolved in acetonitrile at 170 mg/ml, were added to the spiro-OMeTAD solution subsequntially. The HTM solution (40 µl) was

applied to the dye-stained TiO$_2$ film (area = 0.49 cm^2) and left for 45 seconds before spin coating at 2000 rpm for 30 seconds in air. After spin coating, the film was dried overnight in dry air box.

Thermal evaporation was used to deposit gold (100 nm) as a counter electrode. For high efficiency cells, silver (200 nm) was applied to the devices. The film deposition rate is important to acquire a good contact between the HTM and the counter electrode. The rate was less than 0.5 nm/sec for the first 20 nm then increased to over 1 nm/sec up to the desired thickness.

SSDSC devices are quite stable under atmosphere without light. However, materials such as sensitizer and HTM can be degraded by oxygen and humidity under light. Devices that were used for the long-term stability and characterization under light condition were sealed to minimize material degradation by protecting the active surface from atmosphere. For sealing, the active surface was covered by micro glass and sealed with a 25 µm thick Surlyn$^®$ by heating. After sealing the device, it was placed high vacuum of 10^{-6} mbar for 2 hours to remove moisture and oxygen remaining from the device preparation.

2. 3 Experimental Methods

2.3.1 Photovoltaic device characterization

Current-voltage measurement is a simple method to evaluate photovoltaic devices under both illumination and dark conditions. Figure 2.3 shows a typical I-V curve for a solar cell under illumination. The following parameters can be extracted from the I-V curve.
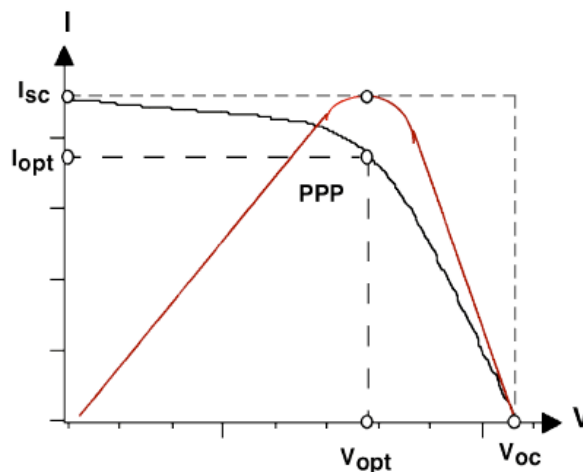

Figure 2.3. A representative I-V curve of a solar cell under illumination.

Short circuit current (I_{sc}): Cell current measured at an applied potential of zero volt, I_{sc} increases linearly with light intensity.

Open circuit voltage (V_{oc}): Cell potential measured when there is no external load. Under these conditions there is no external electric current between the terminals.

Fill Factor (*F.F.*): The fill factor is defined as the ratio

$$F.F = \frac{V_{max} \times I_{max}}{V_{oc} \times I_{sc}}.$$

The *F.F.* describes how a maximum power rectangle fits under the I-V characteristics. It is influenced by the series resistance (R_s) following from the internal resistance and shunt resistance (R_{sh}) from the leakage of current. A simplified equivalent circuit for a DSC including R_s and R_{sh} is shown in Figure 2.4. To obtain high *F.F.* R_s should be small, while R_{sh} needs to be as large as possible.
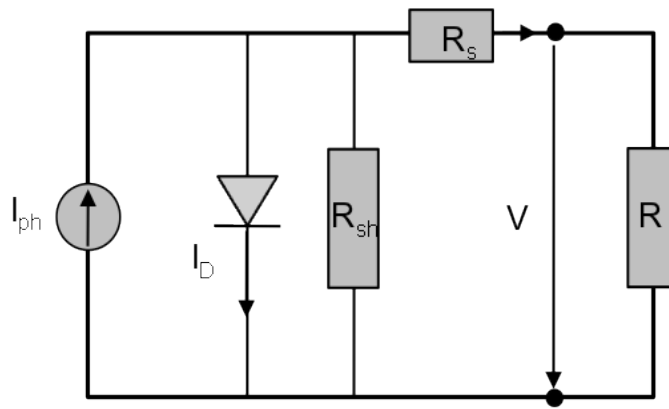

Figure 2.4. A simplified equivalent circuit for a DSC device.

Power conversion efficiency (*η*): The PCE is defined as the ratio of the maximum power output from a cell (P_{max}) to the incident radiation power (P_{in}).

$$\eta = \frac{P_{max}}{P_{in}} = \frac{V_{oc} \times I_{sc} \times F.F.}{P_{in}}$$

This parameter is equated to the performance of the DSC device. In order to compare different results, standard test condition should be used for measurements of all the devices. The standard condition specifies AM 1.5 spectrum illumination with an incident power density 100 mW/cm^2 at 298K. The Air Mass (AM) is the ratio of the path length of the sun light through the atmosphere when the sun is at a given angle θ the zenith, to the path length when the sun is at its zenith. This relation can be approximated by

$$AM = \frac{1}{\cos\theta}.$$

The standard condition is AM 1.5, which corresponds to a solar incident angle of 48° relative to the surface normal.

<u>Experimental set up</u>

The irradiation source was a 450 W xenon light source (Osram XBO 450, USA) with a filter (Shott 113), the power of which was regulated to 100 mW/cm^2 using a reference Si photodiode equipped with IR-cutoff filter (KG-3, Schott) to reduce the mismatch in the region of 350-750 nm between the simulated light and AM 1.5 to less than 4 %. Light intensity was changed with wire meshes in front of light source.

2.3.2 Incident photon-to-current conversion efficiency (IPCE)

The IPCE is defined as the ratio of the number of electrons generated in the device to the number of incident photons at a certain wavelength. It can be considered as the effective quantum yield of the device and is the product of three key factors: a) light harvesting efficiency (LHE), b) the charge injection yield (φ_{inj}) and c) the charge collection efficiency (η_{cl}).

$$IPCE = \frac{N_{electron}}{N_{photon}} = \frac{qN_{electron}/s}{qN_{photon}/s} = \frac{I_{ph}(amp)}{qN_{photon}/s}$$

$$= \frac{I_{ph}}{\dfrac{qP_{in}\lambda}{hc_0}} = \frac{I_{ph}}{P_{in}}\frac{hc_0}{q}\frac{1}{\lambda} = \frac{I_{ph}}{P_{in}} \times \frac{1240}{\lambda(nm)} \times 100\%$$

$$\left[\; P_{in}(Watt) = P_{in}\left(\frac{Joule}{s}\right) = \frac{N_{photons}}{s}h\nu = \frac{N_{photons}}{s}\frac{hc_0}{\lambda} \;\right]$$

<u>Experimental set up</u>

For the IPCE measurements the incident light from a 300 W xenon lamp (ILC Technology, USA) was focused through a Gemini-180 double monochromator (Jobin Yvon Ltd.) The spectral response of the test device was plotted as a function of excitation wavelength and it compared with the spectral response of Si photodiode of known IPCE spectrum.

2.3.3 Optical characterizations

<u>UV-Vis spectroscopy</u>

The UV-visible absorption spectra were measured with a Cary 5 spectrophotometer. The extinction coefficient and absorptivity can be determined using dye solutions or dye stained TiO$_2$ films.

<u>Fluorescence spectroscopy</u>

The steady state emission and emission dynamics were measured on a Horiba Jobin-Yvon Fluorolog3. The same optical detection channel was used to collect the light at right angles with respect to the excitation channel for both the steady state signal and the dynamic signal. The emission spectra were photometrically corrected. The emission lifetime was measured using the TRSPC

configuration, using a laser diode at 460 nm having a pulse width at FWHM of about 700 ps. The instrument time resolution is of the order of 50 ps.

2.3.4 Transient photocurrent and photovoltage decay measurements

The DSC's operation mechanism is based on competition between charge generation/separation and recombination. Photoexcitation and charge separation, *i.e.* electron injection in TiO$_2$ and dye regeneration in a DSC, create a photocurrent. In contrast, recombination eliminates the moving carriers and it normally increases with increasing carrier density. At a certain potential, recombination matches the photocurrent, and this equilibrium governs the open circuit voltage of the DSC. Therefore, retarding recombination is a crucial factor to improve the performance of DSCs. The electron lifetime reflects the basic kinetics of the recombination of electrons. In addition to the electron lifetime, the electron transport kinetics also strongly influence the device performance. There are many different techniques to investigate electronic properties of the device, for instance impedance spectroscopy[4, 5], V_{oc} decay method[6, 7] and small amplitude step time transient decay[8-10].

Transient photocurrent and photovoltage decay measurements are easily and quickly performed compared to impedance spectroscopy. Normally, the photovoltage decay closely follows a pseudo single exponential form, thus the recombination rate constant, κ_{rec}, can be extracted from the slope of a semi-logarithmic plot. Since the back reaction is usually taken as the pseudo-first order reaction, κ_{rec}, is related to electron lifetime τ_e by

$$\kappa_{rec} = 1/\tau_e$$

The recombination constant at short circuit conditions is determined by monitoring the transient photovoltage decay of the device under bias with a countercurrent equal to the short circuit current but in the opposite direction. The decay process is found to be very slow compared to the transport process under the short circuit condition.

From the photocurrent decay, the measured current decay rate (κ_{cur}) is the sum of both the charge transport rate (κ_{tr}) through the film and the recombination rate (κ_{rec}) between electron in TiO$_2$ and hole in HTM.

$$\kappa_{cur} = \kappa_{tr} + \kappa_{rec}$$

The electron diffusion coefficient D_n can be calculated from the electron transport rate by a three-dimension diffusion model

$$D_n = \frac{d^2 \kappa_{tr}}{C}$$

where d is the thickness of the mesoporous TiO$_2$ film and C is a constant with a value of about 2.35, which depends slightly on absorption coefficient of the film and direction of illumination[11]. The

electron diffusion length is given by the square root of the product of diffusion coefficient and electron lifetime[12, 13].

$$L = \sqrt{D_n \tau_e}$$

Furthermore, the total concentration of electrons in the mesoporous TiO_2 film under solar cell operating condition can be determined measuring the capacitance of the mesoporos film[8]. At a certain open circuit potential, obtained by bias illumination, a light flash is added and the resulting voltage rise is measured. The photocurrent transient resulting from the light flash is measured separately under short circuit conditions and used to calculate the injected charge induced by the light flash. The chemical capacitance is calculated as

$$C = \Delta Q / \Delta V$$

where ΔV is the peak of the transient and ΔQ is the number of electrons injected during the light flash.

The charge extraction method is also used for measuring the number of electrons in the TiO_2 film. In this method, the light is switched off and all remaining charges in the film are extracted as a current during a certain period of time and integrated to obtain the charge. Under short circuit conditions, this simply corresponds to the integration of the photocurrent transient recorded after the light is switched off[14, 15]. Starting from open circuit conditions, the cell connection has to switch from open circuit to short circuit while simultaneously switching off the light. When the open circuit voltage decay is measured in the dark for different periods before charge extraction, a complete charge-potential curve is obtained by repeated experiments[16].

These methods may underestimate the actual injected charge by the fraction of electrons due to recombination losses during transport and limitations in extraction time.

Experimental set up

White light bias was generated by an array of diodes (Lumiled Model LXHL-NWE8 whitestar) in combination with red light pulsed diodes (LXHLND98 redstar, 0.2 s square pulse, 100 ns rise and fall time) for the perturbation excitation, controlled by a fast solid-state switch. The voltage dynamics were recorded via a Keithley 2602 sourcemeter. The light source for the perturbation was set to a low light intensity to achieve monoexponential voltage decay kinetics. The voltage decay measurements were performed from zero current (V_{oc}) over a range of fixed currents intervals on the photocurrent–voltage curve to mimic the I-V characteristic of the device while measuring the transients. Small perturbation transient photocurrent measurements were performed in a similar way to the open-circuit voltage decay measurements but here holding a fixed potential while measuring the photocurrent transients. To check on the RC limitation of the measurement setup the pulse charge rate and the voltage decay rate were compared and showed no limitation.

2.3.5 Photoinduced absorption spectroscopy

Photoinduced absorption spectroscopy (PIA) is a useful method to study injection and regeneration processes in DSCs[17-19] because small changes in optical transmission are detected using a detector with a lock-in amplifier tuned at the frequency of the modulation. In a dye stained TiO_2 film without electrolyte, the absorption spectra of electrons in TiO_2 and of oxidized dye can be measured. In the presence of electrolyte, the spectrum of the oxidized electrolyte is seen instead of the spectrum of the oxidized dye. If the electrolyte is not able to regenerate the dye or not in contact with every dye molecule, the spectrum of the oxidized dye would still be observed in presence of the electrolyte due to a long lifetime of the oxidized state[18]. By analogy, if pores remain unfilled by spiro-OMeTAD, signals for the oxidized dye should be observed in the PIA spectrum[19, 20].

Experimental set up

The probe light source in this pump/probe technique was provided by a 10 W halogen lamp, which was focused onto the sample, with the transmitted light refocused onto the slits of a double monochromator (Gemini-180). The light intensity on the sample was ~65 μW/cm^2. A cooled dual-color solid-state detector (Si/InGaAs) was mounted on the exit slits of the monochromator to monitor the optical signal. To obtain the PIA spectrum, the pump source was provided by a Lumiled 470 nm diode that was modulated using the internal reference frequency of the lock-in amplifier. The pump light from this diode was focused onto the same face of the sample as the probe source but 20° off axis, with an approximate intensity of 6 mW/cm^2. A dual-phase lock-in amplifier (SR 830) was used to separate out the DC signal component from the AC signal coming from the pump source. The signal provided the change in transmission (ΔT) as a function of wavelength. As such, the plotted PIA spectra are shown as $\Delta T/T$, where ΔT is from the AC component, and T is derived from the DC signal. All the PIA measurements were performed in air.

Bibliography

1.   C. J. Barbé, F. Arendse, P. Comte, M. Jirousek, F. Lenzmann, V. Shklover and M. Grätzel, Journal of the American Ceramic Society **80** (12), 3157-3171 (1997).

2.   S. Ito, P. Chen, P. Comte, M. K. Nazeeruddin, P. Liska, P. Péchy and M. Grätzel, Progress in Photovoltaics: Research and Applications **15** (7), 603-612 (2007).

3.   L. Kavan and M. Grätzel, Electrochimica Acta **40** (5), 643-652 (1995).

4.   F. Fabregat-Santiago, J. Garcia-Canadas, E. Palomares, J. N. Clifford, S. A. Haque, J. R. Durrant, G. Garcia-Belmonte and J. Bisquert, J Appl Phys **96** (11), 6903-6907 (2004).

5.   F. Fabregat-Santiago, J. Bisquert, L. Cevey, P. Chen, M. K. Wang, S. M. Zakeeruddin and M. Grätzel, J Am Chem Soc **131** (2), 558-562 (2009).

6.   A. Zaban, M. Greenshtein and J. Bisquert, ChemPhysChem **4** (8), 859-864 (2003).

7.   J. Bisquert, A. Zaban, M. Greenshtein and I. Mora-Sero, J Am Chem Soc **126** (41), 13550-13559 (2004).

8.   B. C. O'Regan, S. Scully, A. C. Mayer, E. Palomares and J. Durrant, The Journal of Physical Chemistry B **109** (10), 4616-4623 (2005).

9.   S. Nakade, T. Kanzaki, Y. Wada and S. Yanagida, Langmuir **21** (23), 10803-10807 (2005).

10.   J. Nissfolk, K. Fredin, A. Hagfeldt and G. Boschloo, The Journal of Physical Chemistry B **110** (36), 17715-17718 (2006).

11.   J. van de Lagemaat and A. J. Frank, The Journal of Physical Chemistry B **105** (45), 11194-11205 (2001).

12.   J. Bisquert and V. S. Vikhrenko, The Journal of Physical Chemistry B **108** (7), 2313-2322 (2004).

13.   A. C. Fisher, L. M. Peter, E. A. Ponomarev, A. B. Walker and K. G. U. Wijayantha, The Journal of Physical Chemistry B **104** (5), 949-958 (2000).

14.   G. Boschloo and A. Hagfeldt, The Journal of Physical Chemistry B **109** (24), 12093-12098 (2005).

15.   J. van de Lagemaat, N. Kopidakis, N. R. Neale and A. J. Frank, Physical Review B **71** (3), 035304 (2005).

16.   N. W. Duffy, L. M. Peter, R. M. G. Rajapakse and K. G. U. Wijayantha, Electrochemistry Communications **2** (9), 658-662 (2000).

17.   G. Boschloo and A. Hagfeldt, Chemical Physics Letters **370** (3-4), 381-386 (2003).

18.   G. Boschloo and A. Hagfeldt, Inorg. Chim. Acta **361** (3), 729-734 (2008).

19.   U. B. Cappel, E. A. Gibson, A. Hagfeldt and G. Boschloo, The Journal of Physical Chemistry C **113** (15), 6275-6281 (2009).

20.   J. S. Henry and et al., Nanotechnology **19** (42), 424003 (2008).

Chapter 3

High Molar Extinction Coefficient Sensitizers – Ruthenium Sensitizers

3. 1 Introduction

Metal complex sensitizers usually have anchoring groups and ancillary ligands. Anchoring groups are responsible for the sensitizer adsorption onto the TiO_2 surface and facilitate the injection of the excited electron into the conduction band of the TiO_2. Ancillary ligands, typically bipyridines or terpyridines are not directly attached on the TiO_2 surface and can be used for tuning the overall properties by different substituents (alkyl, aryl, heterocycle, etc.)[1].

Among the metal complexes, ruthenium dyes have shown the best photovoltaic performance, since they have excellent properties such as a broad absorption spectrum, suitable excited and ground state energy levels, relatively long excited state lifetimes, and good stability[2]. Major improvements in cell efficiencies have been made through the development of new ruthenium complexes capable of absorbing well into the visible range and even into the near-infrared (IR) region, from approximately 400 to 900 nm[3].

In 1993, Grätzel and co-workers reported the dye [{(4,4'-CO_2H)$_2$bipy}$_2$Ru(NCS)$_2$], coded as N3[4], which showed outstanding power conversion efficiency of over 10 %. Using the N3 dye as a reference, many research groups have started to tune the electronic and optical properties by modifying ligands. Five key approaches are described in the following sections.

Different protonation level of N3 dye

Nazeeruddin *et al*[5]. investigated the effect of changing the number of protons on the N3 dye, ranging from zero proton (coded as N712) to four protons (N3). Here, the protons were replaced by a bulky tetra-*n*-butylammonium (TBA) group. By decreasing the number of protons, the oxidation and reduction potentials of the dye shifted to more negative potential in solution. The number of protons also influences the TiO_2 surface states and Fermi-level. The surface protonation can also affect the photocurrent and open circuit voltage. The photovoltaic performance of doubly-protonated sensitizer (coded as N719) was superior to that of sensitizers cantaining four or no protons.

Extending the spectral response of dyes

To improve the efficiency of DSCs, extending the spectral coverage of the sensitizer to the near-IR region is desirable. Sensitizers such as N3 and N719 have comparatively low IPCEs in the red and near-IR region. To develop better red-absorbing dyes, control of the HOMO and LUMO levels of a dye is required. However, the LUMO and HOMO of a dye should remain at levels where injecting electrons into the TiO_2 conduction band and regeneration of the dye by electrolyte can take place. In 2001, Grätzel and co-workers published panchromtic sensitizer, N749 dye, which was a terpyridyl-Ru complex[6]. The red-shift in the metal-to-ligand charge transfer (MLCT) band is due to the lowering of the π^* level of the terpyridine ligand and the raising of the energy of the t_{2g} metal orbital. The IPCE spectrum of the N749 was obtained over the whole visible range extending into the near-IR region up to 920 nm and a power conversion efficiency of 11.1 % was achieved[7].

Amphiphilic dyes with alkyl chains

Dyes adsorbed onto the TiO_2 surface through carboxylic acid groups are susceptible to desorption from water on the surface. This problem was resolved by introducing hydrophobic groups onto properties in the ligands. Dyes containing long alkyl chains such as Z907[8] and N621[9] showed excellent stability towards water-induced desorption from TiO_2. The Z907 sensitized DSCs did not degrade in performances when tested for 1000 hours at 80 °C in darkness and at 55 °C under full sunlight[10, 11]. The hydrophobic groups not only improve the stability but also retard charge recombination[12]. Furthermore, they can enhance the wettability of the TiO_2 by the hole transporting material (HTM) making better contact with the dye.

Different anchoring groups

Most of the sensitizers have carboxylic acid groups to anchor onto the TiO_2 surface. However, the resulting ester linkage between the dye and TiO_2 can be hydrolyzed by water. This is an important issue in terms of stability of the cell. An alternative anchoring group is the phosphonic acid moiety that binds even more strongly to TiO_2. In 2004, a Ru complex with a phosphonic acid anchoring group (Z955) was reported, which yielded a conversion efficiency of over 8 % accompanied by a good

stability under prolonged light-soaking (1000h at full sunlight and 55 °C). Besides the phosphonic acids, other anchoring groups have been investigated, but they do not show significant improvements in solar cell performance[13, 14].

Enhancing molar extinction coefficients

The ruthenium dyes have lower absorption coefficients compared to organic dyes. Therefore, thick TiO_2 layers are needed to harvest most of the incident light, which could increase electron recombination.

Recently, many research groups have focused on increasing the extinction coefficient and red response of the ancillary ligand. The dyes with high molar extinction coefficient can increase light harvesting of a given film thickness or thinner films can be used, which result in better efficiencies due to decreased losses during charge transport through the TiO_2 layer.

One strategy for increasing the light harvesting efficiency is to increase the conjugation length of the ligand. To this end, alkoxy group[15, 16] or conjugated electron rich units[17-19] such as alkyl thiophene, alkyl furan, or alkyl selenophene were recently investigated. Moreover, the DSCs based on these dyes showed excellent photovoltaic performances of over 10 %. The results suggest that there will be promising application in solid-state DSCs (SSDSCs) with these dyes. The SSDSC using spiro-OMeTAD as a HTM has a limitation of the thickness of the TiO_2 film due to poor infiltration[20] and limited charge carrier mobility of HTM. Therefore, enhancing light harvesting is a crucial issue in SSDSCs. The use of dyes having high molar extinction coefficient is desirable, leading to higher power conversion efficiencies.

In this chapter, ruthenium sensitizers with enhanced absorption coefficients will be applied to SSDSCs and their properties will be investigated by using optical and transient methods.

3. 2 Ruthenium Dyes Having High Molar Extinction Coefficient

Here, a family of high molar extinction coefficient heteroleptic polypyridyl ruthenium sensitizers (coded as C101, C104, C106 and CYC-B1) is introduced to improve the photovoltaic performance in SSDSCs. The Z907 dye is used as a reference sensitizer to compare with new sensitizers.

Figure 3.1 shows the molecular structures of the Z907 and the new high extinction coefficient sensitizers. All of these new sensitizers contain thiophene units. The thiophene unit between the alkyl chain and the pyridine unit enhances the molar extinction coefficient of the sensitizer by increasing the π-conjugation. The long alkyl chains help to promote pore-filling of the HTM due to their strong hydrophobicity, like for the Z907 sensitizer. Moreover, the presence of a long alkyl chain retarded charge recombination and increased electron lifetime by up to 9 times[21]. Compared to the Z907 dye, the MLCT transition of the new dyes is red-shifted and the molar extinction coefficients are dramatically enhanced. (see Table 3.1) The red-shifting and broadening behavior increase the photocurrent response region, resulting in the increase of photocurrent.
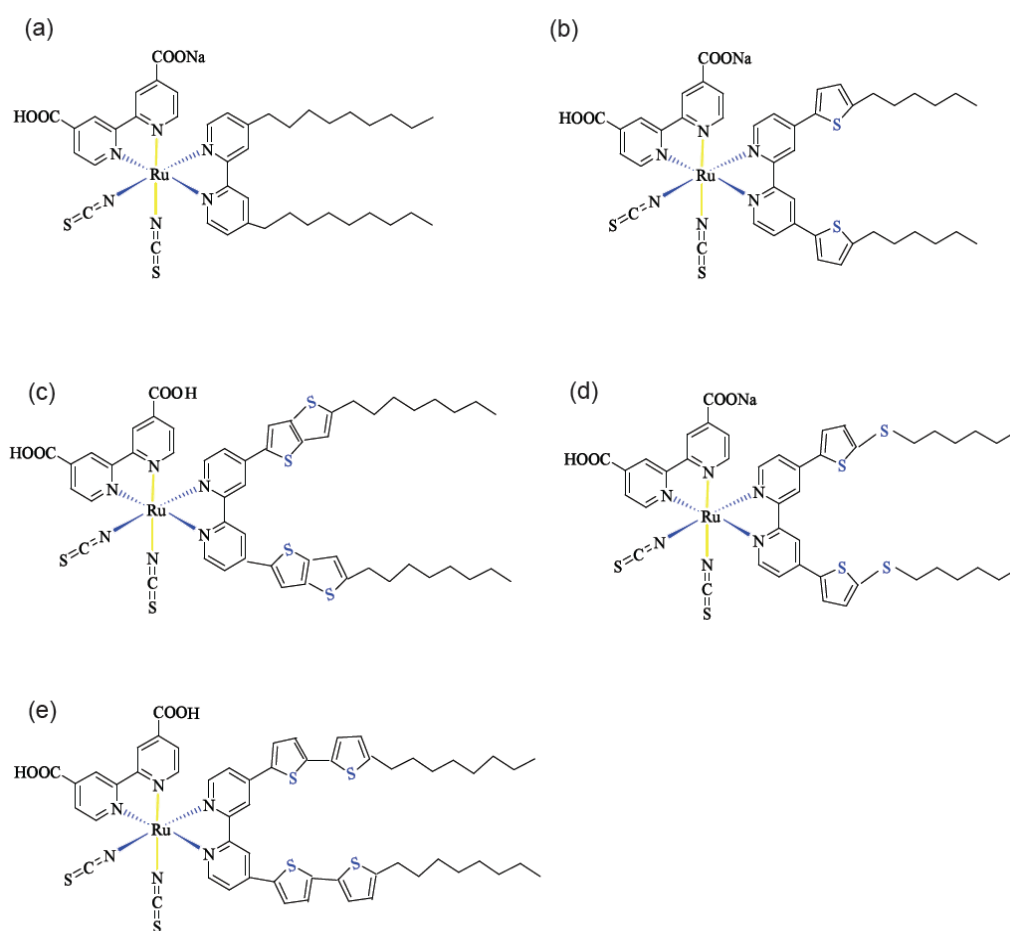

Figure 3.1. Molecular structures of (a) Z907, (b) C101, (c) C104, (d) C106 and (e) CYC-B1.

code	IUPAC name	molar extinction coefficient ($M^{-1}cm^{-1}$)
Z907	NaRu(4,4'-dinonyl-2,2'-bipyridine)(4-carboxylic acid-4'-carboxylate-2,2'-bipyridine) (NCS)$_2$	12,200 at 521 nm
C101	NaRu(4,4'-bis(5-hexylthiophen-2-yl)-2,2'-bipyridine)(4-carboxylic acid-4'-caboxylate-2,2'-bipyridine)(NCS)$_2$	17,500 at 547 nm
C104	cis-Ru(4,4'-bis(5-octylthieno[3,2-b]thiophen-2-yl)-2,2'-bipyridine)(4,4'-dicarboxyl-2,2'-bipyridine)(NCS)$_2$	20,500 at 553 nm
C106	Na Ru(4,4'-bis(5-(hexylthio)thiophen-2-yl)-2,2'-bipyridine)(4-carboxylic acid-4'-carboxylate-2,2'-bipyridine)(NCS)$_2$	18,700 at 550 nm
CYC-B1	cis-Ru(4,4'-bis-(4'-octyl-bithiophen-2-yl)-2,2'-bipyridine)(4,4'-dicarboxylicacid-2,2'-bipyridine)(NCS)$_2$	21,200 at 553 nm

Table 3.1. IUPAC names and molar extinction coefficients of Z907, C101, C104, C106 and CYC-B1 sensitizers.

3.2.1 C101 and C106 sensitizers

C101 and C106 dyes have excellent photovoltaic performances of over 11 % efficiency in liquid electrolyte-based DSC devices[17, 19]. C106 has almost the same structure as C101: a sulfur atom has been inserted between the hexyl and thiophene moieties. The addition of the sulfur atom between the hexyl and thiophene group extends the π-conjugated system of the ancillary ligand, which is clearly seen in the electronic absorptions[19]. In the UV-Vis spectrum (see Figure 3.2a), the C106 sensitizer shows the best absorptivity, compared to C101 and Z907. This enhancement of the light absorption by the C101 and C106 dyes in comparison to Z907 leads to improved light harvesting. Improvement of light harvesting is apparent from Figure 3.2b, which depicts the photocurrent action spectra of the devices sensitized with C101, C106 and Z907 sensitizers. The IPCEs of C101 and C106 sensitized devices were significantly enhanced in the yellow and red regions compared to that of the cell with Z907. The IPCE value of C106 was 56 % at 550 nm, which is slightly higher than the 50 % of the C101 dye at the same wavelength. The integrated current value was lower compared to the short circuit current measured under a xenon lamp. This mismatched current value between IPCE and J-V measurements arises from the nonlinearity of the current as a function of light intensity[22].
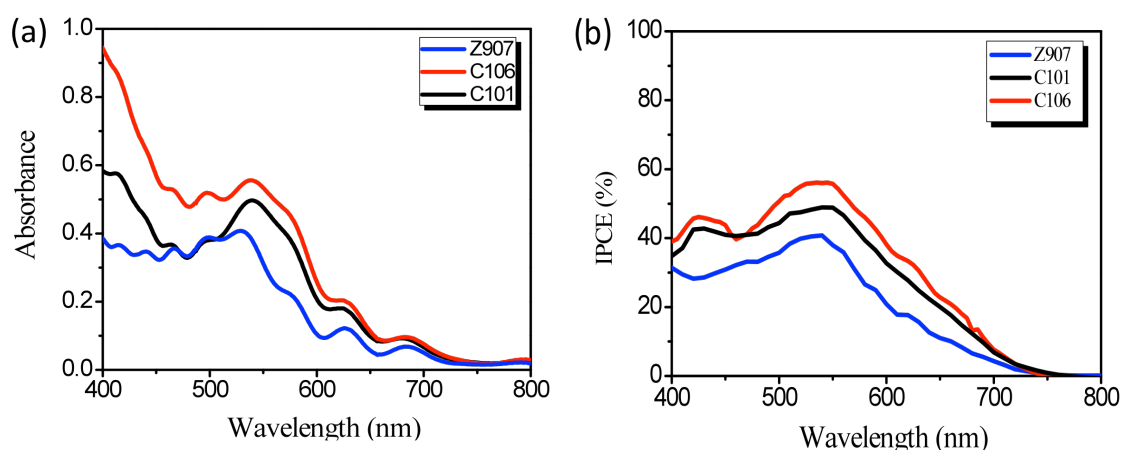
Figure 3.2. (a) UV-Vis spectrum of Z907 (blue), C101 (black) and C106 (red) stained on 2 μm thick mesoporous TiO$_2$ films. (b) Photocurrent action spectrum of the devices with Z907 (blue), C101 (black) and C106 (red).

Photocurrent-voltage characteristics for the C101 and C106 based SSDSC measured under simulated AM 1.5G sunlight are shown in Figure 3.3 and detailed photovoltaic parameters are summarized in Table 3.2. C101 and C106 based devices generate a higher open circuit voltage (V_{oc}) and a short circuit current density (J_{sc}) compared to the Z907 based device. Under similar conditions, the photovoltaic parameters of a Z907 based device were V_{oc} of 749 mV, J_{sc} of 5.67 mA/cm^2, and $F.F.$ of 0.68, yielding a lower photovoltaic conversion efficiency of 2.93 %[23]. There was no difference in the open circuit voltage between C101 and C106, however, the short circuit current density of the C106 sensitized device was 8.97 mA/cm^2, which was much higher than the 7.87 mA/cm^2 of C101. As a result, the overall power conversion efficiency of the device sensitized with C106 was also improved. Figure 3.4 illustrates a certified efficiency of 5 % (measured at the National Renewable Energy Laboratory (USA)), which is the highest efficiency of a ruthenium dye based solid-state solar cell.
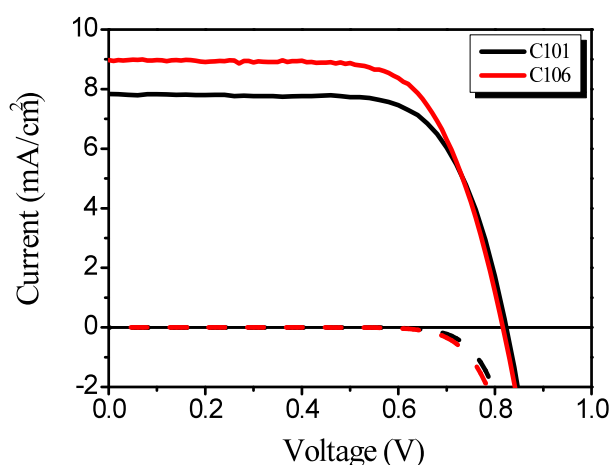

Figure 3.3. J-V characteristics of the devices with C101 (black curve) and C106 (red curve) under full sunlight (100 mW/cm^2). Dotted lines correspond to the dark current measurement.

sensitizer		J_{sc} (mA/cm^2)	V_{oc} (mV)	F.F.	η (%)
Z907		5.67	749	0.68	2.93
C101		7.87	823	0.69	4.60
C106	LPI	8.97	816	0.68	5.07
	NREL	8.27	848	0.71	4.99

Table 3.2. Photovoltaic parameters of devices with Z907, C101 and C106 under full sunlight (100 mW/cm^2).

The higher photocurrents observed in the C101 and C106 based devices can be explained by higher absorbance of the dye-sensitized TiO$_2$ films. The enhanced open circuit voltage (~70 mV) in C101 and C106 sensitized cells compared to that of the Z907 based cell could be either due to the reduction of electron-hole recombination or an upward shift of the conduction band edge position. Figure 3.5 illustrates electron lifetimes (τ_e) of SS DSCs with C101, C106 and Z907 as a function of charge density. As the charge density extracted from the TiO$_2$ films increases, the electron lifetimes (τ_e) become shorter due to higher electron densities found in the TiO$_2$ as well as to larger driving forces for interfacial recombination. Photovoltaic devices sensitized with C101 and C106 possessed almost the same electron lifetime, however, they both had longer electron lifetimes at an identical charge density compared to that derived for a Z907 device. These results indicate that higher open circuit voltage in the devices with C101 and C106 arises from the decrease of the recombination rate, which is in good agreement with results of the photovoltaic data.
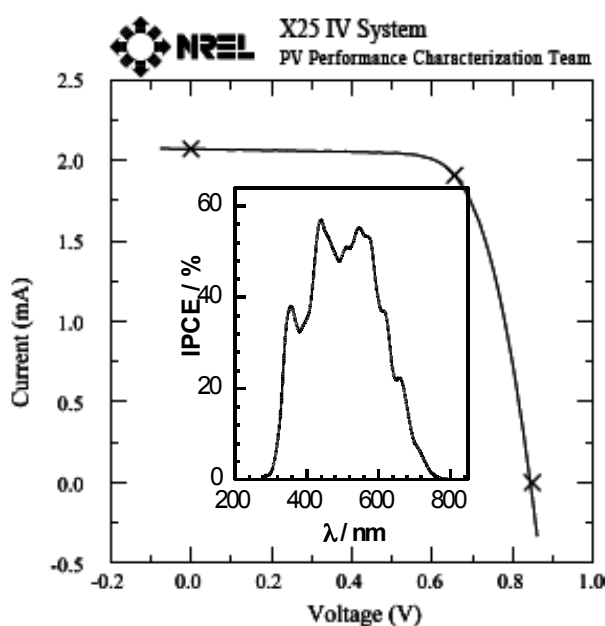

Figure 3.4. *J–V* characteristics of a SSDSC sensitized by C106 dye measured by the NREL photovoltaic calibration laboratory under standard reporting conditions, i.e. illumination with AM 1.5G sunlight (intensity 100 mW/cm^2) and 298 K temperature. The inset exhibits its photocurrent action spectrum. Cell active area tested (with a mask): 0.2505 cm^2.
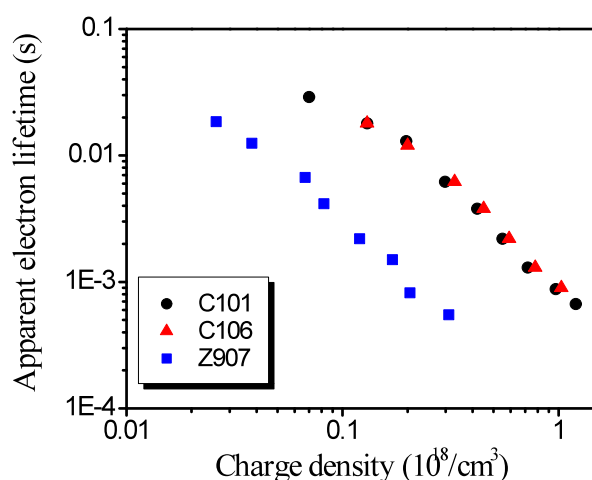
Figure 3.5. Apparent electron lifetime (τ_e) of SSDSCs sensitized with C101 (black), C106 (red) and Z907 (blue) from transient photocurrent and photovoltage decay measurements.

3.2.2 C104 sensitizer

C104 (see Figure 3.1c) is an analogue of the Z907Na dye, a thienothiophene unit being inserted between each hydrophobic alkyl chain and the pyridine ring[18]. Photocurrent-voltage characteristics for the C104 based SSDSC measured under simulated AM 1.5G condition are shown in Figure 3.6a. The open-circuit voltage (V_{oc}), short-circuit current density (J_{sc}), and fill factor ($F.F.$) are 813 mV, 8.39 mA/cm^2, and 0.69, respectively, yielding a photovoltaic conversion efficiency (η) of 4.67 %, which is improved photovoltaic performance compared to a Z907 sensitized SSDSC (V_{oc} 749 mV, J_{sc} 5.67 mA/cm^2, $F.F.$ 0.68, η 2.93 %[23]).

The advantage of using C104 dye over Z907Na is clearly reflected in the improved J_{sc} and V_{oc}, which lead to an improved photon-to-electricity conversion efficiency. The photocurrent action spectrum of the device with C104 shows that the IPCE peak is about 50 % near the absorption maximum of the dye, which is higher than that of Z907Na dye (see Figure 3.6b, left ordinate). The spectral response of the photocurrent closely follows the absorption spectra (see Figure 3.6b, right ordinate) of dye-coated mesoporous titania films. Higher IPCE in a C104-based device can be explained by the higher optical cross section of dye compared to Z907Na. The enhancement of the light harvesting by the C104 dye in comparison to Z907Na is clearly visible from this comparison.
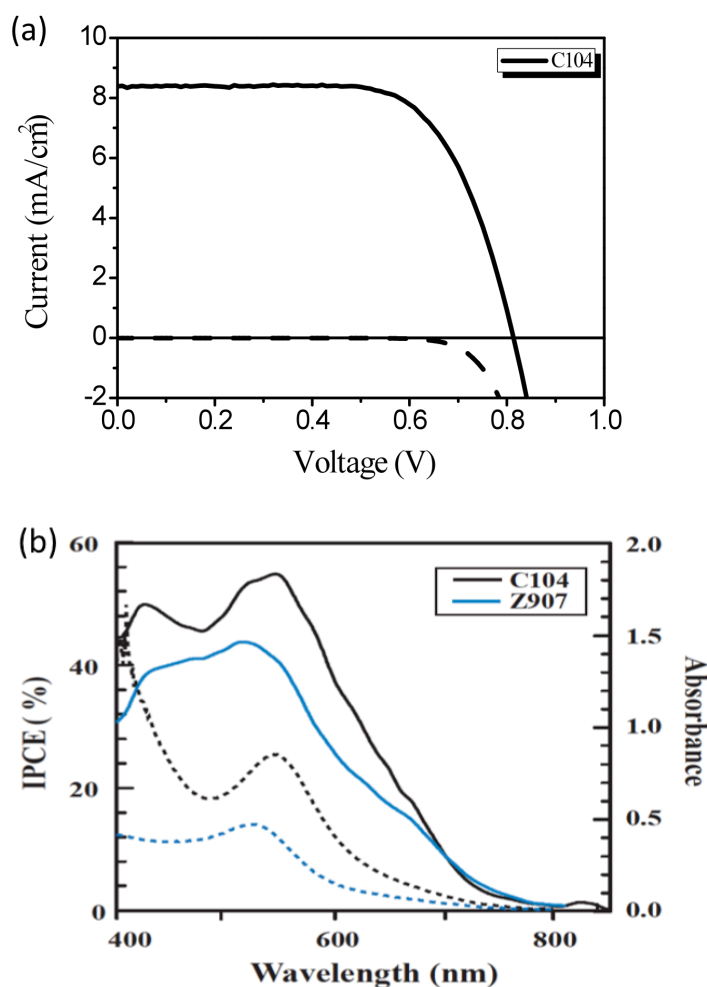
Figure 3.6. (a) *J*-V characteristics of the device sensitized with C104 under full sunlight (100mW/cm^2). Dotted line corresponds to the dark current measurement. (b) Left ordinate, the photocurrent action spectrum of SSDSCs with C104 (black, solid line) and Z907Na (blue, solid line): right ordinate, the UV-Vis absorption of C104 dye (black, dashed line) and Z907Na dye (blue, dashed line) anchored on 2 μm TiO$_2$ films.

The stability test was carried out in argon atmosphere under combined thermal stress (60 °C) and light-soaking (full sunlight intensity). The cell was sealed with micro glass to protect active area for the stability test. The hermetically sealed cell was put into a glass vial under argon atmosphere during the light-soaking test. The device was covered with a 50 μm thick polyester film, which acts as 460 nm cut off filter. Cells were exposed at open circuit to a Suntest CPS plus lamp (ATLAS GmbH, 100 mW/cm^2, 60 ^{o}C) over 1000 hours. The cells were taken out occasionally to check the *J*-V performance. Figure 3.7 shows the detailed evaluation of the device parameters during the aging period. The J_{sc}, V_{oc}, and *F.F.* of devices retain more than 80 % of their initial values. As a result, the overall photovoltaic efficiency remained at 3.2 % after aging for 1000 h. This relatively small decrease in the photovoltaic performance after 1000 h light-soaking test confirms the robustness of the TiO$_2$/dye/HTM heterojunction architecture.
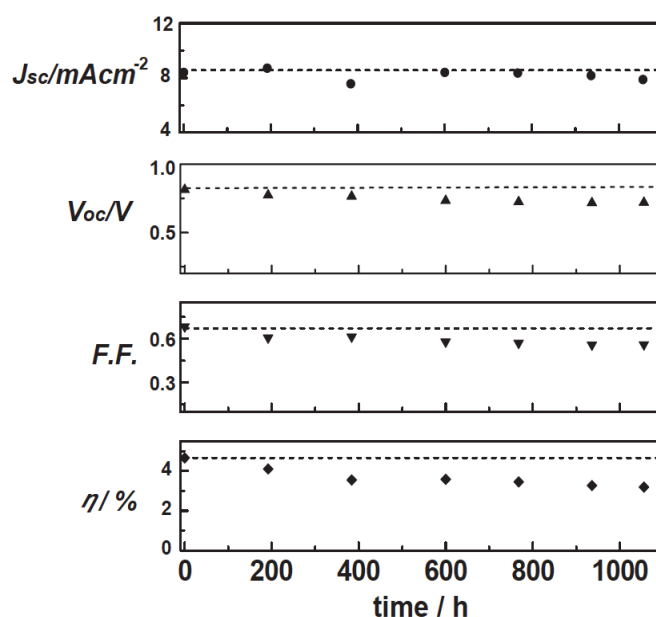
Figure 3.7. Variations of photovoltaic parameters (J_{sc}, V_{oc}, F.F., and η) with aging time for the device 1.7µm TiO$_2$ film sensitized with C104 during 1 sun visible light-soaking in argon atmosphere at 60 $^{\circ}$C.

During the prolonged light-soaking test the V_{oc} of the device decreased by approximately 100 mV (see Figure 3.7). The drop in the V_{oc} may be caused by the acceleration of electron–hole recombination or a downward shift of the conduction-band edge position. Our previous study on SSDSCs has demonstrated that charge recombination at the dye/HTM interface plays a decisive role for the cell efficiency[23, 24]. Figure 3.8a compares typical transient photovoltage curves of the fresh and aged cells at open-circuit voltage conditions under the same light intensity (1.86 mW/cm^2), serving as an illustrative example of the technique. The aged sample has faster photovoltage decay than the fresh one, indicating that the lower V_{oc} in the aged sample arises from an increase in the recombination rate. The recombination rate constant (k) value was determined by fitting the decay of the transient photovoltage to an exponential function. Figure 3.8b shows the recombination rate constant (k) of the fresh and aged SSDSCs prepared with C104 dye as a function of short circuit current. As presented in Figure 3.8b, the estimated recombination rate constant increases upon aging under identical short-circuit current conditions, which is consistent with the findings from impedance measurements, as discussed below, showing shorter electron lifetime values. We note similar slopes for the recombination rate constants of the fresh and aged cells in Figure 3.8b, indicating that the distribution function for electron trapping states in the TiO$_2$ film is similar for both devices.
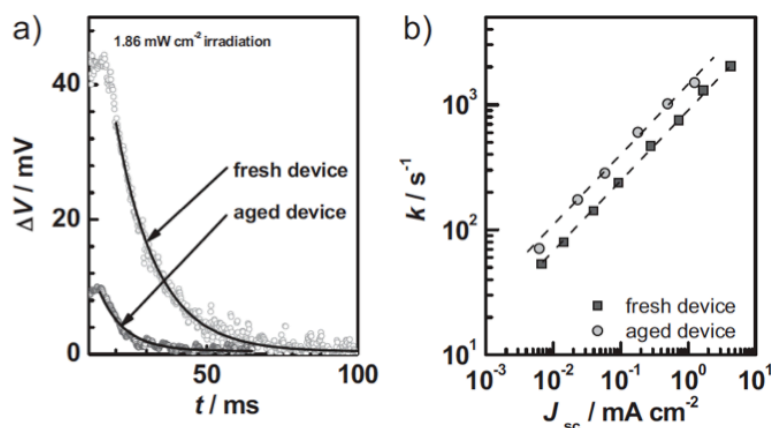
Figure 3.8. (a) Transient photovoltage decay measurements of the fresh SSDSC sensitized with C104 dye and its corresponding aged device after 1000 h 1 sun visible light-soaking at 60 ^{o}C: The transient photovoltage signals obtained in the small perturbation regime measured under 1.86 % sun illumination. The black lines are the corresponding fits for the decay processes. (b) Effect of light-soaking on the relationship between the short current density (J_{sc}) and the recombination rate constant (k).

As discussed above, contribution to the V_{oc} and J_{sc} of the sensitized heterojunction devices include the band offset between the donor and acceptor materials, the built in field due to the asymmetric contacts, and the effect of internal recombination in reducing the V_{oc}[23]. Electrochemical impedance spectroscopy (EIS) is useful to diagnose any changes in the individual electric circuit element of the device during the long-term light-soaking test. Using a small amplitude sinusoidal voltage applied to devices we have measured the frequency dependent response as a function of the applied bias voltage. Figure 3.9 depicts the Nyquist plot of the fresh C104 sensitized device at a forward bias of -0.7 V under illumination with one-fifth solar intensity (20 mW/cm^2). There are three distinct frequency ranges (a high frequency range from 1 MHz to 46.5 kHz, a middle frequency range from 46.5 kHz to 1.47 kHz and a low frequency range from 47.8 Hz to 2.12 Hz) analyzed in the Nyquist plot. These spectra obey the transmission line model, as suggested by Bisquert et al[25, 26]. Here the first arc resolved in the high frequency range of the Nyquist plot (i.e., from 1 MHz to 46.5 kHz) is assigned to the charge exchange process at the HTM (spiro-OMeTAD)/CE (Au) interface. A linear Warburg impedance feature appears in the intermediate frequency range (i.e., from 45.6 kHz to 1.47 kHz) corresponding to the transmission channel for the electron transport in the mesoscopic TiO$_2$ film. The low frequency range semi-circle (i.e. from 118 Hz to 0.5 Hz) is related to the recombination between the electrons in the TiO$_2$ conduction band and the holes in the HTM at the TiO$_2$/spiro-OMeTAD interface. Using the transmission line model[26], the important elements, such as electron diffusion resistance (R_t), recombination resistance (R_{ct}) and chemical capacitance (C_μ), were derived by fitting the impedance data.
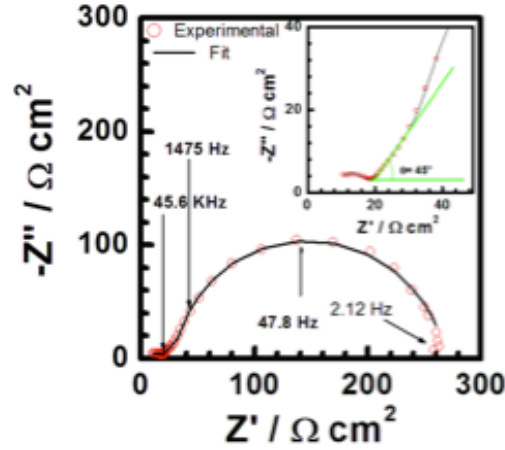
Figure 3.9. Impedance spectra of SSDSC device sensitized with C104 (fresh sample) at forward bias of -0.7 V under illumination conditions (20 mW/cm^2). The solid line corresponds to derived values using the fitting model.
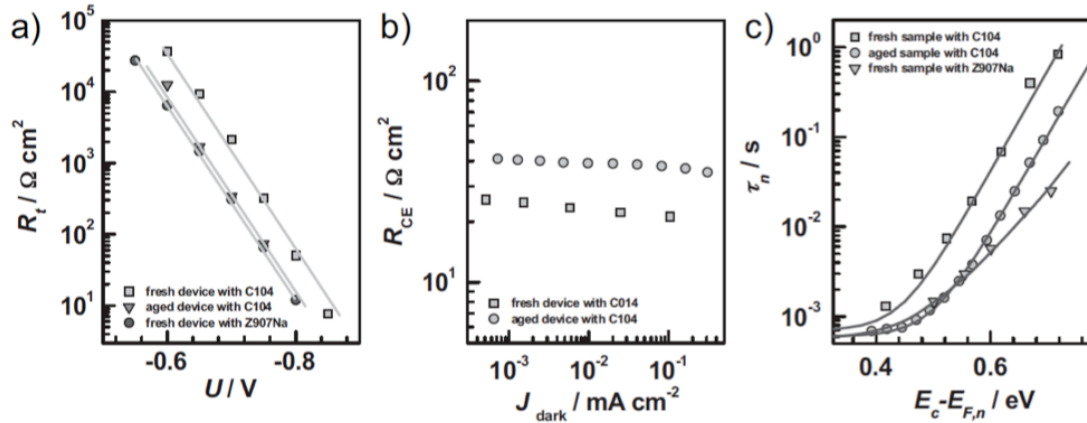

Figure 3.10. Derived equivalent circuit components obtained from impedance measurements in the dark for the fresh device sensitized with C104 dye and its corresponding aged device after 1000 h 1 sun visible light-soaking at 60 °C: (a) Electron diffusion resistance R_t in the TiO$_2$ film (R_t vs. U); (b) Charge transfer resistance R_{CE} at the counter electrode/spiro-OMeTAD interface (R_{CE} vs. dark current); (c) Recombination lifetime (τ_n) for the fresh and aged devices. In order to compare, the R_t and τ_n of similar devices except the sensitizer using Z907Na dye are also presented.

Figure 3.10a illustrates the electron diffusion resistance (R_t) versus applied voltage (U) obtained from impedance measurements in the dark. For comparison, the resistance R_t measured with a similar device using Z907Na is also presented. The steady-state transport resistance reflects the rate of electron displacement in the conduction band of the nanoparticles by means of equation 1[26].

$$R_t = R_0 \exp\left(\frac{E_{cb} - E_{Fn}}{k_B T}\right) = R_0 \exp\left(\frac{E_{cb} - E_{Fp}}{k_B T}\right)\exp\left(\frac{E_{Fp} - E_{Fn}}{k_B T}\right)$$

$$= R_0 \exp\left(\frac{E_{cb} - E_{Fp}}{k_B T}\right)\exp\left(-\frac{U}{k_B T}\right) \tag{1}$$

where R_0 is the film resistance at the applied bias (U) where the electron Fermi level (E_{Fn}) matches the conduction band edge (E_{cb}) and E_{Fp} is the Fermi energy level of the HTM. Thus, any TiO$_2$ conduction band edge movement induced by the light-soaking effect can be inferred by tracing the R_t[23, 26]. As presented in Figure 3.10a, the logarithm of the R_t, which depends on the number of free electrons (n_c) in the conduction band[23, 26], shows parallel behavior for the fresh and aged devices. This implies that the shift of the resistances for the steady-state electron transport is caused by a change in position of the conduction band edge (E_{cb}) with respect to the Fermi level of the HTM. There is a downward shift (to more positive potentials versus NHE) of the TiO$_2$ conduction band edge by approximately 45 mV for the aged device with C104 dye compared to that of the corresponding fresh one. This energy shift influences largely the device's V_{oc} value. The decrease in V_{oc} for the aged device with C104 dye could be mainly related to the surface protonation during the aging period. Compared to the fresh C104 based device, the cell with Z907Na likewise shows a downward shift of the TiO$_2$ conduction band edge (see Figure 3.10a). The displacement of the conduction band edge is about 40 mV for these two devices. The observed increase in charge exchange resistance (R_{CE}) at the Au/spiro-OMeTAD interface was observed upon aging (see Figure 3.10b), indicates that the holes transfer process is slowed down at the Au back contact. The low $F.F.$ found in the aged device stems from its high R_{CE}. The $F.F.$ is a photovoltaic parameter, which in conjunction with V_{oc} and J_{sc} determines the maximum power output from the solar cell.

In order to better understand the electron recombination dynamics at the dye-sensitized heterojunction interface, we have modeled the electron-hole recombination by considering the continuous-time random walk of electron transport in a trap-dominated material. The apparent recombination lifetime τ_n ($\tau_n = R_{ct}C_\mu$) was obtained by fitting the frequency dependent response in impedance measurements. According to the quasi-static treatment[27], the apparent recombination lifetime, τ_n, is related to the conduction band electron lifetime, τ_0, by the expression[26]

$$\tau_n = \tau_0 \left(1 + \frac{\partial n_t}{\partial n_c} \right) \tag{2}$$

where n_t is the trapped electron density, τ_0 is the inverse of the pseudo first order rate constant for the back transfer of electrons from conduction band, and n_c is the conduction band electron density. Our previous impedance studies on DSC show the electrons to be trapped at levels in the band-gap[23, 26]. It is reasonable to assume that these levels are associated with surface states present at the high internal surface area of the TiO$_2$ nanoparticles or with trapping levels at the particle-particle contact. Equation 2 can be expressed by[26]

$$\tau_n = \tau_0 \left[1 + \frac{N_{t,0}}{N_C T_0} \exp\left(\frac{E_{cb} - E_{Fn}}{k_B T} \right)^{\frac{T_0 - T}{T_0}} \right] \tag{3}$$

where $N_{t,0}$ and N_c are the total density of the localized states and the accessible density of states in the conduction band; T is the temperature; T_0 has the unit of temperature and reflects the width of the trap

distribution function below the edge of the conduction band (E_c), a high value of T_0 implying a broad density of state (DOS). The measured apparent recombination lifetime τ_n differ substantially from the free electron lifetime (τ_0) and is dependent on the trap occupational level[25]. Under practical device operating conditions, τ_n is much larger than τ_0. Under these conditions, we assume a first-order rate for recombination of electrons in the nanocrystalline TiO$_2$ with the holes in the HTM, keeping constant in the concentration of holes.

The conduction band electron lifetime τ_0 can be calculated by using equation 3. In order to compare the apparent recombination lifetime τ_n for the fresh and aged device at equal electron concentrations in the titania nanoparticles, the plot in Figure 3.10c uses the difference between the conduction band edge and the Fermi level, i.e., $E_{cb}-E_{Fn}$, as abscissa instead of the applied forward bias voltage (U). Obviously, the apparent recombination lifetime τ_n decreased for the aged device compared with those for the fresh device at an identical energy offset. This is attributed to the generation of additional traps within the TiO$_2$ nanoparticles during the light-soaking test, for example, by lithium ions intercalation, Very similar values of the conduction band electron lifetime time τ_0 (0.7 ms and 0.6 ms) were obtained for the fresh and aged devices, respectively by fitting the apparent recombination lifetime τ_n. The apparent recombination lifetime τ_n in Figure 3.10c were fitted to equation 3 with T_0= 1600 K and 996 K, and $N_{t,0}$= 2.5×10^{19} cm^{-3} and 5.5×10^{19} cm^{-3} for the fresh and aged device, respectively. The larger value of $N_{t,0}$ for the aged device correlates with a shorter apparent recombination lifetime (τ_e) in this device. This result indicates that most of the electron-hole recombination happens between the trapped electrons (by the surface and/or bulk trap states in the band-gap) and the holes in the HTM. We note a higher value of T_0 for the fresh device corresponds to a flatter distribution of trapping states, which were confirmed by the analysis of the intensity dependence of the chemical capacitance determined by the transient photovoltage decay measurement. Compared to the device with Z907Na dye, the device with C104 dye clearly shows a longer electron lifetime, indicating that introduction of the thienothiophene moiety between each hydrophobic alkyl chain and the pyridine ring increases the electron lifetimes[17, 28]. This result likewise identifies that shunting alone was not the cause of the difference in V_{oc} of these devices. The impedance measurement under illumination conditions (20 mW/cm^2) show that the electron diffusion length ($L_e = d\sqrt{R_{ct}/R_t}$, where d is the film thickness) attains 9.1 and 7.1 µm for the fresh and aged devices with C104 dye at -0.5 V bias voltage respectively, which is consistent with a higher J_{sc} obtained in the fresh device. In fact the decreasing of J_{sc} during aging was found to be due to the photodoping of the hole conductor generating colored cation radicals that filter part of incoming light.

Device fabrication of the SSDSCs sensitized with Z907, C101, C104 and C106

Basic 23 nm paste was used for a mesoporous TiO$_2$ film and film thickness was less than 2 µm. TiO$_2$ electrode was stained by immersing it into a dye solution overnight. The concentration of dye

solution was 0.3 mM in a mixture of acetonitrile and *tert*-butyl alcohol solvents (volume ratio: 1/1). Standard spiro-OMeTAD solution was applied for the HTM layer. As a counter electrode, Au was evaporated on top of the HTM layer and Ag was also employed for a high efficiency cell.

3.2.3 CYC-B1 sensitizer and co-adsorbents effect

C104 and CYC-B1 sensitizers have similar molecular structures and the same length of the alkyl chain. CYC-B1 (see Figure 3.1e) possesses a bithiophene unit between each hydrophobic alkyl chain and the pyridine ring. The detailed properties of this dye were reported in reference 29[29]. It also has an immensely high molar extinction coefficient among ruthenium sensitizers due to the extended π-conjugated system of the ancillary ligands. However, the thiophene moiety tends to increase the aggregation of the dyes on the mesoporous TiO_2 surface[30], which leads to unfavorable back electron transfer and decreases the open circuit voltage of the device[30, 31].

CYC-B1 sensitizer

First, we fabricated a device with CYC-B1, but the fill factor was very poor , with a value of less than 0.6. The low fill factor may be from dye aggregation. We investigated the effect of the concentration of the dye solution: the normal concentration (0.3 mM) and 5 times diluted one (0.06 mM) to investigate aggregation of dye on the TiO_2 surface. Figure 3.11 shows UV-Vis spectrum of the TiO_2 films stained with CYC-B1 solution having a normal concentration (0.3 mM) and a diluted concentration (0.06 mM). The absorbance of the film sensitized with diluted concentration slightly decreased compared to that of the film sensitized with normal concentration.
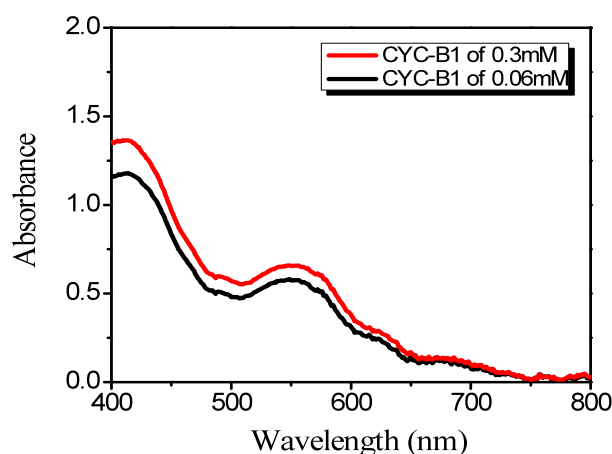

Figure 3.11. UV-Vis spectrum of CYC-B1 of 0.3 mM (red curve) and CYC-B1 of 0.06 mM (black curve) stained on 2 μm thick mesoporous TiO_2 films.

The solar cell performance, measured under simulated AM 1.5G 100 mW/cm^2 illumination is presented in Figure 3.12. The cells with dye solutionS of 0.3 mM and 0.06 mM concentration are denoted as devices A and B, respectively. Device A generated very high J_{sc} around 9 mA/cm^2, but the *F.F.* was less than 0.6, likely due to aggregation of the dye. However, device B had a slightly lower J_{sc} of 8.35 mA/cm^2 and a higher *F.F.* of 0.69 and a V_{oc} of 828 mV. Consequently, it yielded a higher overall efficiency of 4.87 % compared to 4.18 % of device A. This huge improvement of the power conversion efficiency of device B results from an increase of the *F.F.* Although the amount of the CYC-B1 sensitizer on TiO$_2$ surface was decreased, the photocurrent was not significantly reduced. The detailed photovoltaic parameters at 0.1 sun and 1 sun light intensities are summarized in Table 3.3.
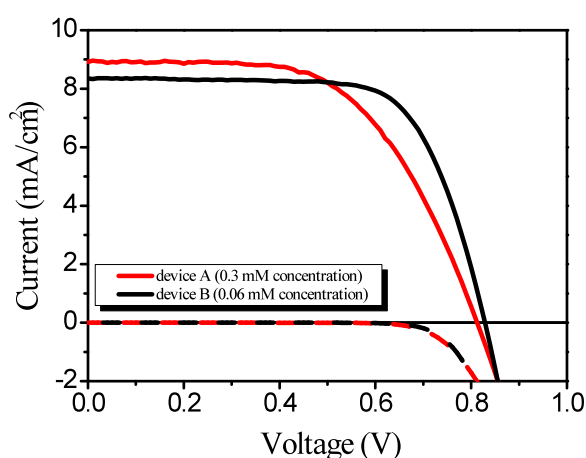

Figure 3.12. *J*-V characteristics of device A (0.3 mM concentration, red curve) and device B (0.06 mM concentration, black curve) under full sunlight (100 mW/cm^2). Dotted lines correspond to the dark current measurement.

device	light intensity	J_{sc} (mA/cm^2)	V_{oc} (mV)	*F.F.*	η (%)
A	0.1 sun	0.69	725	0.74	3.97
	1 sun	8.91	812	0.57	4.18
B	0.1 sun	0.77	745	0.77	4.78
	1 sun	8.35	828	0.69	4.87

Table 3.3. Photovoltaic parameters of device A and B under different light intensities.

Figure 3.13 shows the current dynamics as a function of a light intensity where the dashed lines show the individual photocurrents normalized to 1 sun. Under illumination intensities of 10 mW/cm^2 and 100 mW/cm^2, the device A appears to be unable to sustain linearity in the photocurrent, delivering a J_{sc} from 0.69 to 8.91 mA/cm^2. The J_{sc} is only 77.5 % at 0.1 sun compared to the photocurrent

generated at 1 sun. In contrast, device B exhibits linearity in the photocurrent, and overall efficiencies as well. This nonlinearity of the photocurrent in device A could be attributed to dye aggregation.
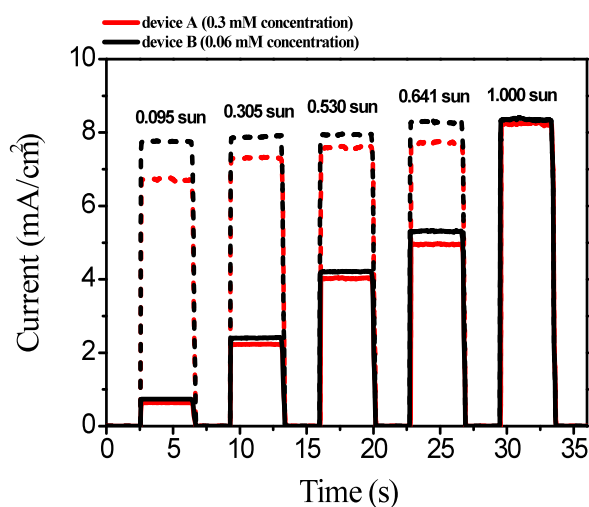

Figure 3.13. Current dynamics of device A (red curve) and B (black curve) at various light intensities. Measured currents (solid line) and normalized currents (1 sun, dashed lines).

Co-adsorbent effect

Co-adsorbents such as chenodeoxycholic acid (CDCA)[31, 32] and 4-guanidinobutyric acid (GBA)[23] are frequently used to prevent aggregation of the dye on the TiO$_2$ surface. The sensitizer could aggregate in a dye solution or on the TiO$_2$ surface. Dye aggregation can be avoided by the presence of co-adsorbents on the TiO$_2$ surface, since co-adsorbents adsorb competitively with dye molecules. They not only reduce dye coverage on the TiO$_2$ surface but also can enhance J_{sc} by improving electron injection yield, and increase V_{oc} by retarding charge recombination, as revealed by increased electron lifetime[33, 34].

For the CYC-B1 sensitizer, GBA and 3-phenylpropionic acid (PPA)[35, 36] co-adsorbents were added to the diluted dye solution to investigate their effect. The molecular structures of the co-adsorbents (GBA and PPA) are illustrated in Figure 3.14. Figure 3.15 shows the UV-Vis spectrum of the TiO$_2$ films stained with diluted CYC-B1 sensitizer and CYC-B1 with co-adsorbent GBA and PPA. The absorbance of the CYC-B1 with PPA was almost the same as compared to that of CYC-B1 alone. However, the absorption peak of the CYC-B1 with GBA sensitized film was decreased considerably compared to that of CYC-B1.
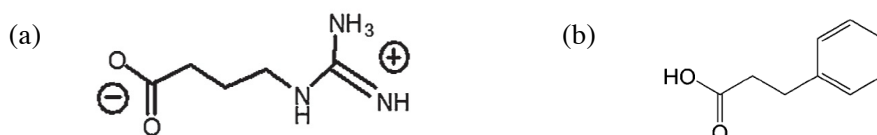

Figure 3.14. Molecular structures of the co-adsorbents: (a) GBA and (b) PPA.
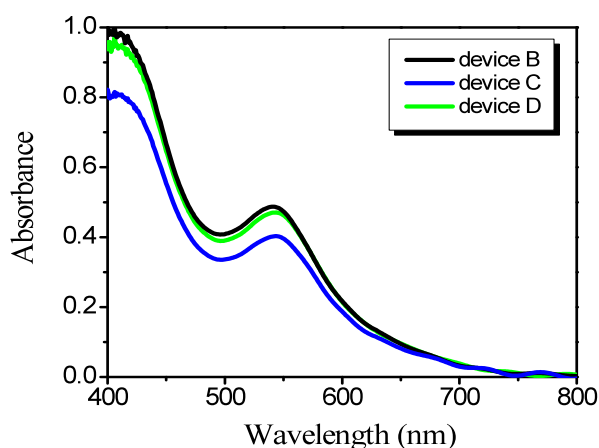
Figure 3.15. UV-Vis spectrum of CYC-B1 of 0.06 mM (black curve), CYC-B1 with PPA (green curve), and CYC-B1 with GBA (blue curve) stained on 2 µm thick mesoporous TiO_2 films.

Devices with and without co-adsorbents were fabricated to explore the photovoltaic performances. The cells prepared by dye solutions containing GBA and PPA were coded as device C and D, respectively. For comparison, a cell sensitized with CYC-B1 alone was also prepared (device B). Figure 3.16a presents the current-voltage characteristics measured at full sunlight (100 mW/cm^2). The devices with co-adsorbents produced a slightly increased V_{oc} of 10 to 17 mV compared to that of device B. Moreover, device D yielded a higher overall efficiency due to improved V_{oc} and F.F. than that of device B. The V_{oc} could be raised due to a decrease of back electron transfer from the TiO_2 electrode to the HTM by dense packing on the electrode of dye and co-adsorbents[37]. Device C generated higher V_{oc}, but J_{sc} was decreased by more than 1 mA/cm^2 compared with devices B and D. A reduction of the photocurrent is assigned to a decreased light harvesting efficiency, since GBA reduced the dye adsorption remarkably. As a result, power conversion efficiency of device C was lower than that of device B. The photocurrent action spectra show the light harvesting efficiencies in Figure 3.16b. The overall IPCE of device C decreased in comparison to those of devices B and D.

device	J_{sc} (mA/cm^2)	V_{oc} (mV)	F.F.	η (%)
B	8.35	828	0.69	4.87
C	7.19	845	0.69	4.25
D	8.31	839	0.70	4.91

Table 3.4. Photovoltaic parameters of devices B, C, and D under full sunlight (100 mW/cm^2).
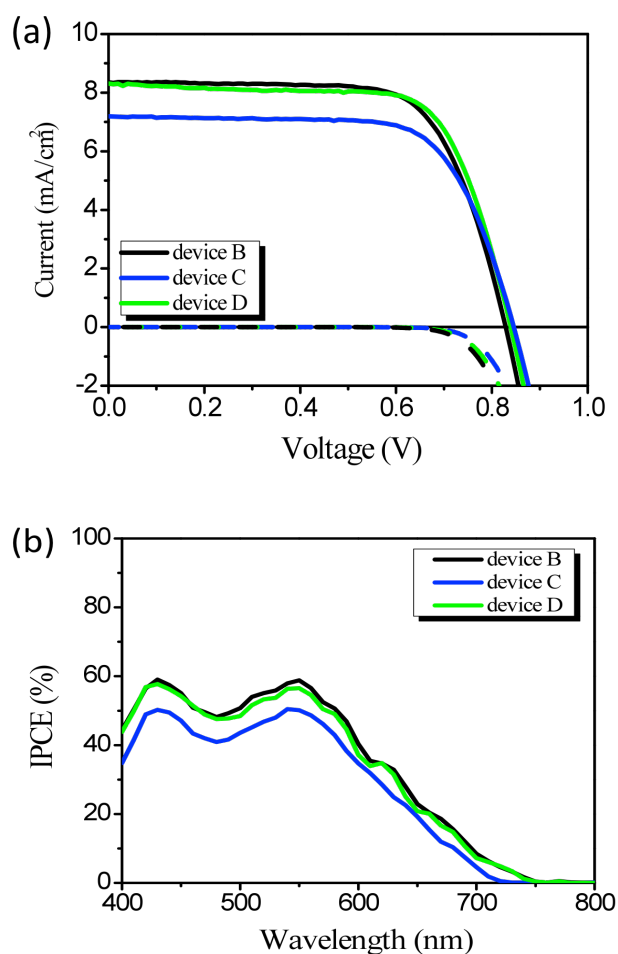
Figure 3.16. (a) *J*-V characteristics of device B (diluted CYC-B1 sensitizer, black curve), device C (with co-adsorbent GBA, blue curve) and device D (with co-adsorbent PPA, green curve) under full sunlight. (100 mW/cm^2) Dotted lines correspond to the dark current measurement. (b) Photocurrent action spectrum of device B (black), C (blue) and D (green).

Next, the effect of the co-adsorbents on electron lifetime was investigated. Figure 3.17 shows electron lifetimes of the devices with and without co-adsorbent GBA as a function of charge density. Device D has almost the same electron lifetime as device B. The cell with GBA has a longer lifetime at fixed charge density than that of the cell without co-adsorbent. Adding GBA resulted in a low photocurrent by decreasing dye loading on the TiO$_2$ surface, but it suppressed charge recombination by passivating the surface's recombination centers, as well as the formation of an insulating layer[23].
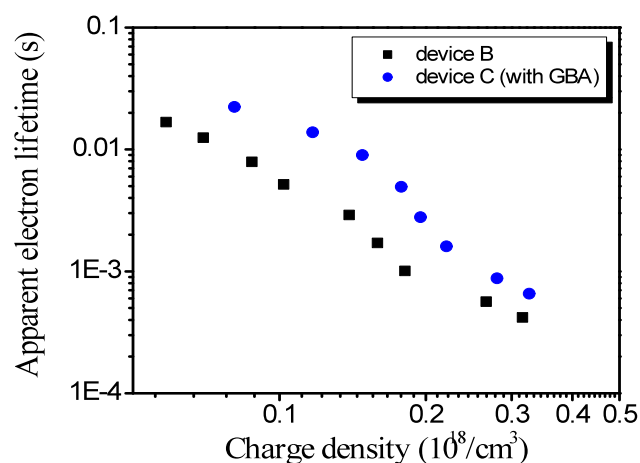
Figure 3.17. Apparent electron lifetime (τ_e) of device B (black dot) and C (blue dot) from transient photocurrent and photovoltage decay measurements.

Device fabrication of the SSDSCs sensitized with CYC-B1 sensitizer

Basic 23 nm paste was used for a mesoporous TiO_2 film and film thickness was less than 2 μm. TiO_2 electrode was stained by immersing it into a dye solution overnight. The normal concentration of dye solution was 0.3 mM and the diluted concentration was 0.06 mM in a mixture of acetonitrile and *tert*-butyl alcohol solvents (volume ratio: 1/1). For the co-adsorption study, 0.06 mM concentration of GBA and PPA were added into the diluted dye solution (0.06 mM concentration). Standard spiro-OMeTAD solution was applied for the HTM layer. As a counter electrode, Au was evaporated on top of the HTM layer.

3. 3 Conclusions

Ruthenium sensitizers having high molar extinction coefficients can generate higher photocurrents with thin TiO_2 films of 2 µm thickness compared to the well known ruthenium dyes such as N719 or Z907. We have demonstrated the photovoltaic properties of a family of high molar extinction coefficient heteroleptic polypyridyl ruthenium sensitizers bearing thiophene units.

We employed ruthenium sensitizers containing hexylthiophene, (hexylthio)thiophene, octylthieno(3,2-b)thiophene and bithiophene groups to solid-state solar cells. These thiophene units increased the conjugation length of the ancillary ligand and resulted in a red-shift of the MLCT transition, as well as enhanced absorption capability. Consequently, they improved the absorbed photon-to-current conversion efficiencies, resulting in high photocurrents.

For the first time, we achieved a certified power conversion efficiency of 5 % with a device sensitized with a C106 sensitizer containing (hexylthio)thiophene unit. Moreover, we successfully demonstrated a stable solid-state solar cell with C104 sensitizer including octylthieno(3,2-b)thiophene under full sunlight at 60 °C for 1000 h. The dyes having thiophene units not only enhanced molar extinction coefficients but also augmented electron lifetimes in the devices.

Bibliography

1.   A. S. Polo, M. K. Itokazu and N. Y. Murakami Iha, Coordination Chemistry Reviews **248** (13-14), 1343-1361 (2004).

2.   A. Hagfeldt, G. Boschloo, L. Sun, L. Kloo and H. Pettersson, Chemical Reviews, **110** (11), 6595-6663 (2010).

3.   K. Hara and H. Arakawa, Handbook of Photovoltaic Science and Engineering, 663-700 (2005).

4.   M. K. Nazeeruddin, A. Kay, I. Rodicio, R. Humphrybaker, E. Muller, P. Liska, N. Vlachopoulos and M. Grätzel, Journal of the American Chemical Society **115** (14), 6382-6390 (1993).

5.   M. K. Nazeeruddin, S. M. Zakeeruddin, R. Humphry-Baker, M. Jirousek, P. Liska, N. Vlachopoulos, V. Shklover, C. H. Fischer and M. Grätzel, Inorganic Chemistry **38** (26), 6298-6305 (1999).

6.   M. K. Nazeeruddin, P. Péchy, T. Renouard, S. M. Zakeeruddin, R. Humphry-Baker, P. Comte, P. Liska, L. Cevey, E. Costa, V. Shklover, L. Spiccia, G. B. Deacon, C. A. Bignozzi and M. Grätzel, J. Am. Chem. Soc. **123** (8), 1613-1624 (2001).

7.   Y. Chiba, A. Islam, Y. Watanabe, R. Komiya, N. Koide and L. Y. Han, Jpn. J. Appl. Phys., 2 **45** (24-28), L638-L640 (2006).

8.   S. M. Zakeeruddin, M. K. Nazeeruddin, R. Humphry-Baker, P. Péchy, P. Quagliotto, C. Barolo, G. Viscardi and M. Grätzel, Langmuir **18** (3), 952-954 (2002).

9.   M. K. Nazeeruddin, S. M. Zakeeruddin, J. J. Lagref, P. Liska, P. Comte, C. Barolo, G. Viscardi, K. Schenk and M. Grätzel, Coordination Chemistry Reviews **248** (13-14), 1317-1328 (2004).

10.   P. Wang, S. M. Zakeeruddin, J. E. Moser, M. K. Nazeeruddin, T. Sekiguchi and M. Grätzel, Nat Mater **2** (6), 402-407 (2003).

11.   P. Wang, S. Zakeeruddin, R. Humphry-Baker, J. Moser and M. Grätzel, Adv Mater **15** (24), 2101-2104 (2003).

12.   J. E. Kroeze, N. Hirata, S. Koops, M. K. Nazeeruddin, L. Schmidt-Mende, M. Grätzel and J. R. Durrant, J Am Chem Soc **128** (50), 16376-16383 (2006).

13.   S. Altobello, C. A. Bignozzi, S. Caramori, G. Larramona, S. Quici, G. Marzanni and R. Lakhmiri, Journal of Photochemistry and Photobiology A: Chemistry **166** (1-3), 91-98 (2004).

14.   E. Galoppini, Coordination Chemistry Reviews **248** (13-14), 1283-1297 (2004).

15.   M. K. Nazeeruddin, Q. Wang, L. Cevey, V. Aranyos, P. Liska, E. Figgemeier, C. Klein, N. Hirata, S. Koops, S. A. Haque, J. R. Durrant, A. Hagfeldt, A. B. P. Lever and M. Grätzel, Inorganic Chemistry **45** (2), 787-797 (2005).

16.   M. K. Nazeeruddin, T. Bessho, L. Cevey, S. Ito, C. Klein, F. De Angelis, S. Fantacci, P. Comte, P. Liska, H. Imai and M. Grätzel, Journal of Photochemistry and Photobiology A: Chemistry **185** (2-3), 331-337 (2007).

17.   F. Gao, Y. Wang, D. Shi, J. Zhang, M. Wang, X. Jing, R. Humphry-Baker, P. Wang, S. M. Zakeeruddin and M. Grätzel, J Am Chem Soc **130** (32), 10720-10728 (2008).

18.   F. Gao, Y. Wang, J. Zhang, D. Shi, M. Wang, R. Humphry-Baker, P. Wang, S. M. Zakeeruddin and M. Grätzel, Chemical Communications (23), 2635-2637 (2008).

19.   Y. Cao, Y. Bai, Q. Yu, Y. Cheng, S. Liu, D. Shi, F. Gao and P. Wang, The Journal of Physical Chemistry C **113** (15), 6290-6297 (2009).

20.   L. Schmidt-Mende and M. Grätzel, Thin Solid Films **500** (1-2), 296-301 (2006).

21.   Z.-S. Wang, N. Koumura, Y. Cui, M. Takahashi, H. Sekiguchi, A. Mori, T. Kubo, A. Furube and K. Hara, Chemistry of Materials **20** (12), 3993-4003 (2008).

22.   S. J. Moon, J. H. Yum, R. Humphry-Baker, K. M. Karlsson, D. P. Hagberg, T. Marinado, A. Hagfeldt, L. C. Sun, M. Grätzel and M. K. Nazeeruddin, J Phys Chem C **113** (38), 16816-16820 (2009).

23.   M. Wang, C. Grätzel, S. J. Moon, R. Humphry-Baker, N. Rossier-Iten, S. M. Zakeeruddin and M. Grätzel, Adv Funct Mater **19** (13), 2163-2172 (2009).

24.   M. Wang, X. Li, H. Lin, P. Pechy, S. M. Zakeeruddin and M. Grätzel, Dalton Transactions (45), 10015-10020 (2009).

25.   J. Bisquert and V. S. Vikhrenko, The Journal of Physical Chemistry B **108** (7), 2313-2322 (2004).

26.   M. Wang, P. Chen, R. Humphry-Baker, S. M. Zakeeruddin and M. Grätzel, ChemPhysChem **10** (1), 290-299 (2009).

27. J. Bisquert, A. Zaban, M. Greenshtein and I. Mora-Sero, J Am Chem Soc **126** (41), 13550-13559 (2004).

28. L. Schmidt-Mende, J. E. Kroeze, J. R. Durrant, M. K. Nazeeruddin and M. Grätzel, Nano Lett **5** (7), 1315-1320 (2005).

29. C. Y. Chen, S. J. Wu, C. G. Wu, J. G. Chen and K. C. Ho, Angewandte Chemie International Edition **45** (35), 5822-5825 (2006).

30. G. Li, K.-J. Jiang, Y.-F. Li, S.-L. Li and L.-M. Yang, The Journal of Physical Chemistry C **112** (30), 11591-11599 (2008).

31. J. H. Yum and et al., Nanotechnology **19** (42), 424005 (2008).

32. J.-H. Yum, S.-r. Jang, R. Humphry-Baker, M. Grätzel, J.-J. Cid, T. Torres and M. K. Nazeeruddin, Langmuir **24** (10), 5636-5640 (2008).

33. K. Hara, Y. Dan-oh, C. Kasada, Y. Ohga, A. Shinpo, S. Suga, K. Sayama and H. Arakawa, Langmuir **20** (10), 4205-4210 (2004).

34. Z.-S. Wang, Y. Cui, Y. Dan-oh, C. Kasada, A. Shinpo and K. Hara, The Journal of Physical Chemistry C **111** (19), 7224-7230 (2007).

35. P. Wang, S. M. Zakeeruddin, R. Humphry-Baker and M. Grätzel, Chemistry of Materials **16** (14), 2694-2696 (2004).

36. D. Kuang, C. Klein, Z. Zhang, S. Ito, J. E. Moser, S. Zakeeruddin and M. Grätzel, Small **3** (12), 2094-2102 (2007).

37. P. Zuo, C. Li, Y.-S. Wu, X.-C. Ai, X.-S. Wang, B.-W. Zhang and J.-P. Zhang, Journal of Photochemistry and Photobiology A: Chemistry **183** (1-2), 138-145 (2006).

Chapter 4

High Molar Extinction Coefficient Sensitizers – Organic Dyes

4. 1 Introduction

Metal-free organic dyes have three major advantages over Ru-based sensitizers: (1) The molar extinction coefficients of organic dyes are usually higher than those of metal complexes, making them attractive for thin film and solid-state DSCs. (2) No precious metal such as ruthenium is contained in organic dyes. This reduces the overall cost of device production. (3) The molecular structures of organic dyes are diverse in form and can be easily designed, tuned and synthesized compared to the Ru-based sensitizer. For these reasons, organic dyes are attractive alternatives to conventional Ru-based sensitizers in DSCs[1].

Most organic dyes possess a donor-π-bridge-acceptor (D-π-A) structure (see Figure 4.1), which is easy to design for extending the absorption spectra, adjusting HOMO and LUMO levels to complete the intramolecular charge separation. Coumarin, indoline, and triarylamine moieties, which are electron-rich arylamines, are representatively employed to the donor groups. The best moieties for the π-bridge typically contain thiophene units, such as oligothiophene, thienothiophene, ethylenedioxythiophene (EDOT), due to their excellent charge separation properties. For the acceptor group, a cyanonacrylic acid containing carboxylic acid is most often used and it plays a role as an anchoring group[2].
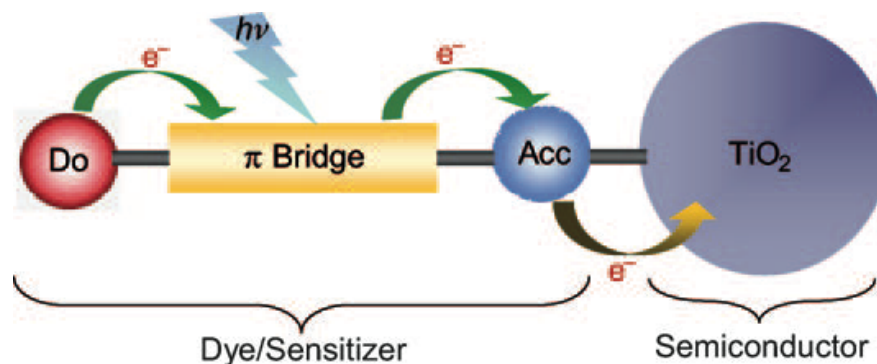
Figure 4.1. Scheme of D-π-A organic dyes[2].

Among the diverse number of donor groups, a large number of triarylamine dyes have been designed and most of them have shown good power conversion efficiencies in DSCs because of their prominent electron donating ability and hole-transport properties. To improve dye performance, researchers have designed different groups. For example, substituted triarylamine donor groups such as dimethylfluorenylamino electron donor[3], dendronized triarylamine[4] and methoxy triphenylamnine[5] have been employed. The tailored triarylamine electron donor can increase electron density of the donor moiety as well as enhance stability of DSCs. Another way to increase efficiency in the D-π-A structure is by expanding the π-conjugation of the bridge between the donor and acceptor by introducing more conjugation units such as thienothiophene[6], bithiophene[3], EDOT[7] and carbon-carbon double bonds. It leads to increase molar extinction coefficient and a bathochromic shift in the absorption spectra.

The high molar extinction coefficients, exhibited by D-π-A dyes, are especially desirable for thin TiO$_2$ films in SSDSCs. For instance, indoline dye D102[8], it has very high extinction coefficient of 55,800 M^{-1}cm^{-1} at 491 nm, which yields over 90 % absorption over a broad spectral range when sensitizing TiO$_2$ films are as thin as 1.4 μm. However, for the ruthenium sensitizers, the TiO$_2$ film of 10 μm thickness is required to get the same absorption. Therefore, sensitizers with high extinction coefficient are essential to enhance photovoltaic performance of the SSDSC device.

Although organic dyes have many advantages as sensitizers in DSCs, the efficiency of devices prepared with them has been limited mainly by two factors: First, increasing the size of the conjugated system chain in organic dyes can cause dye aggregation or π-π stacking on the TiO$_2$ surface due to their planar structures. Dye aggregation results in unfavorable back electron transfer and decreasing cell performance in a DSC. Second, sensitizers reported so far to give high efficiencies mostly have absorption bands below 550nm, indicating that photons in the longer wavelength region are not absorbed efficiently. They should, however, harvest incident light in a broad spectral range to obtain high photocurrent. Some organic dyes show panchromatic response, but the obtained photocurrent and efficiency are not as high as expected due to their low LUMOs, which reduces injection efficiency. New highly absorbing near infrared dyes need to be designed to improve device performance.

In this chapter, new organic dyes having high molar extinction coefficient will be employed in the solid-state DSCs. The sensitizers investigated are divided into three parts: modified triarylamine donors, extended π-conjugation bridges and near infrared dyes.

4. 2 Organic Dyes Having High Molar Extinction Coefficients

4.2.1 Alkoxy substituted triarylamine dyes

Sun and co-workers reported sensitizers modified triphenylamine (TPA) donor by adding methoxy moiety (coded as D9, see Appendix A1)[5]. The introduction of a methoxy moiety in the TPA donor leads to extend absorption region in the visible light, compared to a dye without a methoxy unit.

Through further optimizing molecular structures, they synthesized sensitizers having different alkoxy substituents on the TPA donor and a bisthiophene π-bridge (coded as D5L6, D21L6, and D25L6, see Figure 4.2). The synthetic routes of these dyes were described in reference 9 and 10[9, 10].

D5L6:   R = H
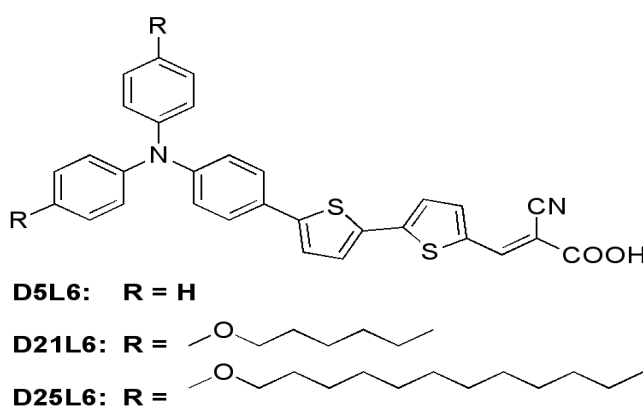
D21L6: R =

D25L6: R =

Figure 4.2. Molecular structures of D5L6, D21L6 and D25L6.

code	IUPAC name
D5L6	3-(5-(5-(4-(diphenylamino)phenyl)thiophene-2-yl)thiophene-2-yl)-2-cyanoacrylic acid
D21L6	3-(5-(5-(4-(bis(4-(hexyloxy)phenyl)thiophene-2-yl)thiophene-2-yl)-2-cyanoacrylic acid
D25L6	3-(5-(5-(4-(bis(4-(dodecyloxy)phenyl)thiophene-2-yl)thiophene2-yl)-2-cyanoacrylic acid

Table 4.1. IUPAC names of D5L6, D21L6 and D25L6.

To characterize sensitizers, the cyclic voltammogram were measured in acetonitrile containing 0.1 M tetrabutylammonium tetrafluoroborate (TBA(BF$_4$)) with 0.1 V/s scan rate in Table 4.1. The D5L6 shows a reversible couple at 1.13 V vs. NHE due to oxidation of the triphenylamine moiety. We note that the D21L6 and D25L6 oxidation potential (0.98 and 0.96 V vs. NHE) shifted cathodically when compared to the D5L6, which demonstrates the extent of destabilization of HOMO caused by the alkoxy groups. The excited state oxidation potential of the dye plays an important role in the electron

injection process from dye to TiO_2. Neglecting any entropy change during light absorption, the value can be derived from the ground state oxidation couple and the zeroth-zeroth excitation energy $E_{(0-0)}$ derived from equation: $E_{(S+/S*)} = E_{(S+/S)} - E_{(0-0)}$. From the absorption/emission spectra, $E_{(0-0)}$ energies of 2.40, 2.33 and 2.31 eV were extracted for D5L6, D21L6, and D25L6, respectively. The excited state oxidation potentials of these dyes are higher than -1.27 V vs. NHE, which are notably more negative than the TiO_2 conduction band potential[11]. The first oxidation potential of spiro-OMeTAD is 0.81 V vs, NHE which is more positive than I^-/I_3^- redox couple (≈ 0.4 V vs. NHE)[12, 13]. The oxidation potentials of the dyes are positive enough to drive the dye regeneration process to compete efficiently with recapture of the injected electrons by the dye cation radical.

These organic dyes show around 3 times higher molar extinction coefficient (see Table 4.2 and Figure 4.3a) than the ruthenium dyes (Z907, ε=12,200 $M^{-1}cm^{-1}$), which is an important issue for solid-state devices, where the film thickness is usually very thin (~2 μm) in order to obtain a good pore filling. Figure 4.3b shows that the absorption spectra of the dyes adsorbed onto 3 μm thick TiO_2 electrodes are similar to those of the corresponding solution spectra but exhibit a red-shift due to the interaction of the anchoring groups with the surface titanium ions and scattering effect of light in mesoporous TiO_2.

code	abs max[a] [nm]	emission max[a] [nm]	extinction coefficients [$M^{-1}cm^{-1}$]	$E_{(S+/S)}$[b] [V]	$E_{(0-0)}$[c] [eV]	$E_{(S+/S*)}$[d] [V]
D5L6	438	611	34,000	1.13	2.40	-1.27
D21L6	458	623	37,000	0.98	2.33	-1.35
D25L6	460	626	36,000	0.96	2.31	-1.35

a: Absorption and emission spectra were measured in ethanol at 25 °C. **b**: The oxidation potential of the dyes measured under the following conditions: working electrode, glassy carbon; electrolyte, 0.1 M tetrabutylammonium tetrafluoroborate, $TBA(BF_4)$ in acetonitrile; scan rate, 0.1 V/s. Potentials measured vs Fc^+/Fc were converted to NHE by addition of +0.69 V. **c:** The zero-zero excitation energies, $E_{(0-0)}$ are estimated from the intercept of the normalized absorption and emission spectra. **d:** The excited state oxidation potentials were derived from equation: $E_{(S+/S*)} = E_{(S+/S)} - E_{(0-0)}$

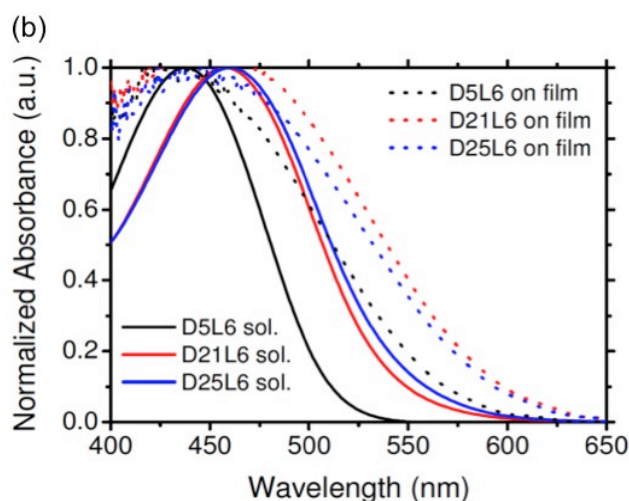Table 4.2. Absorption/Emission spectra data and electrochemical properties of D5L6, D21L6 and D25L6.
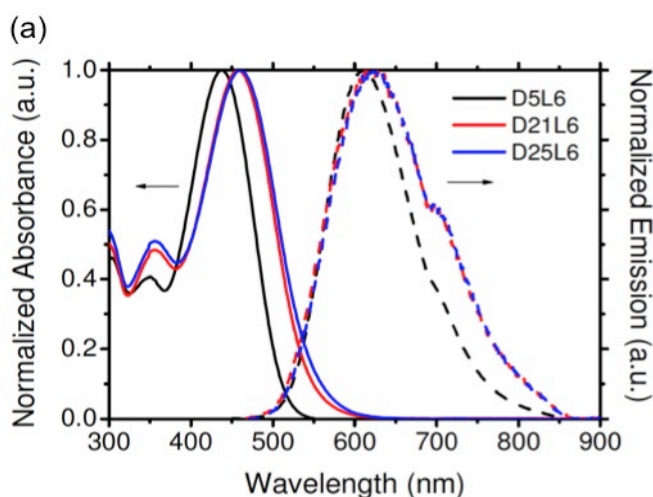
Figure 4.3. (a) Normalized absorption (solid line)/emission (dashed line) spectra and (b) absorption spectra on 3 μm thick TiO2 electrodes (dotted line) of D5L6 (black), D21L6 (red), and D25L6 (blue).

Figure 4.4a shows the incident monochromatic photon-to-current conversion efficiency (IPCE) of SSDSCs incorporating D5L6, D21L6 and D25L6 organic dyes. The IPCE spectra of D21L6 and D25L6 that contain long alkoxy chains exhibit 30 nm red-shift, which is consistent with solution absorption spectra. The red-shift contributes to enhanced current collection of D21L6 and D25L6 when compared with D5L6. The IPCE data of D21L6 plotted as a function of excitation wavelength shows the highest value, 54 % at 460 nm where as the D5L6 and D25L6 showed a slightly lower IPCE 51 %. Figure 4.4b shows the current-voltage characteristics for solid-state solar cells prepared with different dyes. Under standard global AM 1.5 solar conditions, the D21L6 sensitized cell showed the highest J_{sc} of 9.64 mA/cm^2, V_{oc} of 798 mV and $F.F.$ of 0.57, corresponding to an overall efficiency η of 4.44 % (active area of 0.185 cm^2) (see Table 4.3). Under lower light intensities, 0.1 and 0.5 sun, the overall efficiencies of a DSC were higher than that of a DSC measured under 1 sun due to ohmic losses and faster recombination due to higher charge density, leading to a decrease in fill factor. However, J_{sc} obtained under lower intensities are relatively lower when normalized to 1 Sun than J_{sc} measured under 1 sun condition.
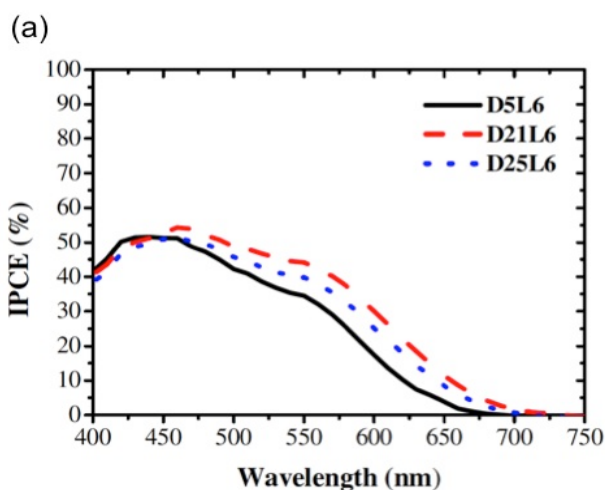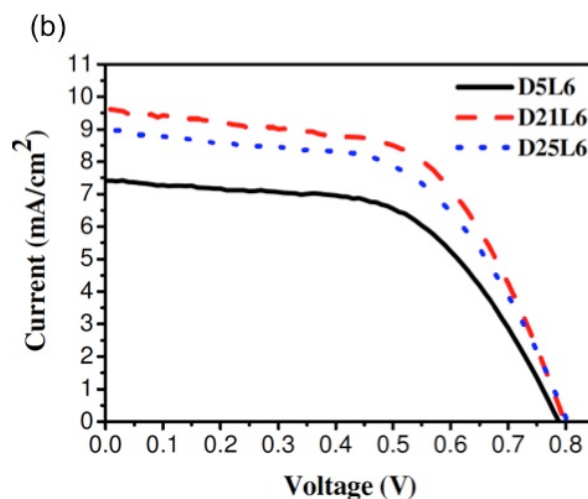
Figure 4.4. Photocurrent action spectrum (a), and *J*-V characteristics (b) of SSDSCs with D5L6 (black solid line), D21L6 (red dashed line) and D25L6 (blue dotted line) sensitizers, measured under full sunlight (100 mW/cm^2).

device	light intensity	J_{sc} (mA/cm^2)	V_{oc} (mV)	*F.F.*	η (%)
D5L6[a]	0.1 sun	0.65	719	0.78	3.89
	0.5 sun	3.88	766	0.65	3.81
	1 sun	7.41	788	0.57	3.35
D21L6[b]	0.1 sun	0.78	740	0.73	4.51
	0.5 sun	4.83	791	0.62	4.64
	1 sun	9.64	798	0.57	4.44
D25L6[a]	0.1 sun	0.77	733	0.76	4.59
	0.5 sun	4.62	787	0.64	4.58
	1 sun	9.01	803	0.56	4.04

Table 4.3. Photovoltaic parameters of SSDSCs prepared with D5L6, D21L6 and D25L6 under various light intensities. a: active area of 0.2 cm^2, b: active area of 0.185 cm^2

Figure 4.5 shows the current dynamics as a function of light intensity, which show the individual photocurrents normalized to 1 sun J_{sc}. These currents are showing super-linearity without achieving a plateau. At the low light intensities such as 0.019 and 0.095 sun, the normalized J_{sc} are only 66 and 79% of the J_{sc} at 1 sun. The light intensity for the IPCE measurement is measured at about these lower intensities and the low IPCEs when compared to the white light J_{sc} are ascribed to this super-linearity of J_{sc} as function of light intensity. The IPCEs are integrated from 350 to 750 nm are 6.1, 7.6 and 6.9 mA/cm^2 which are lower than the J_{sc} obtained from the *J*-V characteristics. The lower observed photocurrent under low intensity could be attributed to aggregation of organic dyes on the TiO$_2$ surface. The higher efficiency of the D21L6 and D25L6 compared to the D5L6 demonstrate the beneficial influence of alkoxy units that enhanced light harvesting resulting in a higher photocurrent.

D25L6 showed a small decrease in photocurrent when compared to D21L6 although optical and electrochemical properties are similar.

Figure 4.6 shows that the relationship between electron lifetimes of solid-state cells of D21L6, and D25L6. As mentioned above, the electron lifetime decreases with increasing charge (electron) density, which means the recombination rate (the reciprocal electron lifetime) becomes faster. For a fixed charge (electron) density, D21L6 shows a longer electron lifetime than that of D25L6, leading to a slightly lower performance of the D25L6 solid-state solar cell. The red-shift in IPCE is attributed to incorporating alkoxy group in the D21L6 and D25L6. However, the long alkoxy chain in D25L6 does not give a further increase in photocurrent because of similar absorption behavior and the fast electron recombination compared to D21L6. The reason for the shorter electron lifetime in D25L6 cell is not clear, but probably caused by issues with spiro-OMeTAD due to the long chain. Because D25L6 showed exactly the same electron lifetime as lifetime of D21L6 in liquid electrolyte-based DSCs.
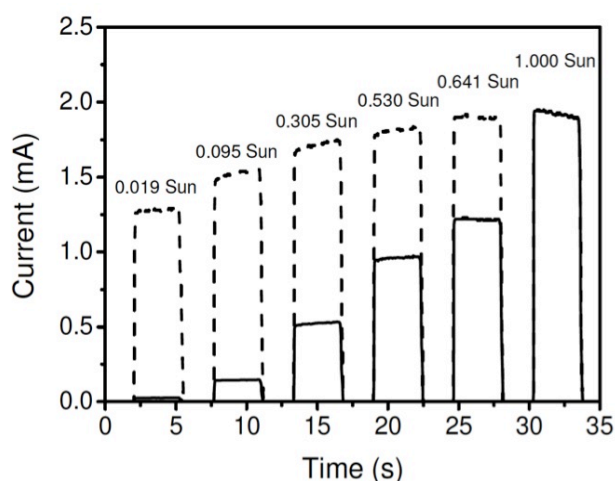

Figure 4.5. The current dynamics of SSDSCs sensitiyed with D21L6 as various light intensities: measured currents (solid line) and normalized currents (1 sun, dashed line).
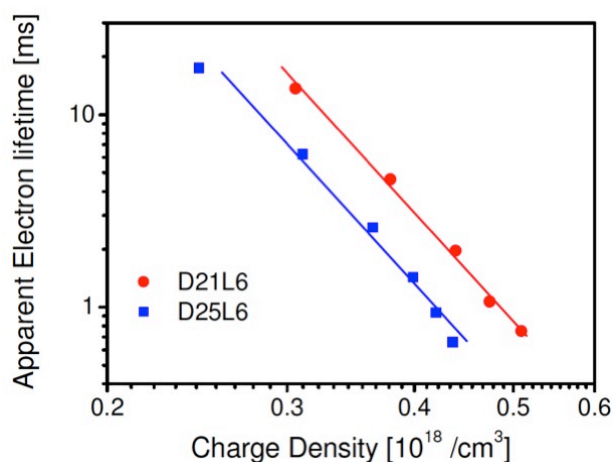

Figure 4.6. The apparent electron lifetime of SSDSCs with D21L6 (red circle) and D25L6 (blue square) sensitizers.

In order to probe the photogenerated charge carriers, photo-induced absorption (PIA) spectroscopy was performed on thin TiO_2 films stained by dye with and without spiro-OMeTAD. Figure 4.7a shows the in-phase signal of the PIA spectrum of 2.5 μm thick TiO_2 film stained by D25L6 on a glass substrate. The appearance of a new transient species is apparent due to a decreased transmission signal. The ΔT/T signal is configured to display as a positive signal in Figure 4.7a. So the positive signal at 740 nm and 1300 nm indicates a strong absorption signal. To confirm the nature of the signal, the dye was chemically oxidized with a strong oxidizing agent, nitrosonium tetrafluoroborate ($NOBF_4$). The oxidized spectrum of D25L6 in chlorobenzene is shown for comparison in Fig 4.7a. The $ΔA_{sol}$ (O.D of oxidized dye – O.D of dye) is consistent with measured PIA spectrum. At wavelengths longer than 1080 nm, the measured PIA shows a higher signal when compared to the oxidized spectrum. This was ascribed to the weak absorption of photo-induced electrons in the TiO_2 film and a shift in the spectrum due to the different medium. In Figure 4.7b, we compare PIA of dye coated TiO_2 film with and without spiro-OMeTAD. The spectrum in the absence of the spiro-OMeTAD shows the characteristic spectrum of the oxidized dye. When the dyed sample is infiltrated with the spiro-OMeTAD, changes in the PIA spectrum are observed. The absorption of the oxidized dye disappeared in the presence of spiro-OMeTAD as a result of hole-transfer from the oxidized dye to the spiro-OMeTAD. The signal at 740 nm is replaced by a small peak around 700 nm is consistent with the oxidized spiro-OMeTAD. In addition the IR peak due to the localization of the hole on the triaryl amine functionality of the spiro-OMeTAD shifts further to the red. This is unfortunately obscured to some extent due to the similar functionality in this series of dyes that localizes the positive charge. But a more sophisticated mathematical treatment of the data involving analysis of the total spectra confirms the similar observations that have been reported[13-15]. Cappel *et al.* found the red-shifted peak of oxidized spiro-OMeTAD, especially in presence of dye and deduced it could be additionally affected by a localized electric field due to electrons in TiO_2[13]. Hence, an efficient hole-transfer from sensitizer to spiro-OMeTAD is deduced by PIA spectroscopy. D5L6 and D21L6 (data is not shown here) showed very similar signal with and without spiro-OMeTAD to D25L6 and here, we observe an efficient hole-transfer process between organic dyes and spiro-OMeTAD.
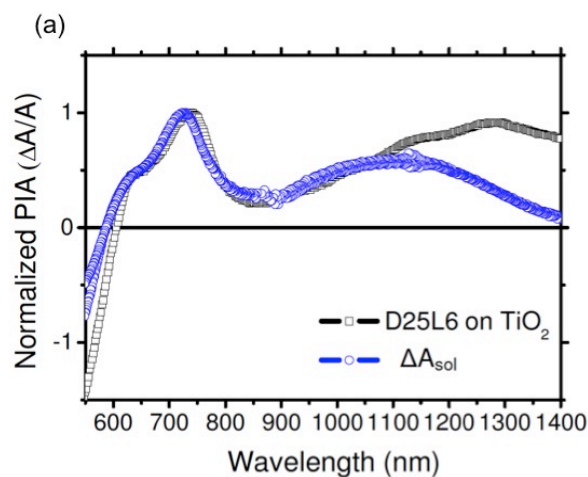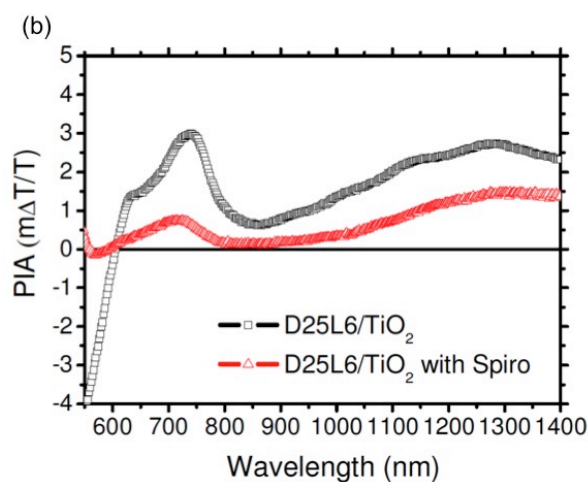
Figure 4.7. (a) Comparison of measured normalized photo-induced absorption spectrum of dyed TiO2 film with normalized difference of optical density after dye oxidation: $\Delta A sol = O.D_{oxidized\ dye} - O.D_{dye}$. (b) Photo-induced absorption spectra of 2.5 μm TiO2 film stained by D25L6 with (red triangle) and without (black square) spiro-OMeTAD.

Device fabrication of the SSDSCs sensitized with DL sensitizers

A mesoporous TiO$_2$ layer (~1.7 μm thick) was coated by the doctor-blading technique with an Acidic 20 nm paste. TiO$_2$ electrodes were stained by immersing them into dye solutions for 3 hours. The normal concentration of dye solution was 0.3 mM in ethanol. Standard spiro-OMeTAD solution was applied for a HTM layer. As a counter electrode, Au was evaporated on top of the HTM layer.

4.2.2 Changing different π-bridges in triphenylamine dyes

The previously-investigated dye coded D21L6 has a 2,2′-dithiophene (**DT**) unit as a linker part between the electron donor and acceptor. Below new organic sensitizers (coded as C2, C6, and C12) are the D21L6 analogue but they have dialkyl-cyclopenta[2,1-*b*:3,4-*b*′]dithiophene (**CPDT**) segments instead of dithiophene unit in D21L6 (see Figure 4.8). The molar extinction coefficients of new sensitizers featuring CPDT segments were enhanced remarkably compared to the D21L6 sensitizer (33,8000 M^{-1} cm^{-1} at 525 nm)(see Table 4.4). To investigate effect of alkyl chain lengths, 3 different alkyl chains (ethyl, hexyl and dodecyl) were employed to the CPDT unit.
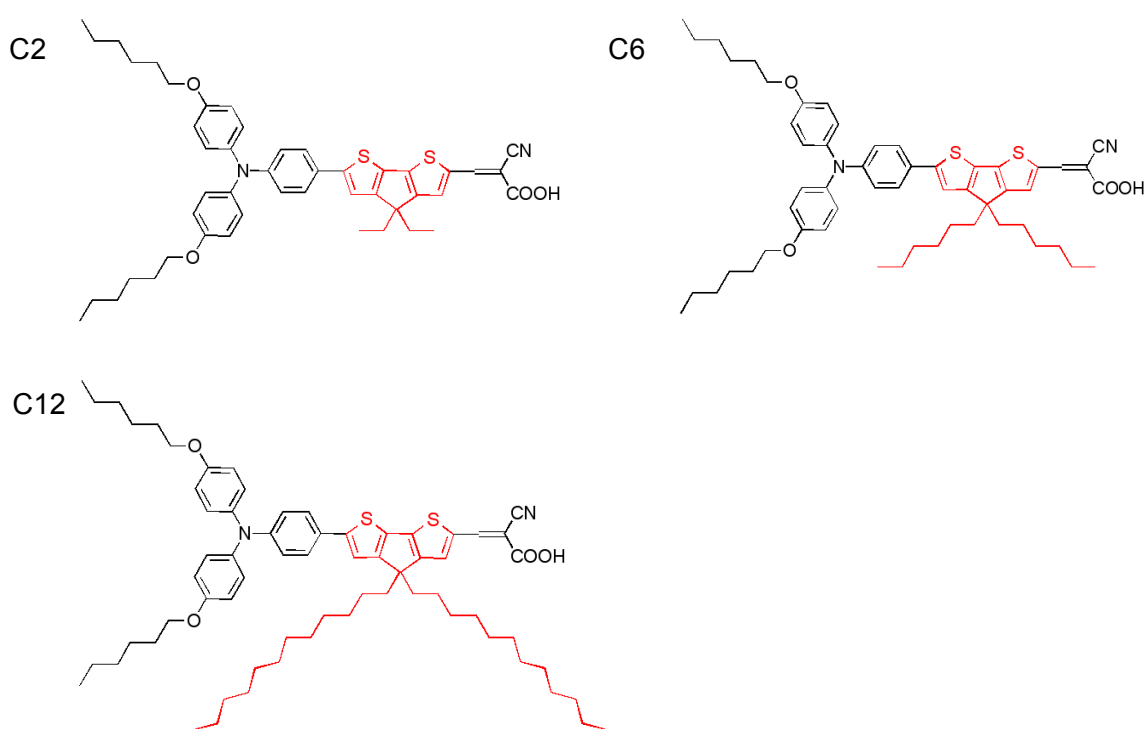

Figure 4.8. Molecular structures of C2, C6 and C12.

code	IUPAC name	molar extinction coefficient ($M^{-1}cm^{-1}$)
C2	2-cyano-3-{6-{4-[*N,N*-bis(4-hexyloxyphenyl)amino]phenyl}-4,4-diethyl-4*H*-cyclopenta[2,1-*b*:3,4-*b*']dithiophene-2-yl}acrylic acid	50,000 at 548 nm
C6	2-cyano-3-{6-{4-[*N,N*-bis(4-hexyloxyphenyl)amino]phenyl}-4,4-dihexyl-4*H*-cyclopenta[2,1-*b*:3,4-*b*']dithiophene-2-yl}acrylic acid	62,700 at 555 nm
C12	2-cyano-3-{6-{4-[*N,N*-bis(4-hexyloxyphenyl)amino]phenyl}-4,4-didodecyl-4*H*-cyclopenta[2,1-*b*:3,4-*b*']dithiophene-2-yl}acrylic acid	55,000 at 525 nm

Table 4.4. IUPAC names and molar extinction coefficients of C2, C6 and C12.

Figure 4.9 depicts UV-Vis absorption spectra of TiO_2 films stained by C2, C6 and C12 dyes. The C2 dye, which has the shortest alkyl chain (ethyl) shows the highest absorption value and the C12 dye, which has the longest alkyl chain shows the lowest absorption capability. Even though the molar extinction coefficient of the C2 dye is not higher than C12, the high absorption value of C2 could be from the aggregation of the dye on the TiO_2 surface due to its short alkyl chain.
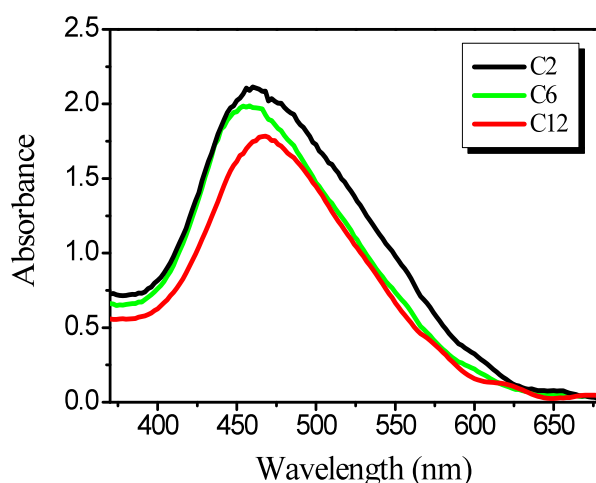

Figure 4.9. UV-Vis spectrum of C2 (black), C6 (green) and C12 (red) stained on 2 μm thick mesoporous TiO_2 films.

For sensitization of the TiO_2 films with C dyes, mesoporous TiO_2 electrodes were immersed into dye solutions for 2 h. However, we reduced the immersing time for the C2 sensitizer from 2 h to 45 min, because the device (C2-2h sensitized cell) prepared with a TiO_2 electrode that was dipped for 2 h in a C2 solution showed a very poor photovoltaic performance under full sunlight (see Figure 4.10). The photovoltaic performance of the C2-2h sensitized cell measured under 0.1 sun looked promising due to the extremely high photocurrent of 1.23 mA/cm^2 and high overall efficiency of 5.96 %. However, under full sunlight the cell appeared to be incapable of sustaining linearity in the photocurrent, delivering a J_{sc} of only 7.07 mA/cm^2, with η being only 2.14 %. In addition, the cell had very low $F.F.$ of 0.39 under full sunlight. This poor performance of the cell could be from the aggregation of dye molecules on the TiO_2 surface. The size of C2 dye molecule is relatively small compared to C6 and C12 dye. To avoid aggregation, we dipped electrodes for only 45 min into the C2 dye solution for coloration (C2-45min sensitized cell). Under simulated AM 1.5G sunlight the C2-45min sensitized device produced high J_{sc} of over 11.0 mA/cm^2, but the $F.F.$ was as low as ever at 0.54. The linearity of J_{sc} with respect to illumination intensity improves compared to that of the C2-2h sensitized cell, however photocurrents measured under 0.1 and 1 sun were still non-linear (see Table 4.5).

Interestingly, when the cell was stored in the dark for 1 month, the cell performance was improved from 5.11 % to 5.80 % under full sunlight. The photocurrent of the aged cell decreased but the open circuit voltage (902 mV) and fill factor (0.68) increased significantly, leading to an improved overall efficiency of 5.80 % (see Figure 4.10 and Table 4.5). This improvement can be explained by extra dye molecules, which were weakly bound to the TiO_2 surface, detaching from the surface[16]. Huge improvement of V_{oc} of the aged cell might also be from an effect of water[17]. Water can increase V_{oc} temporarily but it should be removed from a device for long-term stability.
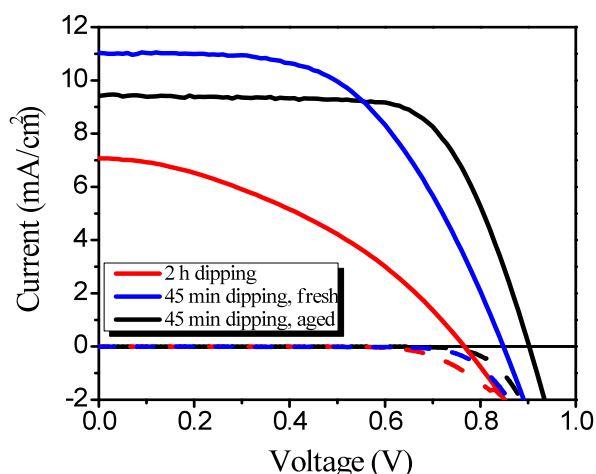

Figure 4.10. *J*-V characteristics of the devices with C2 sensitizer under full sunlight (100 mW/cm^2): 2 h dipping time (red, solid line), 45 min dipping time: fresh cell (black, solid line), aged cell (blue, solid line). Dotted lines correspond to the dark current measurement.

dipping time		light intensity	J_{sc} (mA/cm^2)	V_{oc} (mV)	*F.F.*	η (%)
2 h		0.1 sun	1.23	706	0.65	5.96
		1 sun	7.07	766	0.39	2.14
45 min	fresh	0.1 sun	0.99	783	0.75	5.65
		1 sun	11.0	848	0.54	5.11
	aged	0.1 sun	0.93	816	0.78	6.23
		1 sun	9.41	902	0.68	5.80

Table 4.5. Photovoltaic parameters of C2 sensitized devices with different dipping time under various light intensities.

Photocurrent-voltage characteristics for the C2, C6, and C12 sensitized devices measured under simulated AM 1.5G sunlight are shown in Figure 4.11a and detailed photovoltaic parameters are summarized in Table 4.6. All of them yielded highly improved power conversion efficiencies of over 5 %, which were already higher than our best record of the cell with C106 (certified value of 4.99 %

from NREL). The C12 sensitized cell showed a high J_{sc} of 9.96 mA/cm^2, a V_{oc} of 887 mV, and a *F.F.* of 0.69, corresponding to an overall efficiency η of 6.10 % (active area of 0.4225 cm^2), which, at the time of this writing, is the highest report for a solid-state DSC. The IPCE spectra for the sensitizers are shown in Figure 4.11b. For C6 and C12, the IPCEs were over 70 % from 450 nm up to 570 nm. The C2 sensitized cell also had maximum IPCE of 70 % at 450 nm but the plateau was less broad. This shows that the enhanced light absorbing capabilities of the C dyes lead to improvements of the photocurrents due to a higher amount of injected charge carries. Integration of the IPCE spectra over the AM 1.5G standard solar emission spectrum, leads to the projected J_{sc} values for the C2, C6 and C12 of 10.5 mA/cm^2, 11.0 mA/cm^2 and 10.5 mA/cm^2, respectively, well in agreement with the measured values.

The solid-state cell with C12 was also measured at the National Renewable Energy Laboratory (USA) to obtain a certified value. Figure 4.12 illustrates the certified *J*-V characteristic of the C12 sensitized cell, which is the first time that a certified efficiency of over 6% has been achieved with a solid-state DSC.
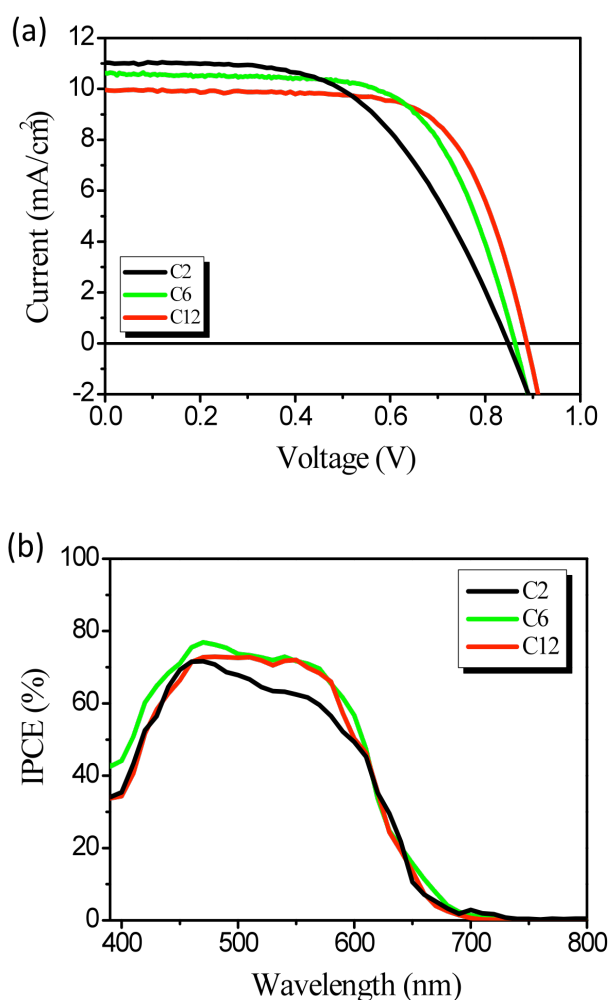

Figure 4.11. (a) *J*-V characteristics under full sunlight (100 mW/cm^2). (b) Photocurrent action spectrum of the devices with C2 (black), C6 (green) and C12 (red).

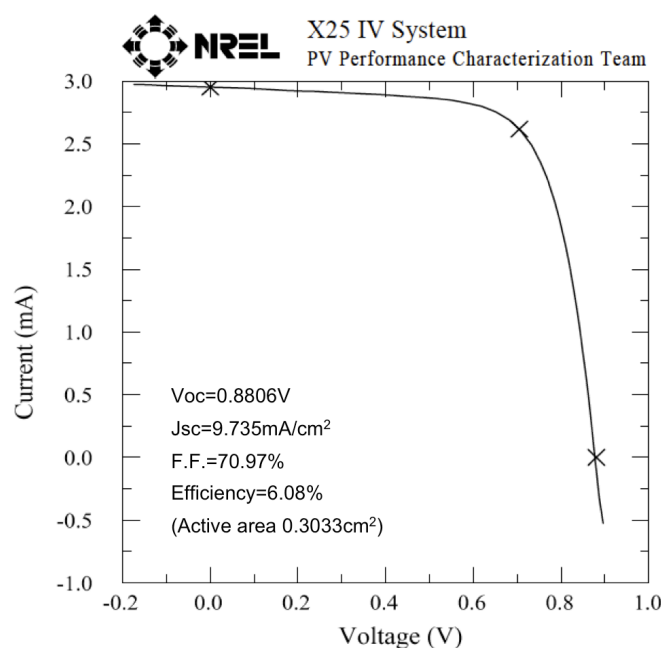| sensitizer	J_{sc} (mA/cm^2)	V_{oc} (mV)	F.F.	η (%)
C2	11.0	848	0.54	5.11
C6	10.6	862	0.65	5.93
C12	9.96	887	0.69	6.10

Table 4.6. Photovoltaic parameters of devices with C2, C6 and C12 under full sunlight (100 mW/cm^2).

Figure 4.12. *J*–V characteristics of a SSDSC sensitized with the C12 dye and measured by the NREL photovoltaic calibration laboratory under standard reporting conditions, i.e. illumination with AM 1.5G sunlight (intensity 100 mW/cm^2) and 298 K temperature. Cell active area tested (with a mask): 0.3033 cm^2.

Devices prepared with C6 and C12 containing longer alkyl chains produced moderately lower J_{sc} but higher V_{oc} and F.F. compared to the C2 sensitized cell (see Table 4.6). Transient photocurrent and photovoltage decay measurements were carried out to investigate an effect of the alkyl chain length in charge recombination. In Figure 4.13 the electron lifetime becomes longer by increasing the length of the alkyl chain, which indicates that the higher V_{oc} of the device with C12 dye is caused by the decrease in the recombination rate. Consequently, introducing longer alkyl chains in the linker part of the C dyes effectively suppressed charge recombination and reduced aggregate formation on the TiO$_2$ surface.

The charge collection efficiency (η_{cc}, $\eta_{cc} = 1/(1+(\tau_{trans}/\tau_e)^{18,\,19}$) also can be determined by the transient photocurrent and photovoltage decay measurement. The η_{cc} of the C12 sensitized cell, possessing the best performance among C dyes, showed over 90 % (see Figure 4.14). Here, the

ruthenium sensitizer Z907 was used for a comparison. The charge collection efficiency was slightly higher near short circuit conditions for the SSDSC device with C12. Going to higher forward bias the collection efficiency of devices sensitized by Z907 dropped faster than C12. The fact that the collection efficiency of DSCs with C12 stays stable over a wider potential range is one of the main reasons for the better performance of these cells. The high V_{oc} and high injection of charge carriers paired with the good charge collection efficiency lead to an impressive overall efficiency of more than 6 % under 1 sun illumination of SSDSC.
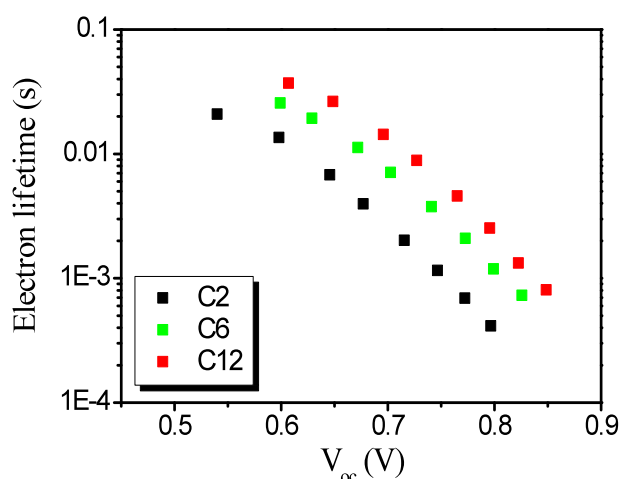

Figure 4.13. Electron lifetime of the C2 (black), C6 (green) and C12 (red) sensitized devices under different V_{oc} level.
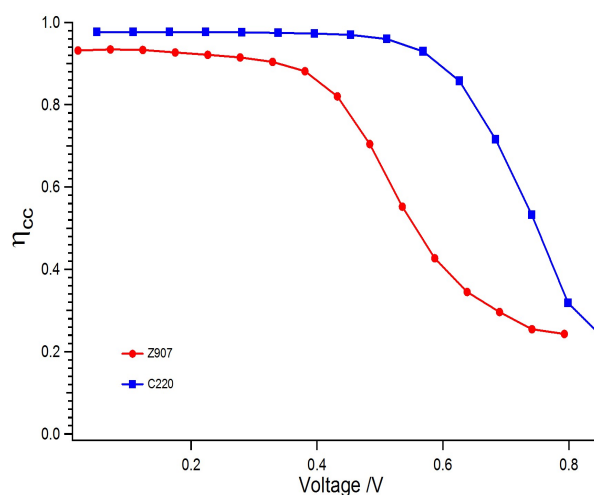

Fig. 4.14. Charge collection efficiency of the devices sensitized with C12 (blue) and Z907 (red) at 1 sun illumination.

Device fabrication of the SSDSCs sensitized with C2, C6, and C12 sensitizers

A mesoporous TiO$_2$ layer (~2 μm thick) was coated by the screen-printing technique with a Basic 23 nm paste. For C6 and C12 dye, TiO$_2$ electrodes were stained by immersing them into dye solutions

for 2 hours. For C2 dye, we immersed electrodes into dye solutions for 2 hours or 45 min. The concentration of dye solutions was 0.1 mM in a mixture of acetonitrile and *tert*-butyl alcohol (volume ratio: 1/1). Standard spiro-OMeTAD solution was applied for a HTM layer. As a counter electrode, Ag was evaporated on top of the HTM layer for the high efficiency.

4.2.3 Squaraine Dyes

Development of sensitizers with extended absorption capability into the infrared is one of the solutions to enhance light absorption. Organic dyes are much more easily tunable toward the near infrared compared to ruthenium dyes and it could enable an increase in their "light harvesting" potential at longer wavelengths. Squaraine dyes are well known to have intense absorption in the visible and near infrared regions. Therefore, they are good candidates for the co-sensitization or tandem cells. Co-sensitization or tandem cells have been demonstrated to improve light absorption and broaden the spectral response of DSCs by using a multiple dye system. For these applications, dyes should be complementary to each other by not overlapping in their absorption of solar light.

SQ1 and SQ2, which were synthesized by Dr. Nüesch group at Empa (Switzerland), were employed for SSDSCs in our group. SQ2 has a benzoindolium derivative instead of the indolium of SQ1 in Figure 4.15, which depicts molecular structures of SQ1 and SQ2. In UV-Vis spectrum (see Figure 4.16), they show intense narrow absorption bands, SQ2s absorption is slightly red-shifted to 662 nm in comparison to SQ1 with an absorption maximum at 647 nm due to the extended π-system of SQ2. Also, SQ2 has a slightly higher molar extinction coefficient of 319,000 $M^{-1}cm^{-1}$ compared to 292,000 $M^{-1}cm^{-1}$ of SQ1. Their extremely high molar absorption coefficients allow using thinner TiO_2 films, which is crucial in solid-state DSCs. In general, squaraine dyes aggregate easily on the TiO_2 surface therefore co-adsorbents have to be added into a dye solution to reduce dye aggregates. Yum *et al.* previously investigated the effect of the CDCA with SQ1 to reduce aggregation in the cells[20]. For this work, we added 10 mM of CDCA into dye solutions.
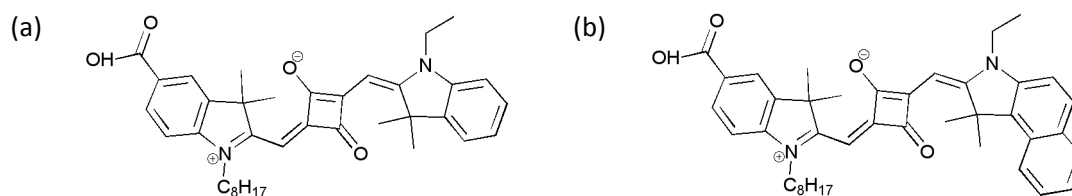

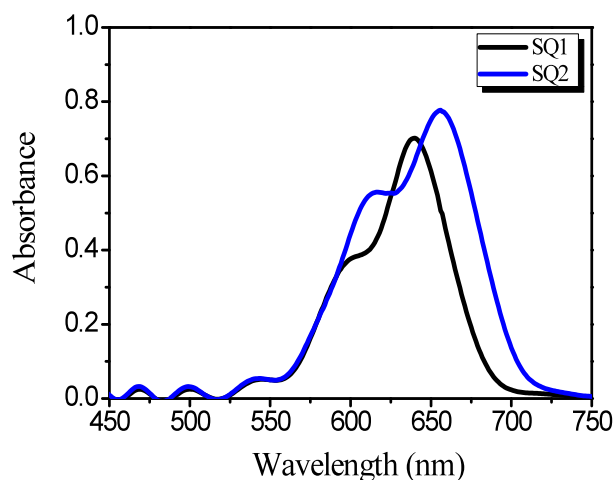Figure 4.15. Molecular structures of (a) SQ1 and (b) SQ2.

Figure 4.16. UV-Vis spectrum of SQ1 and SQ2 stained on 2 µm thick mesoporous TiO_2 films.

Photovoltaic performances of the squaraine-sensitized cells measured under standard global AM 1.5 solar condition are shown in Figure 4.17a. SQ2 sensitized solar cell generated a higher photocurrent of 4.95 mA/cm^2 and a photovoltage of 772 mV compared to SQ1 (see Table 4.7). Consequently, the overall power conversion efficiency of the device with SQ2 was increased by over 30 %. The improved J_{sc} of the SQ2 sensitized cell can be deduced from the red-shifted IPCE of SQ2 in Figure 4.17b. The red-shift of SQ2 in IPCE shows a good agreement with its UV-Vis spectrum. The improved V_{oc} of the SQ2 sensitized cell is caused by the upward shift of the quasi Fermi level of TiO_2 induced by the higher current densities of the SQ2 cell[21-23]. In addition, the enhanced electrical dipole moment of SQ2 might substantially contribute the overall open circuit voltage[24-26].

sensitizer	J_{sc} (mA/cm^2)	V_{oc} (mV)	F.F.	η (%)
SQ1	3.48	736	0.63	1.62
SQ2	4.95	772	0.56	2.15

Table 4.7. Photovoltaic parameters of devices with SQ1 and SQ2 under full sunlight (100 mW/cm^2).
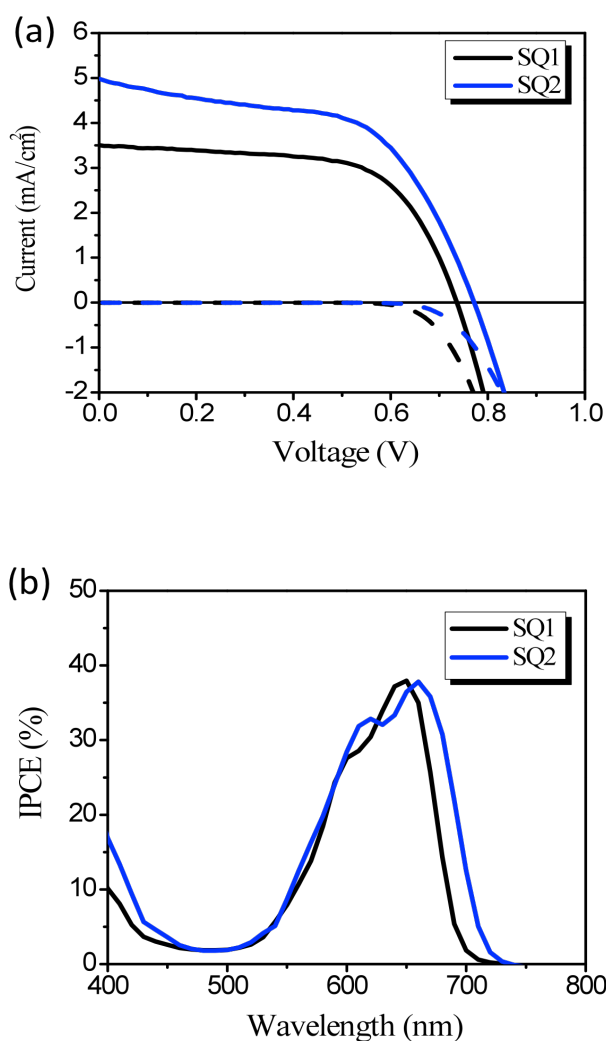
Figure 4.17. (a) *J*-V characteristics of the devices prepared with SQ1 (black) and SQ2 (blue) under full sunlight (100 mW/cm^2). Dotted lines correspond to the dark current measurement. (b) Photocurrent action spectrum of SSDSCs with SQ1 (black) and SQ2 (blue).

Device fabrication of the SSDSCs sensitized with squaraine sensitizers

A mesoporous TiO$_2$ layer (~1.8 μm thick) was coated by the doctor-blading technique with an Acidic 20 nm paste. TiO$_2$ electrodes were stained by immersing them into dye solutions for 4 hours. The concentration of dye solutions was 0.1 mM in ethanol and 10mM of CDCA as a co-adsorbent was added into the dye solutions. Standard spiro-OMeTAD solution was applied for a HTM layer. As a counter electrode, Au was evaporated on top of the HTM layer.

4. 3 Conclusions

In this chapter, we investigated photovoltaic performances and electronic properties of the devices with organic dyes having high molar extinction coefficients. DL series dyes are an analogue of the D9 dye using alkoxy triarylamine donors and a bisthiophene π-bridge instead of methoxy substituted triarylamine donor. The overall efficiency of the cell stained with D5L6, which did not have an alkoxy unit in triphenylamine donor, was higher than that of the D9 sensitized cell due to its extended π-conjugation of the π-bridge. The devices with D21L6 and D25L6 containing long alkoxy chains generated higher photocurrents than the cell with D5L6 owing to red-shifted IPCE. Moreover, the long alkoxy chains improved photovoltage by suppressing charge recombination. The device with D21L6 containing a hexyloxy moiety yielded the highest power conversion efficiency of 4.44 % among the cells sensitized with DL dyes.

C2, 6, and 12 possess cyclopentadithiophene segments as a π-bridge instead of the bisthiophene unit of D21L6 to extend π-conjugation. As a result, their molar extinction coefficients were remarkably increased and absorption spectra were red-shifted compared to D21L6. The cells sensitized with C2, 6 and 12 generated very high photocurrents of 10 mA/cm^2. Their power conversion efficiencies also improved significantly in comparison to our best record (4.99 %) with C106. The C2 and C6 containing shorter alkyl chains on the π-bridge, showed dye aggregates on the TiO$_2$ surface. The cells sensitized with C2 and C6 had a lower *F.F.* than that of C12 sensitized cell. The C12 sensitizer, which contained the longest alkyl chain on the π-bridge yielded the best efficiency of over 6 %, which is the highest record in spiro-OMeTAD based solid-state DSCs.

We employed another interesting dyes (coded as SQ1 and SQ2) to our SSDSCs. Squaraine dyes have strong absorptions in the visible and near infrared regions. They have relatively low efficiency of 2 %, however they can be employed to different device architectures such as tandem cells, Förster Resonance Energy Transfer (FRET), or co-sensitization to get a panchromatic response[27-29]. For instance, the SQ1 with energy relay dye in a SSDSC increased by 29 % in terms of power conversion efficiency by FRET[28]. Thus, near infrared dyes look promising for the improvement of photocurrents by expanding light absorption.

Bibliography

1.   A. Hagfeldt, G. Boschloo, L. Sun, L. Kloo and H. Pettersson, Chemical Reviews, **110** (11), 6595-6663 (2010).

2.   A. Mishra, M. Fischer and P. Bäuerle, Angewandte Chemie International Edition **48** (14), 2474-2499 (2009).

3.   S. Kim, J. K. Lee, S. O. Kang, J. Ko, J. H. Yum, S. Fantacci, F. De Angelis, D. Di Censo, M. K. Nazeeruddin and M. Grtäzel, J Am Chem Soc **128** (51), 16701-16707 (2006).

4.   Z. Ning, Q. Zhang, W. Wu, H. Pei, B. Liu and H. Tian, The Journal of Organic Chemistry **73** (10), 3791-3797 (2008).

5.   D. P. Hagberg, J.-H. Yum, H. Lee, F. De Angelis, T. Marinado, K. M. Karlsson, R. Humphry-Baker, L. Sun, A. Hagfeldt, M. Grätzel and M. K. Nazeeruddin, J Am Chem Soc **130** (19), 6259-6266 (2008).

6.   M. Wang, M. Xu, D. Shi, R. Li, F. Gao, G. Zhang, Z. Yi, R. Humphry-Baker, P. Wang, S. M. Zakeeruddin and M. Grätzel, Adv Mater **20** (23), 4460-4463 (2008).

7.   G. Li, K.-J. Jiang, P. Bao, Y.-F. Li, S.-L. Li and L.-M. Yang, New Journal of Chemistry **33** (4), 868-876 (2009).

8.   T. Horiuchi, H. Miura and S. Uchida, Chemical Communications (24), 3036-3037 (2003).

9.   J. H. Yum, D. Hagberg, S. J. Moon, K. Karlsson, T. Marinado, L. Sun, A. Hagfeldt, M. Nazeeruddin and M. Grätzel, Angewandte Chemie International Edition **48** (9), 1576-1580 (2009).

10.   D. P. Hagberg, Ph.D. Thesis, KTH (Stockholm) (2009).

11.   M. K. Nazeeruddin and M. Grätzel, Encyclopedia of Electrochemistry: Semiconductor Electrodes and Photoelectrochemistry; Wieley-VCH: Germany **6** (2002).

12.   U. Bach, Ph.D. Thesis, EPFL (Lausanne) (2000).

13.   U. B. Cappel, E. A. Gibson, A. Hagfeldt and G. Boschloo, The Journal of Physical Chemistry C **113** (15), 6275-6281 (2009).

14.   J. S. Henry and et al., Nanotechnology **19** (42), 424003 (2008).

15. G. Boschloo and A. Hagfeldt, Inorg. Chim. Acta **361** (3), 729-734 (2008).

16. H. J. Snaith, A. Petrozza, S. Ito, H. Miura and M. Grätzel, Adv Funct Mater **19** (11), 1810-1818 (2009).

17. S. Mikoshiba, S. Murai, H. Sumino, T. Kado, D. Kosugi and S. Hayase, Current Applied Physics **5** (2), 152-158 (2005).

18. Q. Wang, Z. Zhang, S. M. Zakeeruddin and M. Grätzel, The Journal of Physical Chemistry C **112** (17), 7084-7092 (2008).

19. Q. Wang, Z. Zhang, S. M. Zakeeruddin and M. Grätzel, The Journal of Physical Chemistry C **112** (28), 10585-10585 (2008).

20. J. H. Yum and et al., Nanotechnology **19** (42), 424005 (2008).

21. A. Kay and M. Grätzel, The Journal of Physical Chemistry **97** (23), 6272-6277 (1993).

22. G. Schlichthorl, S. Y. Huang, J. Sprague and A. J. Frank, The Journal of Physical Chemistry B **101** (41), 8141-8155 (1997).

23. A. Zaban, S. Ferrere and B. A. Gregg, The Journal of Physical Chemistry B **102** (2), 452-460 (1998).

24. F. Nüesch, F. Rotzinger, L. Si-Ahmed and L. Zuppiroli, Chemical Physics Letters **288** (5-6), 861-867 (1998).

25. F. De Angelis, S. Fantacci, A. Selloni, M. Grätzel and M. K. Nazeeruddin, Nano Lett **7** (10), 3189-3195 (2007).

26. T. Geiger, S. Kuster, J. H. Yum, S. J. Moon, M. K. Nazeeruddin, M. Grätzel and F. Nüesch, Adv Funct Mater **19** (17), 2720-2727 (2009).

27. B. E. Hardin, E. T. Hoke, P. B. Armstrong, J.-H. Yum, P. Comte, T. Torres, J. M. J. Fréchet, M. K. Nazeeruddin, M. Grätzel and M. D. McGehee, Nat Photon **3** (11), 667-667 (2009).

28. J. H. Yum, B. Hardin, S. J. Moon, E. Baranoff, F. Nüesch, M. McGehee, M. Grätzel and M. Nazeeruddin, Angewandte Chemie International Edition **48** (49), 9277-9280 (2009).

29. D. Kuang, P. Walter, F. Nuesch, S. Kim, J. Ko, P. Comte, S. M. Zakeeruddin, M. K. Nazeeruddin and M. Grätzel, Langmuir **23** (22), 10906-10909 (2007).

Chapter 5

Semiconductor Sensitizer – Sb$_2$S$_3$

5. 1 Introduction

Over the last few years semiconductor-sensitized or quantum dot (QD)-sensitized solar cells have drawn a lot of attention due to the intrinsically attractive properties of the QDs such as tunable band gap[1], high extinction coefficients[1, 2], and large intrinsic dipole moment[3, 4]. Moreover, the production of the semiconductor QDs or thin layers is significantly cheaper compared to their bulk counterparts, since they are synthesized at significantly low temperatures and with solution-based approaches. At this point, they are excellent materials as a light absorber for sensitized solar cells.

Semiconductors such as CdS, CdSe, CdTe, CuInS$_2$, Cu$_2$S, PbS, PbSe, InP, InAs, Ag$_2$S, Bi$_2$S$_3$ and Sb$_2$S$_3$ have been synthesized as quantum dots (QDs) and deposited onto wide-bandgap nanostructures as sensitizers. Depending on their size, these materials can absorb photons over a wide spectral range or within a confined window of the solar spectrum. For the QD deposition, the most common processes are chemical bath deposition (CBD)[5-8] and successive ionic layer adsorption and reaction (SILAR)[9], which are direct growth of the semiconductor QDs on the electrode surface by chemical reaction of ionic species. These in-situ methods provide high surface coverage and direct connection between QDs and TiO$_2$, leading to efficient charge injection from the QDs into the TiO$_2$. Also pre-synthesized monodisperse QDs can be deposited by using molecular linkers[10-13] or directly (without linker molecules) onto the TiO$_2$ surface[14, 15]. The properties of the semiconductor materials and the final performance of the solar cell strongly depend on the preparation methods.

Unfortunately, most of the QD materials are not chemically stable in I$^-$/I$_3^-$ redox electrolyte[16]. Therefore, a modification of the cell configuration[17, 18] using different redox couples[10, 19] has been

required to obtain efficient performances in semiconductor-sensitized cells (SSCs). Although diverse approaches have been employed to the SSCs, the power conversion efficiencies are still low (< 5 % in a liquid electrolyte, < 2 % in an organic hole conductor) as compared to DSCs and inorganic-organic hybrid solar cells.

5.1.1 Sb₂S₃ as a light absorber

Sb_2S_3 is a low-band gap semiconductor that has been used on a number of occasions to create novel solar cells. In its crystalline form (stibnite), the band gap is approximately 1.7-1.8 eV and its absorption coefficient is 1.8×10^5 cm^{-1} at 450 nm. It has previously been studied as a potential sensitizer in liquid electrolyte-based TiO_2 mesoscopic solar cells Sb_2S_3 was coated onto the semiconductor electron transporting film by chemical bath deposition (CBD)[20, 21]. The IPCE measured in this study was only 30 % and power conversion efficiency could not be measured due to an unstable photoelectrode in the liquid electrolyte. Recently, Hodes *et al*. reported a successful result of the Sb_2S_3 sensitized solid-state solar cells with CuSCN as an inorganic hole transport layer.[22] The power conversion efficiencies were respectively 3.8 % and 3.4 % under 10 and 100 % sun illumination. The IPCE obtained with such cells was 80 %.

In this chapter, Sb_2S_3 will be investigated as a light absorber in solid-state solar cells with spiro-OMeTAD. These experiments were done in collaboration with the group of Prof. Hodes at the Weizmann Institute of Science, Israel.

5. 2 Sb$_2$S$_3$-Sensitized Solid-State Solar Cells

For the Sb$_2$S$_3$ coated TiO$_2$ electrodes, we prepared mesoporous TiO$_2$ electrodes, which were coated with 20 and 30 nm size TiO$_2$ pastes by screen-printing and the doctor-blading technique, respectively. Prof. Hodes group deposited Sb$_2$S$_3$ layer on the In-OH-S coated TiO$_2$ electrodes, which we sent to them. The Sb$_2$S$_3$ layer was deposited by a CBD method. We fabricated Sb$_2$S$_3$-sensitized solid-state solar cells by using spiro-OMeTAD as a HTM and investigated the photovoltaic performance. The average local thickness of the stibnite layer was roughly 5-10 nm (estimated from XPS data) and the total (optical) thickness typically a few hundred nm. The Sb$_2$S$_3$ does not cover each TiO$_2$ particle conformally, but rather coats clusters of TiO$_2$ (see Figure 5.1).
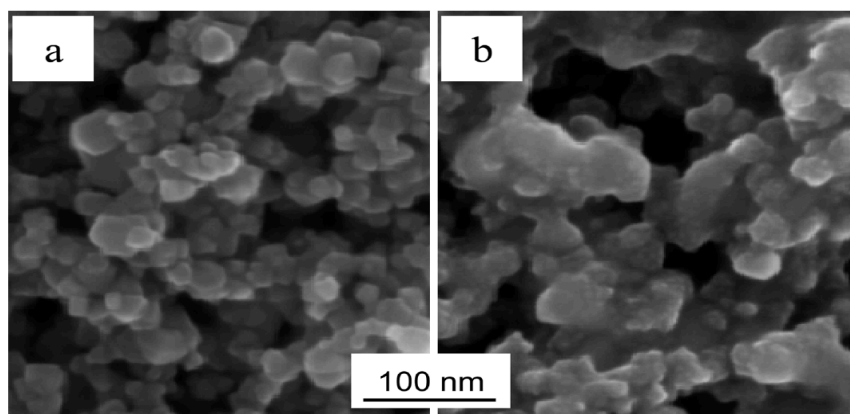

Figure 5.1. SEM pictures of (a) bare 30nmTiO$_2$ particles and (b) the Sb$_2$S$_3$ layer deposited and annealed on a 30 nm TiO$_2$/In-OH-S substrate (Measured by Prof. Hodes group).

The Sb$_2$S$_3$-sensitized solid-state solar cells were prepared by using spiro-OMeTAD solutions with and without dopant. Normally, oxidative chemical dopants, such as antimony salt or NOBF$_4$, are added to a standard spiro-OMeTAD solution in order to improve the cell performance[23] can increase the conductivity of the spiro-OMeTAD and therefore lead to better performances of the cells by improving fill factor. Tris(p-bromophenyl)ammoniumyl hexachloroantimonate (N(p-C$_6$H$_4$Br)$_3$SbCl$_6$, Sb dopant) was used as a dopant for the Sb$_2$S$_3$-sensitized cells.

Figure 5.2 illustrates the J–V characteristics of the Sb$_2$S$_3$-sensitized cells with and without Sb dopant. Under standard global AM 1.5 solar conditions, the Sb$_2$S$_3$-sensitized solid-state solar cell with Sb dopant showed an overall efficiency, η, of 3.11 %, with the corresponding photovoltaic parameters: J_{sc} = 10.5 mA/cm^2, V_{oc} = 610 mV and $F.F.$= 0.48. Under 0.1 and 0.5 sun, the overall efficiencies were, respectively, 5.23 and 4.01 %. The cell without dopant produced a slightly higher J_{sc} of 12.1 mA/cm^2, but V_{oc} and $F.F.$ were lower than those of the cell with dopant. Thus, the chemical dopant contributed to an improvement of V_{oc} and $F.F.$ in the cell. The detailed photovoltaic parameters at various light intensities are summarized in Table 5.1. The cells with and without dopant possess high overall

efficiencies of 5 % under 0.1 sun illumination, but the efficiencies measured at 1 sun irradiation condition are low, about 3 % due to the loss of photocurrent and fill factor. The fill factor loss plausibly stems from a resistive loss. It should be noted that in this study our active area is 0.49 cm^2, which is 3.3 times bigger than that of the cell with CuSCN as a HTM[22] increasing the IR losses due to higher photocurrents. In addition, the Sb$_2$S$_3$/spiro-OMeTAD interface is the most crucial parameter linked to diminished short circuit current values and fill factor. The interfacial property has been regarded as an important issue in sprio-OMeTAD based solid-state cells.[24, 25] In quantum dots or semiconductor sensitizer based cells, it appears even more problematic. Lee *et al.* have pointed to a more hydrophilic property of quantum dots after deposition in hydrophilic alcoholic or aqueous medium than that of typical molecular dyes, which leads to poor pore-filling of spiro-OMeTAD.[26] Moreover, Sb$_2$S$_3$ occupies considerably more space than dyes, resulting in a significantly narrower pathway for the introduction of spiro-OMeTAD. Experiments performed using a TiO$_2$ film composed of 20 nm sized nanoparticles (having a smaller pore size than films comprised of 30 nm particles) yielded an efficiency of less than 1 % at full light intensity.

	light intensity	J_{sc} (mA/cm^2)	V_{oc} (mV)	F.F.	η (%)
standard spiro-OMeTAD solution	0.1 sun	1.54	498	0.60	4.86
	0.5 sun	6.88	542	0.38	3.05
	1 sun	12.1	558	0.33	2.26
spiro-OMeTAD solution with Sb dopant	0.1 sun	1.44	545	0.64	5.23
	0.5 sun	6.61	594	0.52	4.01
	1 sun	10.5	610	0.48	3.11

Table 5.1. Photovoltaic parameters of Sb$_2$S$_3$-sensitized devices with and without Sb dopant under various light intensities.
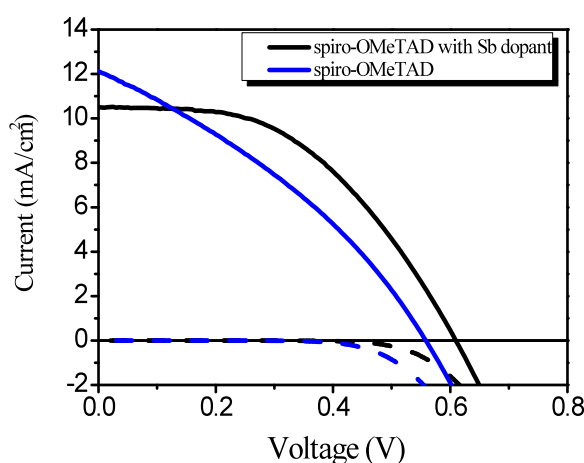

Figure 5.2. *J*-V characteristics of Sb$_2$S$_3$-sensitized cells with Sb dopant (black) and without dopant (blue) under full sunlight (100 mW/cm^2). Dotted lines correspond to the dark current measurement.

The IPCE of the Sb$_2$S$_3$-sensitized solid-state solar cell exhibits very high values, i.e. 70 – 90 % between excitation wavelengths of 420 and 650 nm (see Figure 5.3). Assuming a 10 % optical loss in the conducting glass[27, 28], the internal quantum efficiency ranged from 80 – 100 %. The observed IPCE onset at ca. 750 nm is consistent with an approximate 1.75 eV band gap of crystalline Sb$_2$S$_3$.
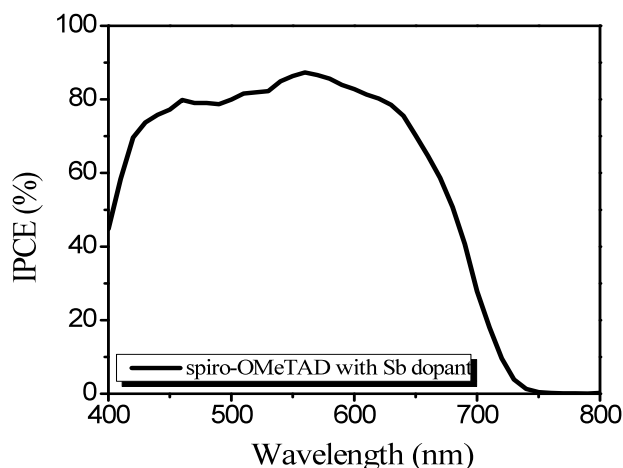

Figure 5.3. Photocurrent action spectrum of Sb$_2$S$_3$-sensitized solid-state cell.

As mentioned above, the photocurrent loss was found in the 1 sun irradiation condition. In order to investigate this loss, we investigated current dynamics of the Sb$_2$S$_3$-sensitized solid-state solar cell measured over the course of light chopping (~3.5 s) at various light intensities. Figure 5.4 shows the current dynamics as a function of light intensity where the dashed lines show the individual photocurrents normalized to 1 sun. Above 0.305 sun, these currents are notably characterized by non-linearity and lack of plateau formation. When normalized to values of J_{sc} measured under 1 sun illumination, the J_{sc} values measured at the lower light intensities are high in comparison to that measured under 1 sun. At the lowest light intensities examined i.e. 0.009 and 0.095 sun, the normalized J_{sc} values are 17.5 and 15.1 mA/cm^2, which are, respectively, 165 and 143 % of the J_{sc} value measured at 1 sun. The IPCE measured under low light intensity and integrated from 350 to 800 nm yields a J_{sc} value of 16.0 mA/cm^2, which is higher than the value of 10.5 mA/cm^2 measured under AM 1.5G irradiation. In the current dynamic measurements, constant currents were maintainable (plateaus were formed) from the initial to final illumination times up to 0.305 sun intensity, but at the higher light intensities examined (i.e. 0.530, 0.641, and 1.000 sun) the J_{sc} decays (non-linear) during the illumination period with a characteristic non-linearity increasing as the light intensity increases. At 1 sun, an 18 % reduction in the final measured J_{sc} value was found. This might indicate a limitation of the J_{sc} by the rate of hole diffusion to the back contact and can explain, to a large extent, the sub-linear increase in photocurrent with light intensity.
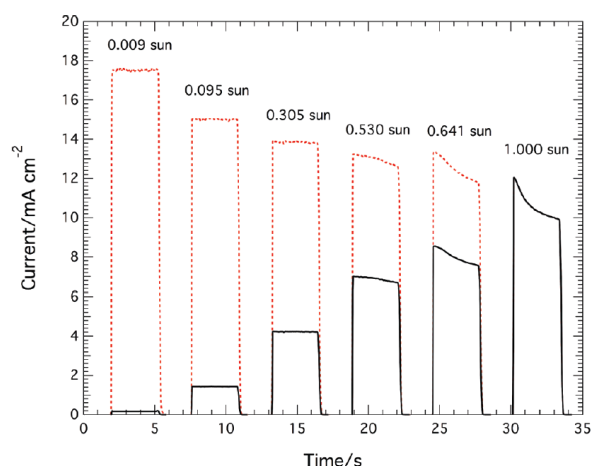
Figure 5.4. The current dynamics of Sb$_2$S$_3$-sensitized solid-state cell as various light intensities: measured currents (solid line) and normalized currents (1 sun, dashed line).

As for the J-V characteristics, the cell with Sb dopant showed higher V_{oc} about 50 mV compared to that of the cell without dopant. The transient photocurrent and photovoltage decay measurement were carried out to investigate an effect of the dopant. Figure 5.5 shows that Sb dopant leads to an increase of the electron lifetime in the Sb$_2$S$_3$-sensitized cell, which is expected by the effect of reduced recombination. The enhanced open circuit voltage of the cell with dopant can be deduced from a reduction of the charge recombination.

The main loss of the Sb$_2$S$_3$-sensitized solid-state cell with spiro-OMeTAD is low V_{oc} and $F.F$. The overall efficiency of the cell with spiro-OMeTAD can be improved by modifying the surface states and using larger TiO$_2$ particles. In QD sensitized cells, decylphosphonic acid (DPA)[29] is used as an interfacial modifier to improve the photovoltage by suppressing charge recombination[26]. Also using larger TiO$_2$ particles for the mesoporous TiO$_2$ electrodes could increase fill factor through enhanced pore-filling of spiro-OMeTAD into the TiO$_2$ pores.
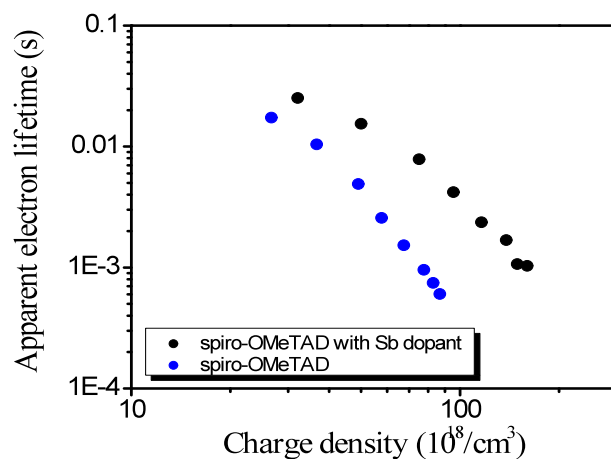

Figure 5.5. Apparent electron lifetime (τ_e) of Sb$_2$S$_3$-sensitized cells with Sb dopant (black) and without dopant (blue).

Device fabrication of the Sb_2S_3-sensitized cells with spiro-OMeTAD

The ~2 μm thick mesoporous layer composed of 30 nm TiO_2 particles was coated onto TCO substrate using the doctor-blading technique. In a stepwise fashion, $In_x(OH)_yS_z$ (In-OH-S) (ca. 1 nm thickness) was first deposited on the TiO_2 film by CBD followed by a CBD deposition of Sb_2S_3 onto these TiO_2/In-OH-S substrates utilizing a solution of $SbCl_3$ and $Na_2S_2O_3$. The as-deposited orange films of amorphous Sb_2S_3 were annealed under N_2 at 300 °C for 30 min to give dark-brown crystalline stibnite. The films were removed from the oven immediately after annealing and were allowed to cool in air. The organic hole conductor, spiro-OMeTAD was then coated on top of the Sb_2S_3/TiO_2 film by spin coating of a 0.17 M chlorobenzene solution of spiro-OMeTAD containing three additives: 19 mM tBP, 10 mM LiTFSI, and 0.30mM Sb dopant at 2000 rpm for 30 seconds. The device fabrication was completed by thermal evaporation of ~100 nm of gold as a counter electrode. All of the fabrication steps and photovoltaic measurements were carried out in air and at room temperature.

5. 3 Conclusions

From the results presented herein Sb_2S_3 appears to be one of the most promising medium-band gap semiconductors for replacement of the sensitizer as a light absorber in solid-state TiO_2 mesoscopic solar cells. An efficiency, η, of 5.2 % was reached under 10 % sun light intensity with an IPCE reaching almost 90 %, which indicates further improvement of the performance under full sunlight. The mechanism of loss of photo-induced charges at higher light intensities still remains to be resolved. Improvements in the interfacial properties of Sb_2S_3 and spiro-OMeTAD should likewise lead to an enhanced overall device performance.

Bibliography

1. W. W. Yu, L. Qu, W. Guo and X. Peng, Chemistry of Materials **15** (14), 2854-2860 (2003).

2. P. Wang, S. Zakeeruddin, J. Moser, R. Humphry-Baker, P. Comte, V. Aranyos, A. Hagfeldt, M. Nazeeruddin and M. Grätzel, Adv Mater **16** (20), 1806-1811 (2004).

3. R. Vogel, K. Pohl and H. Weller, Chemical Physics Letters **174** (3-4), 241-246 (1990).

4. R. Vogel, P. Hoyer and H. Weller, The Journal of Physical Chemistry **98** (12), 3183-3188 (1994).

5. O. Niitsoo, S. K. Sarkar, C. Pejoux, S. R¸hle, D. Cahen and G. Hodes, Journal of Photochemistry and Photobiology A: Chemistry **181** (2-3), 306-313 (2006).

6. L. J. Diguna, Q. Shen, J. Kobayashi and T. Toyoda, Applied Physics Letters **91** (2), 023116-023113 (2007).

7. Q. Shen, J. Kobayashi, L. J. Diguna and T. Toyoda, J Appl Phys **103** (8), 084304-084305 (2008).

8. S. Gorer and G. Hodes, The Journal of Physical Chemistry **98** (20), 5338-5346 (1994).

9. Y. F. Nicolau, M. Dupuy and M. Brunel, Journal of The Electrochemical Society **137** (9), 2915-2924 (1990).

10. I. n. Robel, V. Subramanian, M. Kuno and P. V. Kamat, J Am Chem Soc **128** (7), 2385-2393 (2006).

11. T. Lopez-Luke, A. Wolcott, L.-p. Xu, S. Chen, Z. Wen, J. Li, E. De La Rosa and J. Z. Zhang, The Journal of Physical Chemistry C **112** (4), 1282-1292 (2008).

12. K. S. Leschkies, R. Divakar, J. Basu, E. Enache-Pommer, J. E. Boercker, C. B. Carter, U. R. Kortshagen, D. J. Norris and E. S. Aydil, Nano Lett **7** (6), 1793-1798 (2007).

13. A. Kongkanand, K. Tvrdy, K. Takechi, M. Kuno and P. V. Kamat, J Am Chem Soc **130** (12), 4007-4015 (2008).

14. S.-C. Lin, Y.-L. Lee, C.-H. Chang, Y.-J. Shen and Y.-M. Yang, Applied Physics Letters **90** (14), 143517-143513 (2007).

15.   Y.-L. Lee, B.-M. Huang and H.-T. Chien, Chemistry of Materials **20** (22), 6903-6905 (2008).

16.   G. Hodes, The Journal of Physical Chemistry C **112** (46), 17778-17787 (2008).

17.   G. Sixto and et al., Nanotechnology **20** (29), 295204 (2009).

18.   Y. L. Lee and Y. S. Lo, Adv Funct Mater **19** (4), 604-609 (2009).

19.   H. Lee, M. K. Wang, P. Chen, D. R. Gamelin, S. M. Zakeeruddin, M. Grätzel and M. K. Nazeeruddin, Nano Lett **9** (12), 4221-4227 (2009).

20.   R. Vogel, P. Hoyer and H. Weller, Journal of Physical Chemistry **98** (12), 3183-3188 (1994).

21.   C. Chone and G. Larramona, FR2899385-A1, Octorber 5. (2007).

22.   Y. Itzhaik, O. Niitsoo, M. Page and G. Hodes, Journal of Physical Chemistry C **113** (11), 4254-4256 (2009).

23.   U. Bach, Ph. D., EPFL, 2000.

24.   L. Schmidt-Mende and M. Grätzel, Thin Solid Films **500** (1-2), 296-301 (2006).

25.   I. K. Ding, N. Tetreault, J. Brillet, B. E. Hardin, E. H. Smith, S. J. Rosenthal, F. Sauvage, M. Grätzel and M. D. McGehee, Adv. Funct. Mater. **19** (15), 2431-2436 (2009).

26.   H. Lee, H. C. Leventis, S. J. Moon, P. Chen, S. Ito, S. A. Haque, T. Torres, F. Nüesch, T. Geiger, S. M. Zakeeruddin, M. Grätzel and M. K. Nazeeruddin, Adv. Funct. Mater. **19** (17), 2735-2742 (2009).

27.   L. Brus, Journal of Physical Chemistry **90** (12), 2555-2560 (1986).

28.   S. Wenger, M. Schmid, G. Rothenberger, M. Grätzel and J. O. Schumacher, presented at the 24th EU PVSEC, Hamburg, Germany, 2009 (unpublished).

29.   J. M. Kroon, N. J. Bakker, H. J. P. Smit, P. Liska, K. R. Thampi, P. Wang, S. M. Zakeeruddin, M. Grätzel, A. Hinsch, S. Hore, U. Würfel, R. Sastrawan, J. R. Durrant, E. Palomares, H. Pettersson, T. Gruszecki, J. Walter, K. Skupien and G. E. Tulloch, Progress in Photovoltaics: Research and Applications **15** (1), 1-18 (2007).

Chapter 6

Porphyrin Sensitized Solid-State Solar Cells

6. 1 Introduction

6.1.1 Porphyrin sensitizers

Porphyrin-based chromophores capture sunlight and convert it into chemical energy in plants. Dye-sensitized solar cells also use discrete chromophores to harvest light, so the DSC is often said to accomplish artificial photosynthesis. Accordingly, along with commonly used Ru-based dyes, numerous porphyrins have been synthesized to mimic the reactivity and functionality of natural photosynthesis. They have appropriate LUMO and HOMO energy levels for use with TiO_2 in the DSC and very intense absorption of the Soret band at about 400-450 nm, as well as the Q band at about 500-650 nm[1]. Moreover, they possess very high molar extinction coefficient of 10^5 $M^{-1}cm^{-1}$ in the region of the Soret band. As such, porphyrin derivatives are suitable sensitizers to obtain panchromatic response in DSCs. Porphyrin sensitized cells have been demonstrated, but their power conversion efficiencies have been reported in the range of 5–7 %, which is relatively low compared to ruthenium and organic dyes. One of the reasons causing a low efficiency is the absorption trough between the Soret and Q bands, which decreases the light harvesting efficiency[2]. Aggregations of porphyrin dyes on the TiO_2 surface also cause a low photovoltaic performance, leading to self-quenching of the excited state dye. Therefore, using co-adsorbents is necessary to suppress dye aggregation.

The most commonly used porphyrins are Zn-free and Zn derivatives of the *meso*-benzoic acid substituted porphyrin (see Figure 6.1). There have been various approaches to modify and tune the photophysical properties of porphyrins: porphyrin with Cu as a central metal ion instead of Zn[3, 4],

porphyrins with phosphonate anchoring groups[5], and modifications of the *meso*-tetraphenylporphyrins by substitution at the *β*-position with different functional groups which extend the π systems to enhance the red-absorbing Q bands, as well as optimize the energy levels[6-9].
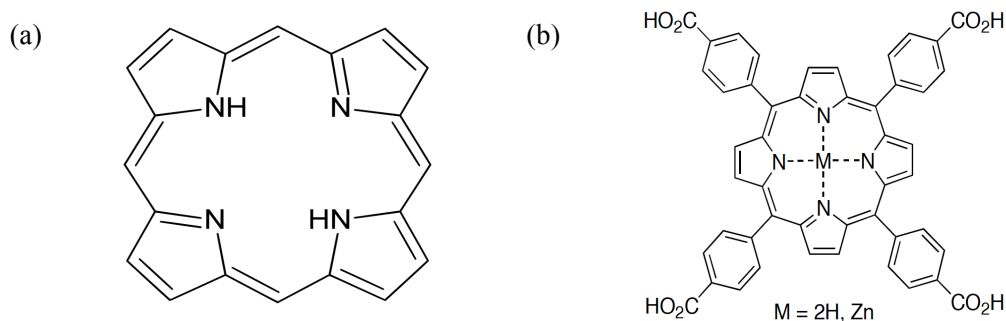

Figure 6.1. (a) The simplest structure of the porphyrin and (b) Tetrakis(4-carboxyphenyl)porphyrins.

6.1.2 TiO$_2$-P3HT hybrid solar cells

Much attention has been focused on organic-inorganic hybrid solar cells due to various advantages of the materials: solution processability, high hole mobility, and strong absorption of conjugated polymers and relatively high electron mobility, high electron affinity, and good chemical and physical stability of inorganic semiconductors. In particular, regioregular poly(3-hexylthiophene)(P3HT) and mesoporous TiO$_2$ hybrid solar cells have been demonstrated like a solid-state DSC. However, power conversion efficiencies of the TiO$_2$-P3HT hybrid cell are very low less than 1 % owing to the poor interfacial contact between the organic and inorganic materials[10, 11]. To improve device performance, numerous approaches have been employed: modifications of TiO$_2$ films with various morphologies such as mesoporous structure or nanotube array and TiO$_2$ surface modifications by chemisorption of carboxylate, phosphonate or sulfonate. The TiO$_2$ surface was changed to be hydrophobic with organic molecules, leading to a better interfacial contact with the hydrophobic organic polymer. This improved contact enhances the electronic coupling between the two components because of large orbital overlapping. As a result, the organic molecules play a role as an electronic mediator that enhances the electron transfer efficiency from polymer to metal oxide[12]. Efficient electron transfer through a mediator has been widely reported for other experimental systems[13, 14].

Recently, sensitizers containing carboxylic group have been employed to improve the interfacial interaction between TiO$_2$ and P3HT[12, 15, 16]. If a dye, which absorbs light in near infrared region, combines with P3HT, which has a strong absorption in the visible region, it will not only improve a power conversion efficiency of the P3HT cell but also obtain a panchromatic response in light-to-current conversions. A high efficiency of 3.1 % was reported for the near infrared dye (SQ1) sensitized TiO$_2$/P3HT hybrid cell and it resulted from extended light harvesting by two

complementary sensitizers (SQ1 and P3HT) and efficient hole transfer of P3HT[17]. This efficiency is improved remarkably compared to 1.3 % of the ruthenium dye sensitized TiO_2/P3HT hybrid cell. However, the photovoltaic performance of the dye-sensitized TiO_2/P3HT hybrid cell could be further enhanced through various approaches: optimization of TiO_2 morphology, in-situ polymerization of P3HT for enhancing pore-filling and utilization of the additives such as *t*BP and Li salt.

In this chapter, a porphyrin sensitizer (coded as YD2) will be investigated for its photovoltaic performance in different cell architectures: YD2 sensitized solid-state cell, co-sensitization with an organic sensitizer, and YD2 sensitized TiO_2/P3HT hybrid solar cells.

6. 2 Porphyrin Sensitizer with Different HTMs

Recently, Bessho *et al.* reported a very high power conversion efficiency of 11 % using a porphyrin dye (coded as YD2) under standard AM 1.5G conditions in a liquid electrolyte-based cell[18]. This result is the highest reported power conversion efficiency for the porphyrin sensitized DSCs. The structure of the YD2 sensitizer is shown in Figure 6.2.The porphyrin ring has donor and acceptor substituents: a diarylamino donor group attached to the porphyrin ring acts as an electron donor, and the ethynylbenzoic acid moiety serves as an acceptor. The porphyrin chromophore itself constitutes the π-bridge in this D-π-A structure[19, 20]. The YD2 sensitizer has strong absorption of the Soret band at 444 nm, as well as the Q-band at 648 nm (see Figure 6.3). It also possesses very high molar extinction coefficients like other porphyrin dyes: 217,000 $M^{-1}cm^{-1}$ at 444 nm and 33,700 $M^{-1}cm^{-1}$ at 648 nm. YD2 sensitizer looks promising for solid-state solar cells incorporated into thin TiO_2 films due to its high extinction coefficients and strong absorption in the visible and near infrared region.
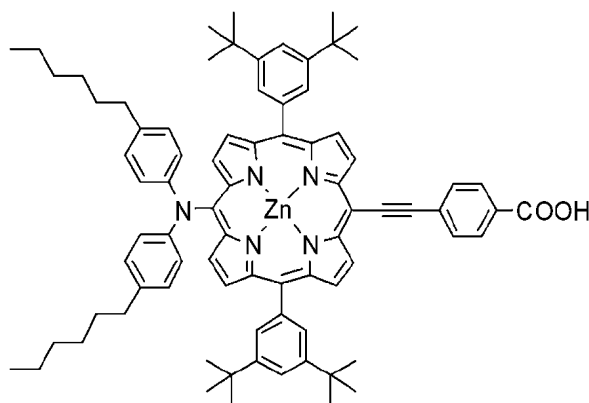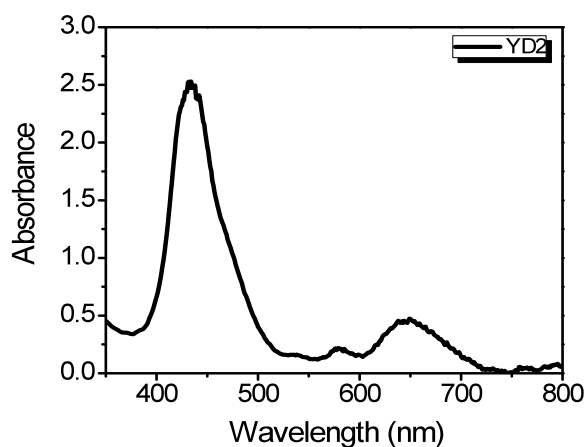

Figure 6.2. Molecular structure of the YD2 dye.

Figure 6.3. UV-Vis spectrum of YD2 stained on a 2 μm thick mesoporous TiO_2 film.

6.2.1 YD2 with spiro-OMeTAD

To investigate the photovoltaic performances of YD2 sensitized solid-state cells, our standard HTM, spiro-OMeTAD, was used. Figure 6.4a shows J-V characteristics of a device prepared with the YD2 sensitizer under various intensities of light. The photovoltaic performance was very poor due to a low J_{sc} of 2.56 mA/cm^2 (see Table 6.1). The low photocurrent results from the low IPCEs of the cell and a lack of the light harvesting in the 480-630 nm range. In the IPCE spectrum (see Figure 6.4b), we can clearly see two main peaks corresponding to the absorption of Soret and Q-band, but the IPCE values of those peaks are only 28 % and 20 %, respectively. These IPCE values are oddly low compared to its high extinction coefficients. This may be attributed to aggregation of the porphyrin molecules, as most of porphyrin dyes have shown to aggregate strongly on the TiO$_2$ surface[21-24]. Moreover, the aggregation becomes stronger as the dye molecule size increases. As a result, the substituted porphyrins, which are larger molecules, possess lower IPCEs than the unsubstituted porphyrins. Rochford et al. reported that aggregates did not contribute to photocurrent generation in tetrachelate porphyrin sensitized devices[22]. For the YD2 sensitizer, we need to optimize the amount of the co-adsorbent to reduce aggregation.

light intensity	J_{sc} (mA/cm^2)	V_{oc} (mV)	F.F.	η (%)
0.1 sun	0.25	745	0.81	1.60
0.5 sun	1.40	802	0.79	1.76
1 sun	2.56	827	0.77	1.64

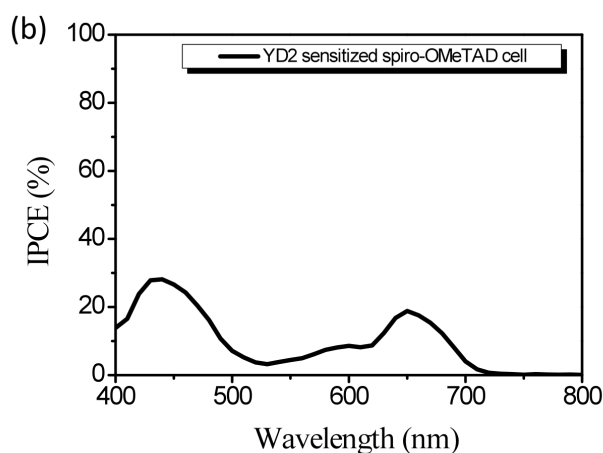Table 6.1. Photovoltaic parameters of the device with YD2.
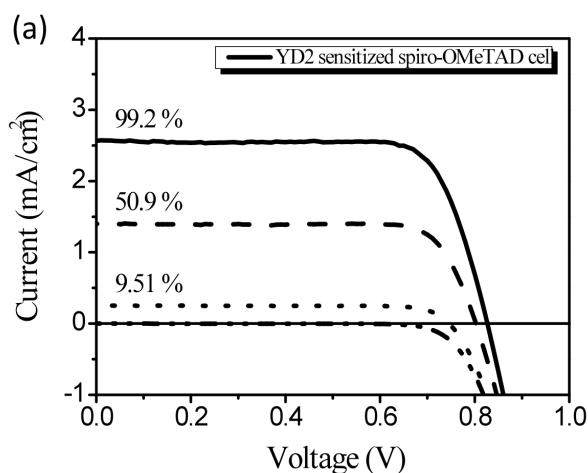
Figure 6.4. (a) *J*-V characteristics of the device sensitized with YD2 sensitizer under various light intensities. (b) Photocurrent action spectrum of the device.

Co-sensitization could be a judicious concept in order to increase the light harvesting by a complementary spectral response. We employed a C6 sensitizer (see Chapter 4) in combination with the YD2 sensitized TiO_2 film. The C6 dye has an absorption maximum at 555 nm that correspond with the minimum of the IPCE response of YD2. Hence, the co-sensitization by C6 dye could increase the light harvesting in the green wavelength region, leading to an improvement of the photocurrent.

For co-sensitization, the TiO_2 film was first stained with YD2 by immersing the film into a dye solution for 16 hours, followed by dipping the electrode into a C6 dye solution for 30 minutes and then washing with acetonitrile to remove excess dyes on the TiO_2 surface. The IPCE of the devices co-sensitized with YD2 and C6 dyes is shown in Figure 6.5a. The peaks corresponding to two different dyes are clearly displayed in the IPCE spectra of the co-sensitized devices. The co-sensitization by C6 dye results in a significant enhancement of the photocurrent in the spectral region of 480–580 nm, where the IPCE spectrum of YD2 shows a dip. Moreover, the IPCE values of YD2 were increased by 35 % at 440 nm and 45 % at 660 nm in the YD2/C6 co-sensitized cell, compared to those of the cell sensitized with YD2 alone. In general, an IPCE value of the YD2 dye alone is less than the IPCE of the device made by co-sensitization. This is because the dye molecules that were first adsorbed are partially desorbed when the electrode is exposed to the second dye solution. However, if the first dye exhibits significant aggregation, the second dye can act as a co-adsorbent, leading to retardation of the aggregation like has been observed with CDCA[25]. As mentioned above, the YD2 dye can easily aggregate on the TiO_2 surface. The C6 dye then reasonably inhibited the aggregation of YD2 and resulted in an improvement of the incident-photon-to-current conversion efficiency in the co-sensitized cell.
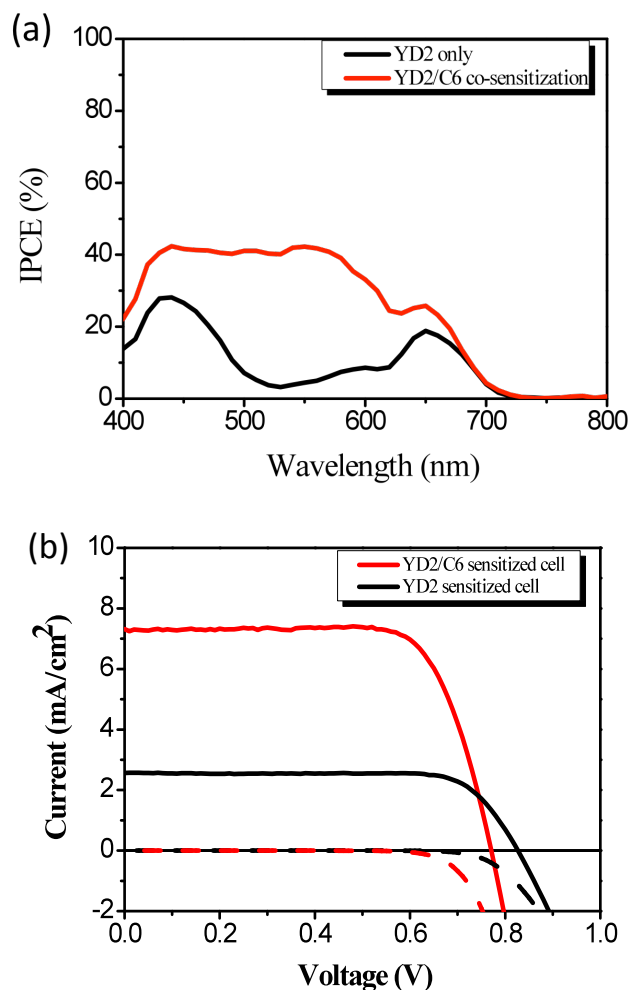
Figure 6.5. (a) Photocurrent action spectrum of the devices with YD2 (black line) and YD2/C6 (red line). (b) J-V characteristics of the devices sensitized with YD2 (black line) and YD2/C6 (red line) under full sunlight (100 mW/cm^2). Dotted lines correspond to the dark current measurement.

The photovoltaic parameters of these solar cells are given in Table 6.2. The device based on the co-adsorbed dyes C6 and YD2 produced 3 times higher J_{SC} and 2.5 times increased power conversion efficiency in comparison to those of the cell sensitized with YD2 alone (see Figure 6.5a). This enhancement results from filling the absorptivity-dip and increasing IPCE values between the Soret and Q bands of YD2, and by suppressing dye aggregation.

sensitizers	J_{sc} (mA/cm^2)	V_{oc} (mV)	F.F.	η (%)
YD2 only	2.56	827	0.77	1.64
YD2/C6	7.32	770	0.74	4.11

Table 6.2. Photovoltaic parameters of the devices with YD2 and YD2/C6 under full sunlight (100 mW/cm^2).

6.2.2 YD2 with P3HT

The overall efficiency of the YD2/C6 co-sensitized device was improved compared to the YD2 sensitized cell, but this efficiency is lower than that of the C6 sensitized device (5.93 % in Chapter 4). In this section we investigate a new efficient system for the YD2 sensitizer by using P3HT as a HTM as well as a light absorber. P3HT is a widely used semiconducting polymer that has been employed in combination with acceptors such as PCBM and TiO_2 in bulk heterojunction photovoltaic cells. As mentioned in the introduction, P3HT possesses a high hole mobility and absorbs light strongly in the spectral region of 400-630 nm, where the light harvesting of YD2 is insufficient. In figure 6.6, the absorption peak of the P3HT coated TiO_2 film shows no blue-shift in comparison to that of pristine P3HT film, suggesting a high degree of π-π stacking of the chains is still occurring within the pores[26]. In addition, the absorption bands of the YD2 dye and P3HT complement each other. This should lead to an enhancement of the light harvesting.
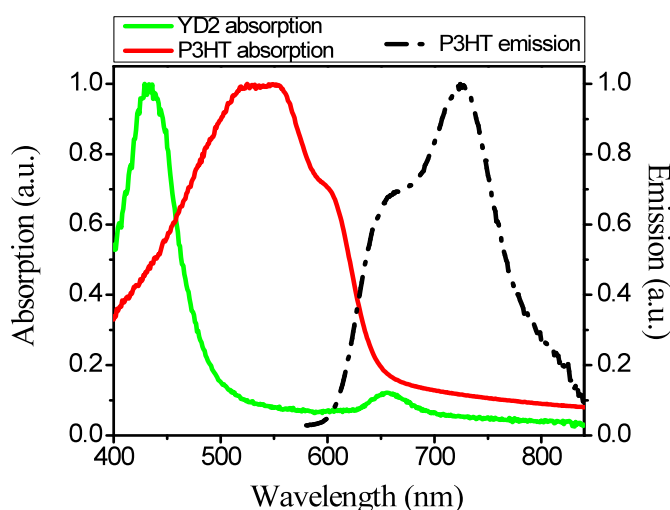

Figure 6.6. UV-Vis absorption of YD2 (green, solid line) sensitized TiO_2 film and P3HT (red, solid line) infiltrated TiO_2 film (1 μm thick and 75 nm TiO_2 particles). Emission spectrum of pristine P3HT film (black, dash line).

For the P3HT based cells, we modified our mesoporous TiO_2 electrodes in order to infiltrate P3HT chains into TiO_2 pores easily. Because spin coating method can cause incomplete pore-filling of the P3HT in the pores of the TiO_2[27]. TiO_2 electrodes were deposited using a paste containing 75 nm TiO_2 particles and the film thickness was less than 1 μm. We employed a P3HT solution on top of the YD2 sensitized TiO_2 film by spin coating. Figure 6.7 is described a simplified energy band diagram of the mesoporous TiO_2/P3HT hybrid solar cells, illustrating the likely energy cascade reaction. The band alignment among TiO_2, YD2, and P3HT is such that exciton dissociation and charge transfer at the interface is energetically favourable.
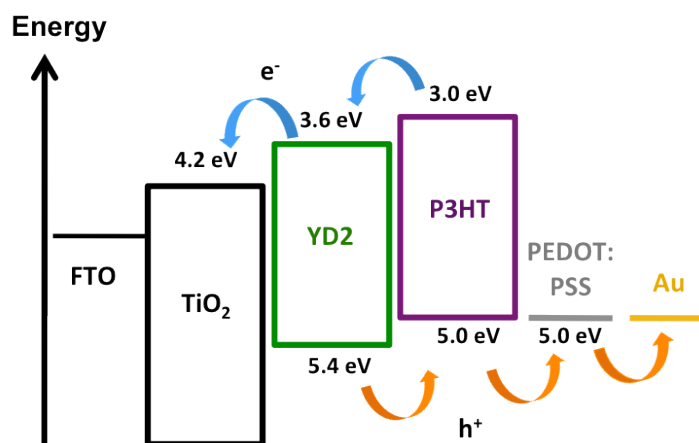
Figure 6.7. Energy band diagram of YD2 sensitized TiO$_2$/P3HT hybrid solar cell.

In Figure 6.8a, a comparison of the IPCE in photovoltaic devices based on P3HT and spiro-OMeTAD is displayed. The IPCE of the P3HT based cell improved remarkably compared to that of the spiro-OMeTAD based cell: the P3HT, as a sensitizer, completely filled the valley where YD2 did not absorb light and the IPCE values (at 440 nm and 650 nm) of YD2 were also enhanced significantly. At 440 nm, near Soret band maximum, the IPCE reaches 69 %, which is a 3-fold increase compared to that of the spiro-OMeTAD based device. The IPCE value in near infrared region is also about 50 %. Thus, both Soret and Q band feature of the YD2 dye are enhanced in the IPCE spectrum of the P3HT based cell. This reveals that charge carrier injection at the YD2/TiO$_2$ interface as well as corresponding electron collection within TiO$_2$ electrode is improved compared to the spiro-OMeTAD cell. The IPCE spectrum of the P3HT based cell shows effective panchromatic light harvesting by the combination of the "two sensitizers".

The photovoltaic performance of the P3HT based cell measured under standard AM 1.5G condition is shown in Figure 6.8b. The TiO$_2$/P3HT hybrid cell generates very high J_{sc} of 12.1 mA/cm^2 and this high photocurrent is ascribed to an enhancement of the IPCE by efficient photosensitizing effect of YD2 and P3HT. It leads to improved overall efficiency of 3.13 %, which was increased by 100 % and 50 % compared to that of spiro-OMeTAD with 75 nm and 23 nm TiO$_2$ particles, respectively (see Table 6.3). However, the V_{oc} of the P3HT cell was much lower in comparison to that of the spiro-OMeTAD based cell. It could be from high charge recombination due to short exciton diffusion length (3-10 nm) of P3HT. We did not use any additives to improve V_{oc}, but recently Grimes et al.[17] and Ramakrishna et al.[15] reported enhanced V_{oc} and F.F. by using tBP or Li salt in TiO$_2$/P3HT hybrid solar cells. Therefore, the P3HT based cell has a potential for increasing power conversion efficiency by using additives or heat treatment. From the IPCE and photovoltaic performance of the P3HT based cells, we can clearly see that P3HT has dual functions as a hole transporter and sensitizer. As a HTM, the P3HT regenerates the oxidized dye molecule and as a sensitizer, it can be excited by

the incident light and gives electrons to the TiO_2. As a sensitizer, dye molecules could function as an electronic mediator or interface modifier to improve the electron injection efficiency, resulting in increasing photocurrent[12, 15, 16].

HTM	J_{sc} (mA/cm^2)	V_{oc} (mV)	F.F.	η (%)
P3HT	12.1	510	0.50	3.13
Spiro-OMeTAD	1.03	635	0.51	0.34

Table 6.3. Photovoltaic parameters of the YD2 sensitized P3HT and spiro-OMeTAD cells with 75 nm TiO_2 particles measured under full sunlight (100 mW/cm^2).
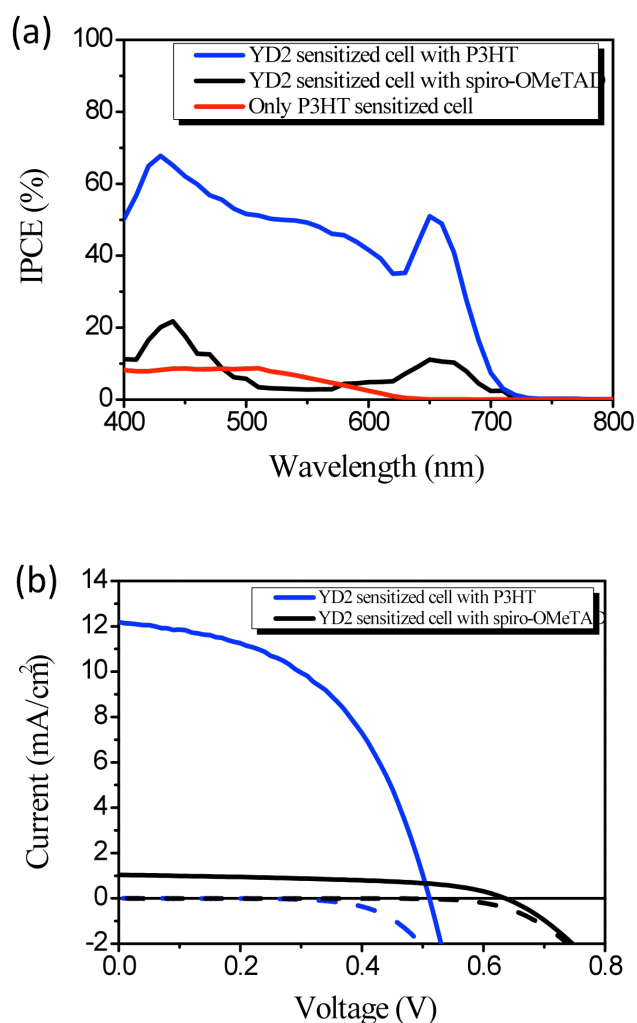

Figure 6.8. (a) Photocurrent action spectrum and (b) J-V characteristics of P3HT based cell (blue line) and spiro-OMeTAD based cell (black line) with 75 nm TiO_2 particles.

We also expect that Förster resonance energy transfer (FRET) from P3HT to YD2 could contribute to the high photocurrent of the cell. Because there is significant spectral overlap between the absorption of the YD2s Q band and the emission of the P3HT (see Figure 6.6)[28]. FRET occurs when the electronically excited state of a "donor" molecule transfers its energy to an "acceptor" molecule via a nonradiative long-range dipole-dipole coupling, resulting in the decrease of the PL emission of the donor. This energy transfer mostly depends on the spectral overlap, center-to-center distance and relative orientation of donor and acceptor. In this work, the donor is P3HT and the acceptor is YD2 dye.

The energy transfer rate depends on the Förster radius (R_0) between the donor and the acceptor. The Förster radius, or the distance at which Förster energy transfer is 50 %, can be calculated using Equation (1)[29]:

$$R_0^6 = \frac{9Q_D(\ln 10)\kappa^2 J}{128\pi^5 n^4 N_A} \tag{1}$$

where Q_D is the photoluminescence efficiency of the donor (1 % for the P3HT), κ^2 is the orientation factor (2/3 for random orientation), n is the refractive index of the medium (1.6 for P3HT-TiO$_2$ film)[17], N_A is Avogadro's number, and J is the spectral overlap integral calculated as

$$J = \int F_D(\lambda)\varepsilon_A(\lambda)\lambda^4 d\lambda$$

where F_D is the normalised donor (P3HT) emission spectrum, and ε_A is the acceptor (YD2) molar extinction coefficient. Using Eq (1), a value $R_0 = 2$ nm is obtained. Similar results have been reported for P3HT/TiO$_2$ hybrid solar cells with Ru dyes or organic dyes[16, 17].

To investigate energy transfer between the P3HT and the YD2, spectral photoluminescence (PL) measurements were carried out. The PL quenching is evidence of the nonradiative energy transfer from an excited donor (P3HT) to the nearby acceptor (YD2) in the ground state. Therefore, the origin of the PL quenching can be assigned to the FRET process[30, 31]. Figure 6.9 shows the PL spectrum of the pristine P3HT and the P3HT/YD2 mixture. The PL intensity of the P3HT/YD2 mixture decreased remarkably compared to that of the pristine P3HT. The P3HT/YD2 mixture leads to a PL quenching ratio of about 90 %. The PL quenching should be attributed to efficient nonradiative energy transfer from the P3HT to the YD2. The spectral overlap between P3HT emission and YD2 absorption and efficient PL quenching indicate that the energy could be transferred between two components by means of FRET.

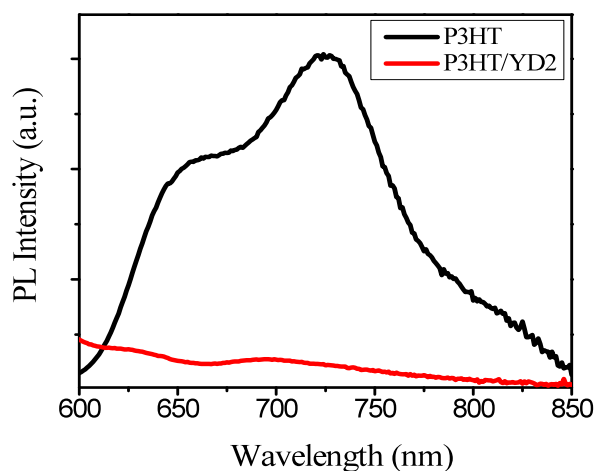Figure 6.9. PL spectrum of the pristine P3HT (black) and the P3HT/YD2 (red) mixture.

<u>Device fabrication of the SSDSCs sensitized with YD2 sensitizer</u>

<For devices with spiro-OMeTAD>

A mesoporous TiO_2 layer (~2 μm thick) was coated by the screen-printing technique with a Basic 23 nm paste. For sensitization, TiO_2 electrodes were immersed into a YD2 dye solution for 18 hours. The concentration of the dye solution was 0.2 mM in ethanol and 0.4 mM of CDCA as a co-adsorbent was added into the dye solution. For the YD2/C6 co-sensitization, TiO_2 electrodes were immersed into a YD2 solution for 18 hours and then rinsed electrodes with ethanol. Electrodes were immersed again into a C6 dye solution for 30 minutes. The concentration of the C6 dye solution was 0.1 mM in a mixture of acetonitril and *tert*-butyl alcohol solvents (volume ratio: 1/1). Standard spiro-OMeTAD solution was applied for a HTM layer. As a counter electrode, Au was evaporated on top of the HTM layer.

<For devices with P3HT>

A mesoporous TiO_2 layer (< 1 μm thick) was coated by a spin coater with a 75 nm size TiO_2 paste. For sensitization, TiO_2 electrodes were immersed into a YD2 dye solution for 18 hours. The concentration of the dye solution was 0.2 mM in ethanol and 0.4 mM of CDCA as a co-adsorbent was added into the dye solution. The dye coated TiO_2 electrodes were spun at 250 rpm for 500 sec with a P3HT (15 mg/ml in 1,2-dichlorobenzene) solution. A PEDOT:PSS solution (2.8 wt % dispersion in water) diluted with two volumes of MeOH was spin-coated onto $P3HT/YD2/TiO_2$ films at 2000 rpm for 30 sec. As a counter electrode, Au was evaporated on top of the samples.

6. 3 Conclusions

In this chapter, we employed a porphyrin sensitizer (coded as YD2) in different cell architectures. The YD2-only sensitized cell with spiro-OMeTAD yielded only 1.6 % power conversion efficiency due to low light harvesting capability even though it had very high extinction coefficients. However, the co-sensitization with a metal free sensitizer (coded as C6) improved the device IPCE remarkably by complementary spectral response, leading to an improvement of the photocurrent in the cell. Moreover, the co-sensitizer played a role as a co-adsorbent by enhancing the IPCEs of YD2 compared to YD2 alone by suppressing dye aggregation on the TiO_2 surface.

Also, we demonstrated TiO_2/P3HT hybrid solar cells with YD2. The YD2/P3HT cell generated very high photocurrent of 12 mA/cm^2 due to enhanced light harvesting by the contribution of two sensitizers (YD2 and P3HT) and efficient resonance energy transfer from P3HT to YD2 as well. The YD2/P3HT cell achieved 3.1 % overall efficiency. This result indicates that P3HT can successfully carry out dual functions as a HTM and a sensitizer in the cell.

Bibliography

1.   R. K. Lammi, R. W. Wagner, A. Ambroise, J. R. Diers, D. F. Bocian, D. Holten and J. S. Lindsey, The Journal of Physical Chemistry B **105** (22), 5341-5352 (2001).

2.   S.-L. Wu, H.-P. Lu, H.-T. Yu, S.-H. Chuang, C.-L. Chiu, C.-W. Lee, E. W.-G. Diau and C.-Y. Yeh, Energy & Environmental Science **3** (7), 949-955 (2010).

3.   A. Kay and M. Grätzel, The Journal of Physical Chemistry **97** (23), 6272-6277 (1993).

4.   A. Kay, R. Humphry-Baker and M. Grätzel, The Journal of Physical Chemistry **98** (3), 952-959 (1994).

5.   F. Odobel, E. Blart, M. Lagree, M. Villieras, H. Boujtita, N. El Murr, S. Caramori and C. Alberto Bignozzi, J Mater Chem **13** (3), 502-510 (2003).

6.   W. M. Campbell, K. W. Jolley, P. Wagner, K. Wagner, P. J. Walsh, K. C. Gordon, L. Schmidt-Mende, M. K. Nazeeruddin, Q. Wang, M. Grätzel and D. L. Officer, The Journal of Physical Chemistry C **111** (32), 11760-11762 (2007).

7.   S. Eu, S. Hayashi, T. Umeyama, A. Oguro, M. Kawasaki, N. Kadota, Y. Matano and H. Imahori, The Journal of Physical Chemistry C **111** (8), 3528-3537 (2007).

8.   M. Tanaka, S. Hayashi, S. Eu, T. Umeyama, Y. Matano and H. Imahori, Chemical Communications (20), 2069-2071 (2007).

9.   S. Hayashi, M. Tanaka, H. Hayashi, S. Eu, T. Umeyama, Y. Matano, Y. Araki and H. Imahori, The Journal of Physical Chemistry C **112** (39), 15576-15585 (2008).

10.   K. M. Coakley, Y. Liu, C. Goh and M. D. McGehee, MRS Bulletin **30** (1), 37-40 (2005).

11.   E. Lancelle-Beltran, P. Prené, C. Boscher, P. Belleville, P. Buvat and C. Sanchez, Adv Mater **18** (19), 2579-2582 (2006).

12.   C. Goh, S. R. Scully and M. D. McGehee, J Appl Phys **101** (11), 114503-114512 (2007).

13.   A. A. Voityuk, N. Rosch, M. Bixon and J. Jortner, The Journal of Physical Chemistry B **104** (41), 9740-9745 (2000).

14.   H. Imahori, H. Yamada, Y. Nishimura, I. Yamazaki and Y. Sakata, The Journal of Physical Chemistry B **104** (9), 2099-2108 (2000).

15.   R. Zhu, C. Y. Jiang, B. Liu and S. Ramakrishna, Adv Mater **21** (9), 994-1000 (2009).

16.   N. Kudo, S. Honda, Y. Shimazaki, H. Ohkita, S. Ito and H. Benten, Applied Physics Letters **90** (18), 183513-183513 (2007).

17.   G. K. Mor, S. Kim, M. Paulose, O. K. Varghese, K. Shankar, J. Basham and C. A. Grimes, Nano Lett **9** (12), 4250-4257 (2009).

18.   T. Bessho, S. M. Zakeeruddin, C.-Y. Yeh, E. W.-G. Diau and M. Grätzel, Angewandte Chemie International Edition **49** (37), 6646-6649 (2010).

19.   H.-P. Lu, C.-Y. Tsai, W.-N. Yen, C.-P. Hsieh, C.-W. Lee, C.-Y. Yeh and E. W.-G. Diau, The Journal of Physical Chemistry C **113** (49), 20990-20997 (2009).

20.   C.-P. Hsieh, H.-P. Lu, C.-L. Chiu, C.-W. Lee, S.-H. Chuang, C.-L. Mai, W.-N. Yen, S.-J. Hsu, E. W.-G. Diau and C.-Y. Yeh, J Mater Chem **20** (6), 1127-1134 (2010).

21.   Y. Tachibana, S. A. Haque, I. P. Mercer, J. R. Durrant and D. R. Klug, The Journal of Physical Chemistry B **104** (6), 1198-1205 (2000).

22.   J. Rochford, D. Chu, A. Hagfeldt and E. Galoppini, J Am Chem Soc **129** (15), 4655-4665 (2007).

23.   C. W. Lee, H. P. Lu, C. M. Lan, Y. L. Huang, Y. R. Liang, W. N. Yen, Y. C. Liu, Y. S. Lin, E. W. G. Diau and C. Y. Yeh, Chemistry – A European Journal **15** (6), 1403-1412 (2009).

24.   M. W. Lee, D. L. Lee, W. N. Yen and C. Y. Yeh, Journal of Macromolecular Science, Part A: Pure and Applied Chemistry **46** (7), 730-737 (2009).

25.   R. Y. Ogura, S. Nakane, M. Morooka, M. Orihashi, Y. Suzuki and K. Noda, Applied Physics Letters **94** (7), 073308-073303 (2009).

26.   K. M. Coakley and M. D. McGehee, Chemistry of Materials **16** (23), 4533-4542 (2004).

27.   K. M. Coakley and M. D. McGehee, Applied Physics Letters **83** (16), 3380-3382 (2003).

28.   B. E. Hardin, E. T. Hoke, P. B. Armstrong, J.-H. Yum, P. Comte, T. Torres, J. M. J. Fréchet, M. K. Nazeeruddin, M. Grätzel and M. D. McGehee, Nat Photon **3** (11), 667-667 (2009).

29.   T. Förster, Discussions of the Faraday Society **27**, 7-17 (1959).

30.   V. Biju, T. Itoh, Y. Baba and M. Ishikawa, The Journal of Physical Chemistry B **110** (51), 26068-26074 (2006).

31.   V. Biju, Y. Makita, A. Sonoda, H. Yokoyama, Y. Baba and M. Ishikawa, The Journal of Physical Chemistry B **109** (29), 13899-13905 (2005).

Chapter 7

General Conclusions and Outlook

The objective of this work was to improve the photovoltaic performance of solid state DSCs using spiro-OMeTAD as a hole transport material with different types of sensitizers. In SSDSCs we use thin TiO_2 films to avoid the pore-filling problem of HTM. Hence it is very important to use high molar extinction coefficient dyes with an efficient light harvesting capability for SSDSCs. Here we scanned a wide variety of different light harvesting systems like ruthenium sensitizers, organic dyes, semiconductor sensitizer, and porphyrin dye as a light absorber. In addition, we examined polymer hole conductor (polythiophene) instead of spiro-OMeTAD and TiO_2/polythiophene hybrid solar cells were successfully demonstrated as alternative solid-state devices.

Ruthenium sensitizers

We studied ruthenium sensitizers (coded as C101, C104, C106 and CYC-B1) having higher molar extinction coefficients compared to that of standard Z907 dye. These new sensitizers improved photocurrents and power conversion efficiencies of the cells resulting from enhanced light harvesting efficiencies. Moreover, we successfully exemplified a stable device performance for the first time with the C104 dye under full sunlight at 60 °C for 1000 h. A record power conversion efficiency of 5% was achieved with C106 sensitized device, to the best of my knowledge this is the highest efficiency reported with any ruthenium sensitizer.

Organic dyes

In order to increase the molar extinction coefficients and shift the spectral response to red region we tuned triarylamine donors by introducing alkoxy substituents (D5L6, D21L6 and D25L6) and extended π-conjugation bridges using dialkyl-cyclopentadithiophene units (C2, C6, C12) in D-π-A

organic dyes. This strategy leads to improve the power conversion efficiencies considerably compared to the cells sensitized with ruthenium sensitizers due to increase in the photocurrents. The C12 sensitized device yielded a NREL certified power conversion efficiency of 6 %, which was a new record efficiency for SSDSCs. Near infrared dyes (SQ1 and SQ2) were also evaluated and they showed possibilities for a panchromatic response using different device architectures such as tandem cells, FRET, or co-sensitization.

Semiconductor sensitizer - Sb_2S_3

Semiconductor sensitizers have gained attention owing to many attractive properties such as tunable band gap, high extinction coefficient and inexpensive process. In this work Sb_2S_3 was used as a light absorber instead of molecular sensitizers. The IPCE of Sb_2S_3 sensitized device reached almost 90 % and a power conversion efficiency of over 5 % measured under 0.1 sun. Under full sunlight, the efficiency was only 3 %, but an overall device performance could be enhanced through optimization of the interfacial properties of Sb_2S_3 coated TiO_2 and spiro-OMeTAD.

**Porphyrin sensitized solid-state solar cells**

A donor acceptor porphyrin (coded as YD2) sensitized solid-state cells with spiro-OMeTAD was demonstrated but the cell performance was low only 1.6 % power conversion efficiency due to an insufficient light harvesting and dye aggregations. We employed a new efficient system for the YD2 sensitizer by using polymer hole conductor, polythiophene. YD2 sensitized TiO_2/P3HT hybrid solar cells generated a very high photocurrent of 12 mA/cm^2 and yielded the power conversion efficiency of 3 %. The high current was ascribed to two reasons: i) filling a valley by P3HT where YD2 did not absorb light and ii) an extended IPCE to near infrared region by the combination of the YD2 and polythiophene. We could see that P3HT efficiently acted dual functions as a hole transporting material and light absorber in the cells. In addition, Förster resonance energy transfer between YD2 and P3HT was observed in photoluminescence measurements.

The performance of solid-state dye-sensitized solar cells has been made remarkable progress. But still several critical issues should be resolved in SSDSCs to replace liquid electrolyte-based DSCs: incomplete pore-filling of the spiro-OMeTAD, stability of the cell, and low light harvesting efficiency. The device performance can be improved by applying new light absorbing materials, modifications of the mesoporous TiO_2 layer, or systematic analysis to understand efficiency loss mechanism in the cells. As well as, new hole transporting materials should be developed in order to enhance a photovoltaic performance in solid-state DSCs.
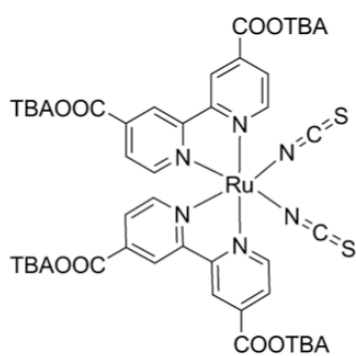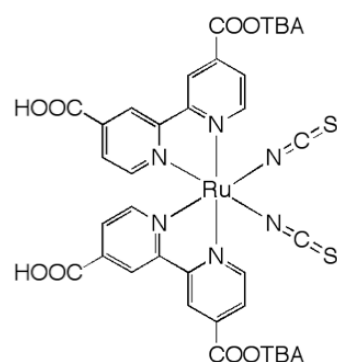
Appendix

A Molecular structures

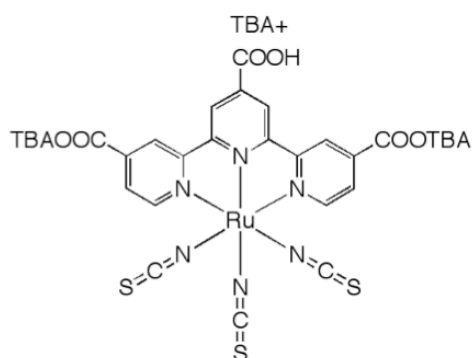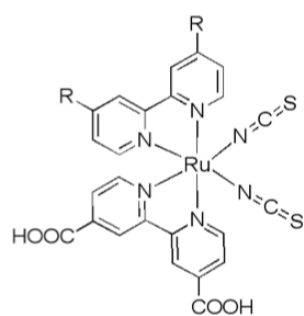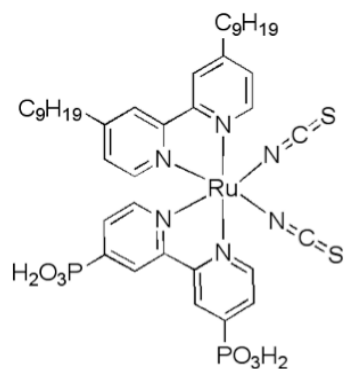### A. 1 Dyes
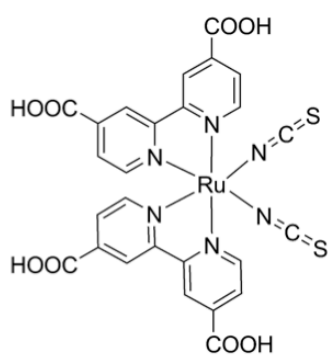
N3

N712

N719

N749

Z907: R = C_9H_{19}
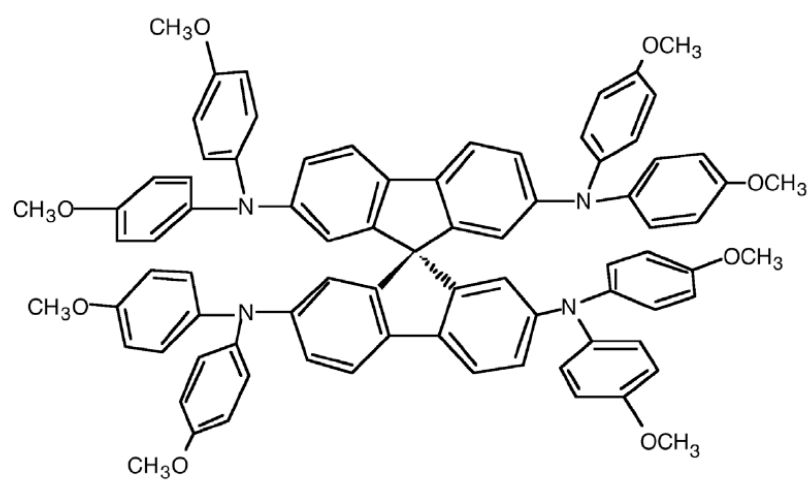N621: R = $C_{18}H_{37}$

Z955
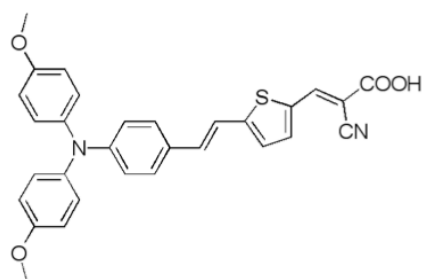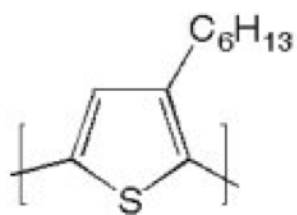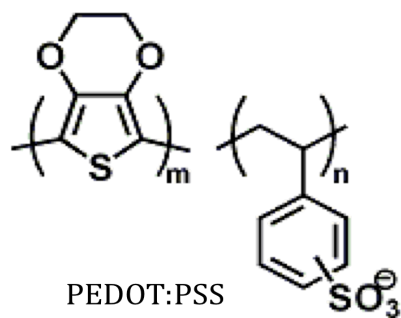

D9

A. 2 HTMs

2,2',7,7'-tetrakis(N,N-di-p-methoxyphenyl-amine)-9,9'-spirobifluorene
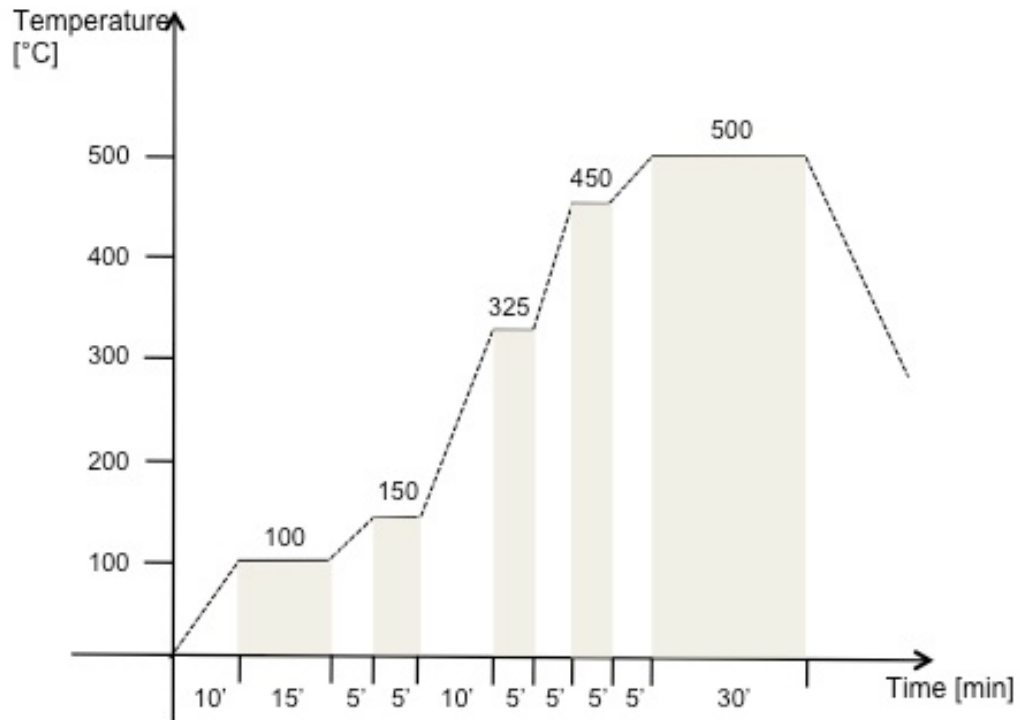

P3HT   PEDOT:PSS

B Temperature program for sintering of screen-printed TiO$_2$ films

Acknowledgement

First of all, I gratefully thank to Prof. Michael Grätzel for giving me the opportunity to do my Ph.D. thesis in his group and for his advice and guidance. This group is really good to work and study for dye-sensitized solar cells with various internal and external experts.

I am indebt to all LPI members and Prof. Jaques-E. Moser for a great help, in particular, I keenly appreciate Dr. Shaik Zakeeruddin helping and encouraging me all the time. Dr. Kevin Sivula, thank you so much for proof-reading a large portion of my manusript. I also appreciate Florian Le Formal and Dr. David Tilley for correcting my French and English.

A warm thank to Jun-Ho for sharing his knowledge with me, fruitful discussions and for screen-printing many TiO$_2$ films. I want to thank to Mme. Cevey, Dr. Peter Chen, Dr. Mingkui Wang and all member of the solid-tate group for wonderful collaborations and help, and Dr. Robin Humphry-Baker for helping PIA characterization and Pascal Comte for providing diverse TiO$_2$ pastes and important advice about TiO$_2$ films.

I would like to thank to Florian and Kevin for many hugs and warm envionment.

I am grateful to Takeru, Il, Jérémie, Francine, Thomas, Hyo-Joong, Sophie and Wieland for sharing joyful moments in Lausanne.

I would also express my gratitude to Ursula Gonthier, Nelly Gourdou and Anne-Lene Odegaard for all their administrative help.

Last but not least I wish to thank to my family for their endless love and support. Jun-Ho and Ji-Ah who make me happy-thank you so much and I love you.

Curriculum Vitae

Name: Soo-Jin MOON
Date of Birth: 11 July 1978
Nationality: S. Korea

Education

Feb. 2007 – 2011	Ph. D. Thesis: Solid-State Sensitized Heterojunction Solar Cells: Effect of Sensitizing System on Performance and Stability. Swiss Federal Institute of technology (EPFL), Switzerland Advisor: Prof. M. Grätzel
Mar. 2001 - Feb. 2003	M.S. in Material Science and Engineering, Gwangju Institute of Science and Technology (GIST), Gwangju, Korea
Mar. 1997 - Feb. 2001	B.S. in Chemical Engineering, Inha University, Incheon, Korea

Working experiences

Feb. 2005 – Jan. 2007	Researcher, Samsung SDI Central research center, Giheung, Korea
Mar. 2003 – Jan. 2005	Researcher, LG Chem. Research Park, Daejeon, Korea

Teaching experiences

Sep. 2007 – Sep. 2009	Teaching assistant, EPFL Physical chemistry lab, Experimental molecular sciences

List of Publications

[1]   "Enhanced-Light-Harvesting Amphiphilic Ruthenium Dye for Efficient Solid-State Dye-Sensitized Solar Cells", M. Wang, S.-J. Moon, D. Zhou, F. Le. Formal, N.-Le Cevey-Ha, R. Humphry-Baker, C. Grätzel, S. M. Zakeeruddin, M. Grätzel, *Advanced Functional materials*, 20, 1821, 2010.

[2]   "High Efficiency Solid-State Sensitized Heterojunction Photovoltaic device", M. Wang, Jingyuan Liu, Ngoc-Le Cevey-Ha, S.-J. Moon, P. Liska, R. Humphry-Baker, J.-E. Moser, C. Grätzel, P. Wang, S. M. Zakeeruddin, M. Grätzel, *Nano Today*, 5, 169, 2010.

[3]   "Sb_2S_3-Based Mesoscopic Solar Cell using an Organic Hole Conductor", S.-J. Moon, Y. Itzhaik, J.-H. Yum, S. M. Zakeeruddin, G. Hodes, and M. Grätzel, *Journal of Physical Chemistry Letters*, 1, 1524, 2010.

[4]   "Efficient and Stable Solid-State Dye-Sensitized Solar Cells Based on a High-Molar-Extinction-Coefficient Sensitizer", M. Wang, Soo-Jin Moon, M. Xu, K. Chittibabu, P. Wang, N.-Le Cevey-Ha, R. Humphry-Baker, S. M. Zakeeruddin, M. Grätzel, *Small*, 6, 319, 2010.

[5]   "Highly Efficient Organic Sensitizers for Solid-State Dye-Sensitized Solar Cells", S.-J. Moon, J.-H. Yum, R. Humphry-Baker, K. M. Karlsson, D. P. Hagberg, T. Marinado, A. Hagfeldt, L. Sun, M. Grätzel and M. K. Nazeeruddin, *Journal of Physical Chemistry C*, 113, 16816, 2009.

[6]   "Panchromatic Response in Solid-State Dye-Sensitized Solar Cells Containing Phosphorescent Energy Relay Dyes", J.-H. Yum, B. E. Hardin, S.-J. Moon, E. Baranoff, F. Nüesch, M.D. McGehee, M. Graetzel and M.K. Nazeeruddin *Angew. Chem. Int. Ed.*, 48, 9277, 2009.

[7]   "Molecular Design of Unsymmetrical Squaraine Dyes for High Efficiency Conversion of Low Energy Photons into Electrons using TiO_2 Nanocrystalline Films", T. Geiger, S. Kuster, J.-H. Yum, S.-J. Moon, M. K. Nazeeruddin, M. Grätzel, F. Nüesch, *Advanced Functional materials*, 19, 2720, 2009.

[8]   "PbS and CdS Quantum Dots-Sensitized Solid-State Solar Cells: ''Old Concepts, New Results'', H. Lee, H. C. Leventis, S.-J. Moon, P. Chen, S. Ito, S. A. Haque, T. Torres, F. Nüesch, T. Geiger, S. M. Zakeeruddin, M. Grätzel, and M. K. Nazeeruddin, *Advanced Functional materials*, 19, 2735, 2009.

[9]   "Regenerative PbS and CdS Quantum Dot Sensitized Solar Cells with a Cobalt Complex as Hole Mediato", H. Lee, P. Chen, S.-J. Moon, F. Sauvage, K. Sivula, T. Bessho, D. R. Gamelin, P. Comte, S. M. Zakeeruddin, S. I. Seok, M. Grätzel, and M. K. Nazeeruddin, *Langmuir*, 25, 7602, 2009.

[10]   "Surface Design in Solid-State Dye Sensitized Solar Cells: Effects of Zwitterionic Coadsorbents on Photovoltaic Performance", M. Wang, C. Grätzel, S.-J. Moon, R. Humphry-Baker, N. Rossier-Iten, S. M. Zakeeruddin, and M. Grätzel, *Advanced Functional materials*, 19, 1, 2009.

[11]   "A Light-Resistant Organic Sensitizer for Solar-Cell Applications", J.-H. Yum, D. P.

Hagberg, <u>S.-J. Moon</u>, K. M. Karlsson, T. Marinado, L. Sun, A. Hagfeldt, M. K. Nazeeruddin, M. Grätzel, *Angewandte Chemie*, 48, 1576–1580, 2009.

[12]   "High Open-circuit Voltage Solid-State Dye-Sensitized Solar Cells with Organic Dye", P. Chen, J.-H. Yum, F. De Angelis, E. Mosconi, S. Fantacci, <u>S.-J. Moon</u>, R. Humphry Baker, J. Ko, M. K. Nazeeruddin and M. Grätzel, *Nanoletter*, 9, 2487, 2009.

[13]   "An improved Perylene Sensitizer for Solar Cell Applications". C. Li, J.-H. Yum, <u>S.-J. Moon</u>, A. Herrmann, F. Eickemeyer, N. G. Pschirer, P. Erk, J. Schneboom, K. Mullen, M. Grätzel and M. K. Nazeeruddin, *ChemSusChem*, 1, 615, 2008.

[14]   "Effect of coadsorbent on the photovoltaic performance of squaraine sensitized nanocrystalline solar cells". J.-H. Yum, <u>S.-J. Moon</u>, R. Humphry-Baker, P. Walter, F. Nüesch, M. Grätzel and M. K. Nazeeruddin, *Nanotechnology*, 19, 424005, 2008.

Presentations

[1]   2008 ESF Research conférences, Obergurl (Austria), poster présentation, The influence of cografting molecules on the performance of solid-state dye-sensitized solar cells.

[2]   2009 PVSEC 19, Jeju (South Korea), poster presentation, Highly efficient organic sensitizers for solid-state dye-sensitized solar cells.

[3]   2010 Nanophotonics, Tsukuba (Japan), oral presentation, Highly efficient dye-sensitized solar cells based on high molar extinction coefficient metal free sensitizers.